UNIVERSITY OF CALIFORNIA

Los Angeles

# Chemical Reactions at the Earth's Core-Mantle Boundary

A dissertation submitted in partial satisfaction

of the requirements for the degree

Doctor of Philosophy in Geology

by

Leslie Insixiengmay

2024

ABSTRACT OF THE DISSERTATION

Chemical Reactions at the Earth's Core-Mantle Boundary

by

Leslie Insixiengmay
Doctor of Philosophy in Geology
University of California, Los Angeles, 2024
Professor Lars P. Stixrude, Chair

Earth's evolution and structure depends heavily on the composition of its interior and the processes occurring deep within. The main objective of this thesis is to better understand the nature of the core-mantle boundary, which not only provides insight for the Earth's interior, but can also be related to other planetary body interiors as well. At the core-mantle boundary, two major planet forming materials (rock and metal) are juxtaposed at high temperatures where the interaction of the materials may occur. Characterizing this interaction requires investigating any chemical reactions that may occur and the possible transport of heat and mass between these two regions. The behavior of this boundary layer can be directly related to understanding deep Earth dynamics, including the origin of the early dynamo, observed seismic structures in the deep mantle, and the redox chemistry of Earth. The work in this thesis outline the different aspects of my Ph.D. projects that work to investigate the nature of the core-mantle boundary. This not only includes the possible interaction of existing mantle and core, but also the behavior of materials introduced to this region by tectonic activity originating from the Earth's surface such as $H_2O$, and the interaction of this other important planetary component (ice) with rock and metal. I apply

first principles molecular dynamics to investigate the chemical reactions of rock and metal materials in the Earth's mantle. I also investigate the material properties of two FeOOH polymorphs, $\varepsilon$-FeOOH and pyrite-structured FeOOH, using first principles static simulations that perform ground state calculations to determine phase stability, elasticity, and phonon vibrational frequencies.

The dissertation of Leslie Insixiengmay is approved.

Abby Kavner

Edward Donald Young

Edwin Arthur Schauble

Lars P. Stixrude, Committee Chair

University of California, Los Angeles

2024

*To my parents, Ken, Rey, and Jensen*

TABLE OF CONTENTS

LIST OF FIGURES

LIST OF TABLES

# ACKNOWLEDGMENTS

I am profoundly grateful for all of those who have supported me throughout my doctoral journey, without whom this thesis would not have been possible.

First and foremost, I extended my deepest appreciation to my advisor Lars Stixrude, whose guidance, wisdom, and unconditional support have been invaluable. Your mentorship not only shaped this research, but also fostered my growth as a scholar. I will miss being able to stop by your office for advice, whether for science, career, or for life advice.

I would also like to thank the members of my doctoral committee Ed Young, Edwin Schauble, and Abby Kavner for their insightful feedback, constructive criticism, and encouragement at every stage of this endeavor.

I am grateful to my friends at UCLA, whose camaraderie and intellectual conversations greatly enriched my experience here. To my group mates: Fred Wilson, Francis Dragulet, Travis Gilmore, David James, Bing Chua Hong, and Junjie Dong. To Carolina's group and next door office mates: Antoniette Grima, Kiran Chotalia, Xiyuan Bao, Boontigan Kuhasubpasin, Matthew Bogumil, and Joseph Lewis-Merill. Thank you all so much for keeping me sane this whole time and for all of the fun office conversations. To my great department friends: Mark Hubbert, Will Misener, Francisco Spaulding-Astudillo, Taylor Dorn, Justin Higa, Akash Gupta, Han Bao, Kevin Shao, Abijah Simon, Dan Fineman, Valeria Jaramillo, Heather Kirkpatrick, Sebastian Krause, Sarah Marcum and Maxwell Parks. An honorable mention to my dear friend Matevz Frajnkovic for carrying me through statistical mechanics, twice, and supporting me both professionally and personally. A special thanks and shout out to Alex Cave and Rekha Cave for always looking out for me, being my outlet to the world outside of academia, and for being the best quarantine team during those strange times.

I am grateful for the staff in the EPSS department who have helped sort through all sorts of logistical hurdles: Lauri Holbrook, Tasha Taylor, Carlene Brown, Anthony Sansone, Rod

O'Connor, Nanette Capulong, Eric Wessenauer, Kelli Yang, and Rick Fort.

I would also like to thank the UCLA Judo club for making my last year at UCLA extremely fun and fulfilling. Thank you Sensei Kenji Osugi and Sensei Dave Guerrero for your wisdom, knowledge, and mentorship towards me becoming a better judoka and person. Thank you for showing by example your commitment to the judo community; I will always admire and strive to be leaders like you two.

To all of my teachers and mentors whose guidance paved the pathway to my academic journey and successes: Thomas Jordan, Scott Paterson, Aaron Celestian, Alyssa Bell, Stephanie Abramowicz, Jan Amend, John Platt, Doug Hammond, Babsi Ratschbacher, Xin Song, Katie Ardill, and Cindy Waite. Thank you to my high school teacher Mr. (James) Weide for inspiring me to pursue geological sciences as a career after taking his Earth and Space Science class.

To my lifelong USC friends: Patrick Cho, Peter Wynn, Resherle Verna, Abby Wesley, Yi Hou, and Geoffrey DeGrande whose support and encouragement all of these years have meant the world to me. I cannot fathom going through the PhD program without all of your love and support. Cheers to the next chapter of our lives!

To my childhood school friends who have always been there for me since the beginning: Emily Weyer, Farah Missaghi, and Sophia Missaghi. It's been so much fun seeing all of us grow through this life together and pursue our career goals that we set back in high school.

My deepest gratitude to my parents, who sacrificed everything to give me and my siblings a better life. Thank you to my siblings for always taking care of me: Eddie, Ailinh, Bobby, Vanna, and Amos, and of course Maria, Aaron, and Bao too. I will always be forever grateful for your selfless acts of kindness and love.

To Rey and Jensen, who have given me unconditional love, emotional and mental support, and for always keeping me grounded.

Lastly, thank you to Ken Mei. I'm so incredibly happy and lucky that I got to meet you

during my time at UCLA. Thank you for always being my rock throughout all of the highs and lows. Thank you for being the best cat dad. And, thank you for being the best partner that I could ask for in this life.

# VITA

2014 - 2016 B.S. Geological Sciences, University of Southern California.

2016 - 2018 M.S. Geology, University of California, Los Angeles.

# PUBLICATIONS

**L. Insixiengmay** and L. Stixrude, 2023, Hydrogen Bond Symmetrization and High-Spin to Low-Spin transition of $\varepsilon$-FeOOH at the Pressure of Earth's Lower Mantle, American Mineralogist. DOI: 10.2138/am-2022-8839

**L. Insixiengmay** and L. Stixrude, 2024, MgO Miscibility in Liquid Iron, Earth, Planetary, and Science Letters (In Review).

**L. Insixiengmay** and L. Stixrude, 2024, Complete Solubility of Rock and Iron at High Pressure and Temperature, (Manuscript in preparation).

**L. Insixiengmay** and L. Stixrude, 2024, High-Spin to Low-Spin Transition of Pyrite-FeOOH, (Manuscript in preparation).

**L. Insixiengmay** and L. Stixrude, 2024, Hydrogen Bond Dynamics of $\varepsilon$-FeOOH, (Manuscript in preparation).

# CHAPTER 1

# Introduction

## 1.1 The Earth's Core-Mantle Boundary

At a depth of 2891 km beneath the Earth's surface, the core-mantle boundary shows the largest contrast in physical properties of any boundary in Earth, exceeding even the air-rock interface in the contrast in density, seismic wave velocity, and electrical conductivity. The contrast in material properties profoundly influences the dynamics of the deep Earth, separating the rapidly convecting core, where the Earth's magnetic field is produced, from the much more viscous and more sluggishly convecting mantle.

The core-mantle boundary is seismically reflective and therefore sharp, a property originating in the immiscibility of the silicate and iron-rich material on either side of the boundary at the temperature conditions prevalent in Earth today. Immediately above the core-mantle boundary, seismology reveals rich structure in the lowermost 200 - 300 km of the mantle, a region known as the D″ layer. This layer exhibits radial and lateral seismic velocity heterogeneity, anomalous velocity gradients and shear wave discontinuities, and anisotropy (Garnero and McNamara, 2008). The origin of many of these structures are unknown, such as the large-low-shear-wave velocity provinces, of several hundred km vertical and several thousand km lateral length scales, and the ultra-low-velocity zones, only a few km thick and several hundred km across.

The core-mantle boundary region is likely to contain a thermal boundary layer, with a temperature contrast of perhaps 1000 K, across which heat must be transported by conduc-

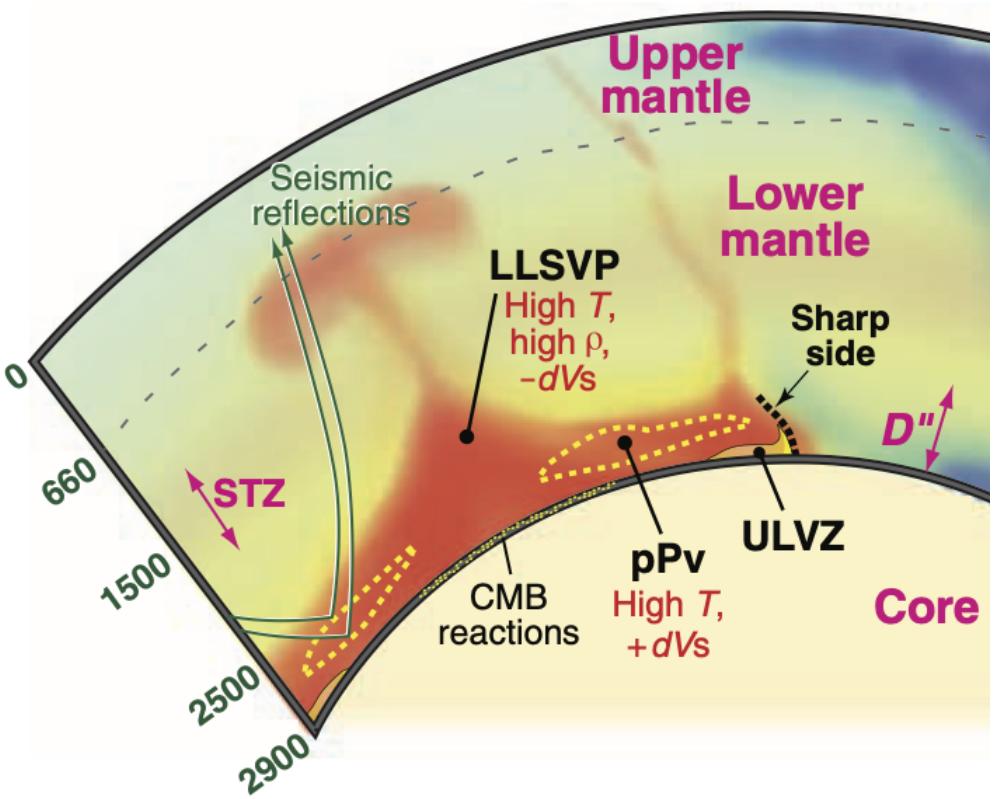


**Figure 1.1:** A schematic of the core-mantle boundary region from Garnero and McNamara (2008), showing the presence of large-low-shear-wave-velocity provinces (LLSVP) with vertical length scale of several 100 km, and distinguished from their surroundings by larger density ($\rho$), smaller shear wave velocity ($V_S$), and seismically sharp lateral boundaries indicating a distinct chemical composition from the rest of the mantle; ultra-low-velocity zones (ULVZ) with thickness of several km and extremely low shear wave velocity (40% lower than surrounding mantle); regions of stability of the post-perovskite phase (pPv), which reflect seismic energy, and therefore help us observationally to constrain the properties of the D$''$ region, consisting of the bottom-most few 100 km of the mantle. Iron in the mantle undergoes a high-spin to low-spin transition over the indicate range (spin transition zone: STZ). The background colors indicated inferred temperature, showing a schematic upwelling mantle plume and a subducting slab.

tion (Lay et al., 2008). This boundary layer controls heat flow from the core, and thus the strength of the magnetic field, and is the likely source of mantle plumes, such as the one responsible for Hawaiian volcanism. The thickness of the thermal boundary layer is thought to vary laterally: thicker in upwelling regions and thinner in regions of slab accumulation, modulating heat flow out of the core, and influencing the geometry of the magnetic field and its observable properties at the surface (Mound et al., 2019).

The D″ layer has often been interpreted as a thermal boundary layer, which would exist if there is a strong temperature contrast between the lower mantle and the outer core, leading to heat flux out of the core (Young and Lay, 1987). The existence of a thermal boundary layer has many implications such as providing an energy source for the general convection of the mantle by heating from below as opposed to internal heating only. Such systems with this type of heat transport may also have stronger upwelling plumes originating from the D″ region (Jones, 1977; Jeanloz and Richter, 1979; Yuen and Peltier, 1980; Stacey and Loper, 1983; Whaler, 1986; Olson et al., 1987). The power available to drive the geodynamo through convection in the core is controlled by the heat flow into the base of mantle; however, many uncertainties estimating the heat flux exists due to the dependence on properties of iron mixtures at high pressure and temperature conditions (Lay et al., 2008).

The core-mantle boundary and the D″ region raise fundamental questions regarding the nature of the deep Earth. Many of these could be encapsulated by the question: is the core-mantle boundary in chemical equilibrium? The answer is not clear, primarily due to a lack of knowledge of the relevant phase equilibria at the prevalent pressure, temperature conditions (136 GPa, 4000 K), which are challenging to replicate in the laboratory. If chemical disequilibrium prevails, which seems likely, at what rate and in which direction does mass transport proceed: ongoing dissolution of the mantle in the core, or exsolution of core components into the mantle? And what is the role of core-mantle chemical reaction at earlier stages in Earth's evolution when the temperature at the rock-iron interface was likely much higher and chemical reaction may have been much more extensive.

In this thesis, the main focus is to better understand the nature of chemical reactions between rock and iron at high pressure and temperature. The primary focus is on Earth, although as major planetary building blocks, my results may have important implications for understanding other rock-iron planets in the galaxy as well. In the remainder of this introductory chapter, I examine further our knowledge of the composition of core and mantle, what the role of the earliest stages of Earth's evolution may have been in setting their compositions, and some possible consequences of rock-iron reaction for our understanding of Earth's evolution.

## 1.2 Core Formation and Composition

The formation of the core is a fundamental process in Earth's history, shaping the internal structure, thermal and chemical state, and evolution. The segregation of dense, iron-rich material towards Earth's center releases gravitational energy in an amount sufficient to melt the entire Earth (Flasar and Birch, 1973; Solomon, 1979). Hf-W data suggests that core formation is complete by 30 Myr (Yin et al., 2002), occurring well before the Moon-forming impact at approximately 60 Myr (Touboul et al., 2007).

Element partitioning between metal and silicate at high pressure and temperature conditions set the compositions of core and mantle. The Earth's core is presumably made primarily of iron, but it is known that it cannot be pure iron because the seismically constrained density of the core is too low for this to be the case (Figure 1.2). Elements lighter than iron must therefore also be present, although their identity cannot be uniquely determined. Plausible candidate light elements in the core include S, Si, O, C, and H due to the abundance of these elements in the Solar System and our still limited knowledge of their partitioning between silicate and metal phases at extreme conditions.

Consideration of the extreme conditions of core-mantle equilibration force us to re-examine the conventional categorization of the elements as lithophile, siderophile, or at-

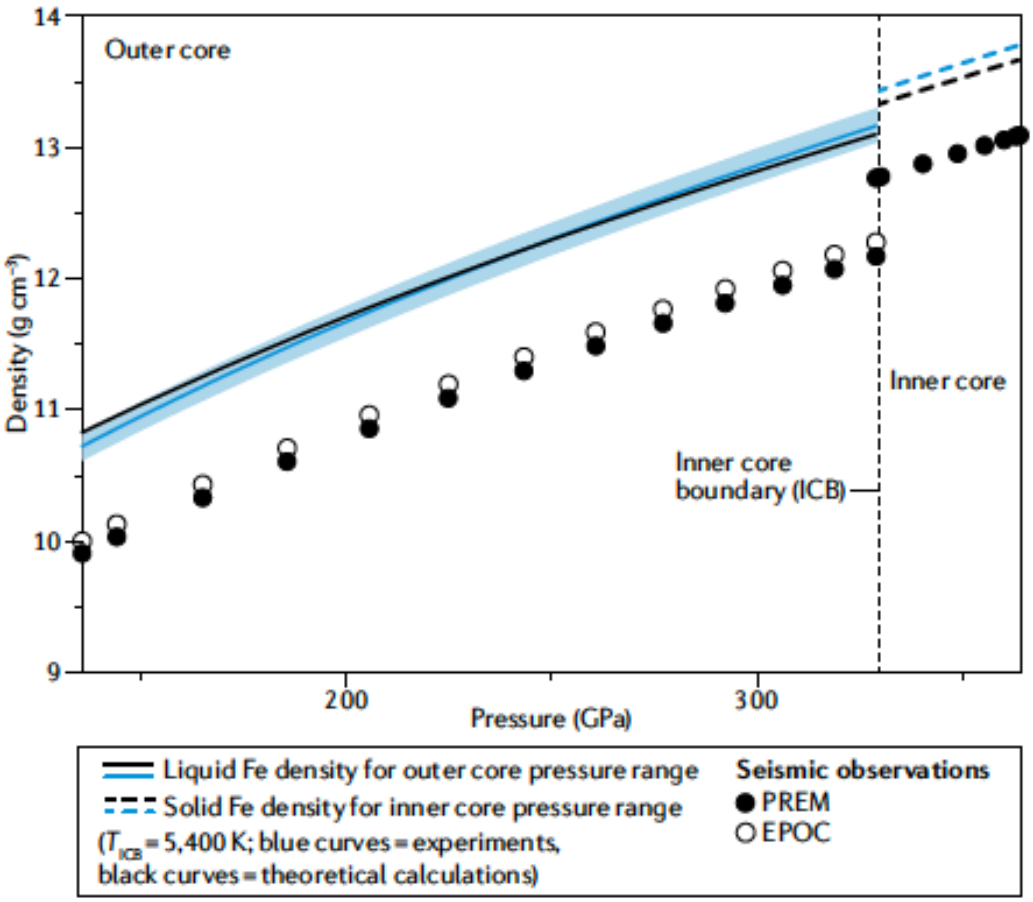


**Figure 1.2:** Core density mismatch between seismic observations and experimental/theoretical constraints on pure Fe density by Hirose et al. (2021).

mophile. Si and O are prototypical lithophile elements at low pressure, yet are plausible candidates for the light element in the core. H is the prototypical atmophile, but at high pressure becomes very soluble in iron. Higher temperatures in the early Earth, due to accretional energy and increased radioactive heat production, may have lead to much greater lithophile element solubility in the core. While lithophile elements have very limited solubility in the Earth's core today, the chemical interaction between core and mantle may have been more extensive in early Earth (Chidester et al., 2022a; Badro et al., 2016; Hirose et al., 2017). Other lithophile elements may also have been present in the early core, such as Mg, Ca, or Al. Lithophile elements may therefore serve as tracers of processes occurring during

the hottest portions of Earth's history.

The light element reduces the melting temperature of the core, thereby controlling the temperature at which the inner core crystallizes. Seismology shows that the density contrast between inner and outer core is too large to be explained by the solid-liquid density contrast alone: the inner core must exclude light elements. The process of inner core growth provides to important sources of energy for the generation of Earth's magnetic field: the latent heat of freezing, and release of gravitational energy as light elements are progressively excluded form the deepest parts of the Earth (Verhoogen, 1961; Gubbins et al., 1977; Braginsky, 1963; Loper, 1978). Thermal evolution models indicate the inner core nucleated at 0.7 to 1.5 Ga (Labrosse et al., 2001)

## 1.3 Magma Ocean

It is likely that the Earth began in a completely molten state with super liquidus core and mantle. This is because of the large sources of energy available to the early Earth, including the kinetic energy of accretion, and the gravitational energy released by core formation. The putative moon-forming giant impact is likely to have been sufficiently energetic by itself to melt the entire mantle (Nakajima and Stevenson, 2015), although it is likely the mantle was completely or mostly molten before the giant impact. The largely or completely molten state of the early Earth facilitates rapid core formation. At the same time, the low viscosity of a molten mantle points to very short, nearly free-fall times of iron blobs descending to the core, raising the question of the size of these blobs and the extent to which mantle and core could have been equilibrated during Earth's accretion (Maller et al., 2024).

Evidence that mantle and core reacted during the early molten stage comes from observed concentrations of moderately siderophile elements in the mantle today, and experiments that determine the partitioning of these elements between liquid silicate and iron phases (Li and Agee, 1996; Righter et al., 1997). Recent analyses indicate that paritioning must have

occurred at predominantly high pressure (70 GPa) and temperature (4000 K) (Badro et al., 2015).

Additional evidence of a magma ocean derives from Neodymium isotopes, which show that the ratio of $^{142}Nd/^{144}Nd$ in chondritic meteorites are 20 ppm lower than from samples derived from Earth (Boyet and Carlson, 2005) (Figure 1.3). In order to mass balance the Earth's Nd budget, a reservoir residing within the Earth's mantle has been proposed. Boyet and Carlson (2005) argue that because Nd is more incompatible than Sm, Nd selectively partition into melts, and this partitioning explains the high $^{143}Nd/^{144}Nd$ ($^{147}Sm$-$^{143}Nd$ decay) ratios measured from samples collected from erupted magmas where the enriched reservoir has never been sampled and is likely located at the base of the mantle.

The hypothesis of an enriched reservoir at great depths has been supported by some magma ocean evolution models (Labrosse et al., 2007; Ballmer et al., 2017) and via simulations (Deng and Stixrude, 2021), where crystallization of the magma ocean occurs from the mid-lower-mantle outwards and results in a basal magma ocean that may still be present today as a very thin layer at the core-mantle boundary that may explain ULVZ. Magma ocean crystallization from the center outwards arises from a steep adiabatic gradient (Stixrude et al., 2009) and shows that the mantle can crystallize from mid-mantle depths as opposed to the base of the mantle (Figure 1.4). The deep enriched reservoir may explain LLSVP structures as well.

Understanding the evolution of the magma ocean from a fully molten state to the almost completely crystalline state that we see today is important for recognizing possible geologic, geochemical, or seismological evidence of this early state of Earth's evolution. An important limitation of many previous studies of magma ocean evolution is that consideration of long-term reaction with the core is generally not considered, although such reaction may be important, largely due to a lack of knowledge of the relevant chemistry.

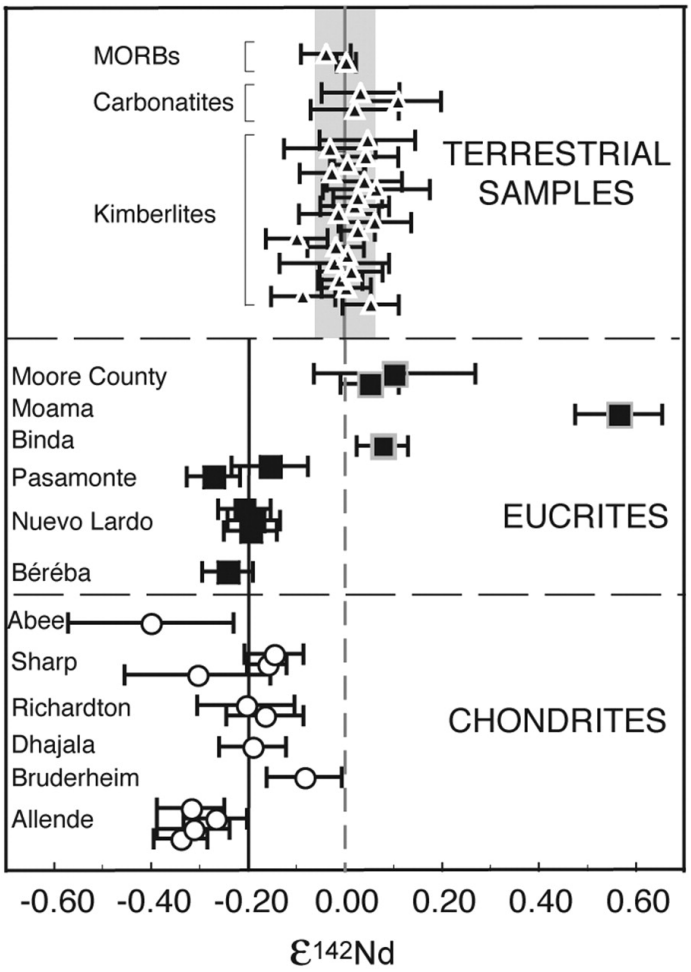


**Figure 1.3:** $^{142}$Nd/$^{144}$Nd ratios measured for chondrites and eucrites compared to the La Jolla Nd terrestrial standard ($\varepsilon^{142}$Nd) from Boyet and Carlson (2005). (Note: $\varepsilon^{142}\text{Nd} = [(^{142}\text{Nd}/^{144}Nd)_{\text{sample}}/(^{142}\text{Nd}/^{144}\text{Nd})_{\text{standard}} - 1] \times 10^4$). The chondritic and eucritic samples have negative $\varepsilon^{142}$Nd values relative to the terrestrial standard.

## 1.4 Early Earth Dynamo

Without the Earth's magnetic field, life on this planet may not exist. The presence of a magnetic field shields planetary bodies from solar wind, preventing atmospheric erosion and water loss (Tarduno et al., 2010). The Earth's magnetic field is generated by the geodynamo: the process in which the rotation and convection of an electrically-conductive liquid iron outer

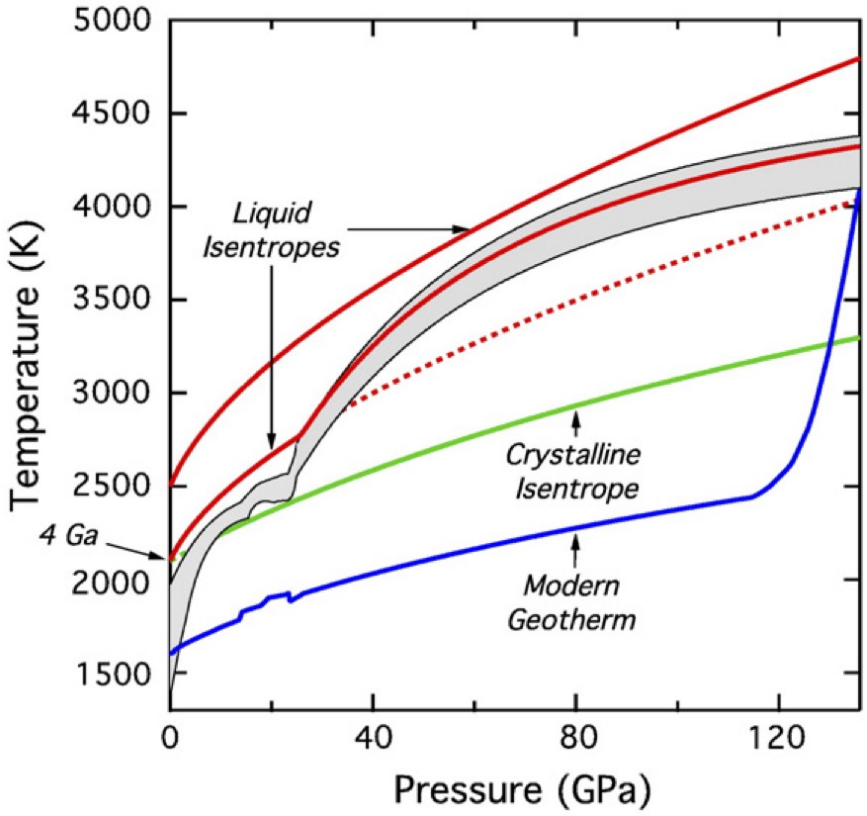


**Figure 1.4:** Figure from Stixrude et al. (2009) showing the gradient of isentropes in the ancient magma ocean. The magma ocean adiabat (uppermost red line) is steeper than the liquidus (grey envelope) requiring crystallization to begin in the mid-lower mantle upon cooling.

core generates a magnetic field. Crystallization of the inner core is thought to provide an essential source of energy to drive this process, via the release of latent heat and gravitational energy.

Paleomagnetic observations show that the Earth's magnetic field dates back at least 3.45 billion years (Bono et al., 2022) with some controversial measurements from inclusions in ancient zircons dating the field to 4.2 Ga (Tarduno et al., 2020). However, thermal evolution models suggest that the Earth's inner core began to crystallize only one billion years ago (Labrosse et al., 2001; Stevenson, 1981). Thus, while we have a convincing explanation for

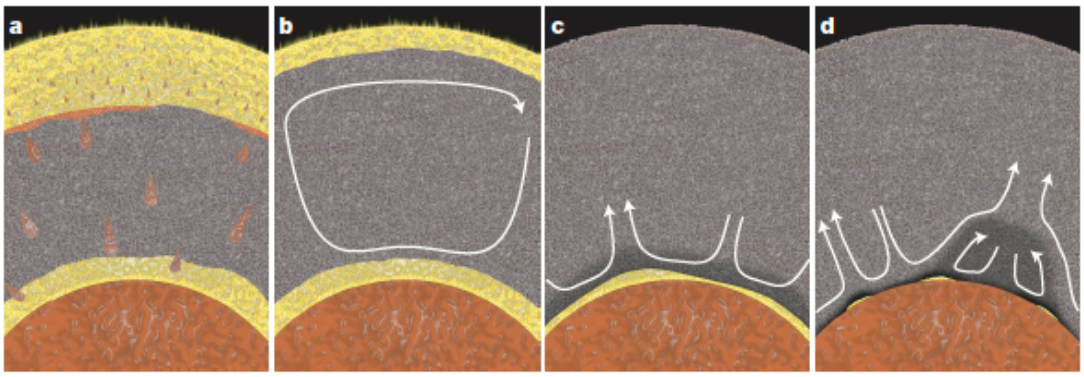


**Figure 1.5:** Schematic illustration from Labrosse et al. (2007) showing the formation and evolution of a dense basal magma ocean, including domains of silicate crystal (light grey), silicate liquid (yellow), enriched silicate crystal (dark grey), and metallic liquid (orange).

what has powered the magnetosphere for the last billion years, it is not clear what powered it prior to solidification of the inner core.

One explanation for the early dynamo envisions exsolution of light elements from the core, including lithophile elements such as Mg (O'Rourke and Stevenson, 2016). In this view, the lithophile elements are incorporated in the core during an early very high temperature stage of Earth's evolution, possibly following the giant moon-forming impact (Canup and Asphaug, 2001). As the initially homogeneous core cools, it becomes thermodynamically unstable to exsolution of separate phases of oxide-rich and metal-rich compositions. The compositional differences result in convection: the exsolved, buoyant oxide mantle material rises in the core, and the denser, liquid metal sinks. This movement drives convection that in this hypothesis is sufficient to create the magnetosphere.

An alternative hypothesis for early geodynamo generation is the existence of a silicate dynamo in the early Earth. The Earth's core was surrounded by a molten silicate basal magma ocean that may have survived for more than one billion years. In order to sustain a silicate dynamo, the electrical conductivity must exceed 10,000 S/m according to studies covering magnetohydrodynamic simulations, laboratory experiments, and planetary bodies

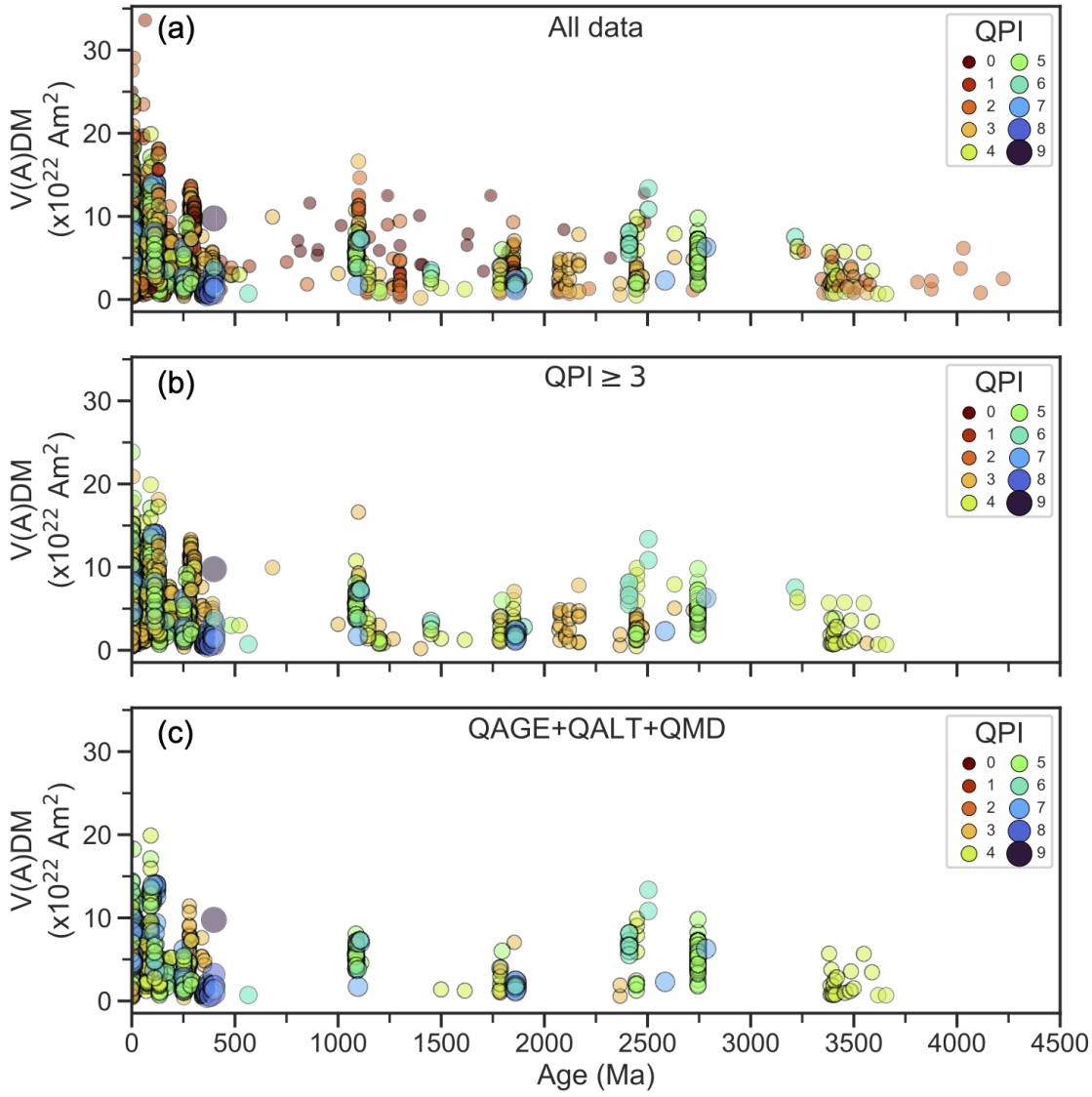


**Figure 1.6:** Compilation of paleomagnetic measurements of the virtual axial dipole moment (a measure of magnetic field strength) (Bono et al., 2022). The three panels sort the data according to quality criteria, with the lowermost panel showing only the highest quality data.

that host magnetic fields (Christensen and Aubert, 2006; Léorat and Nore, 2008). First principles simulations have shown that a silicate liquid, closely approximating the composition of the bulk silicate Earth, can produce electrical conductivity values exceeding 10,000 S/m at basal magma ocean conditions (Stixrude et al., 2020) (Figure 1.7).

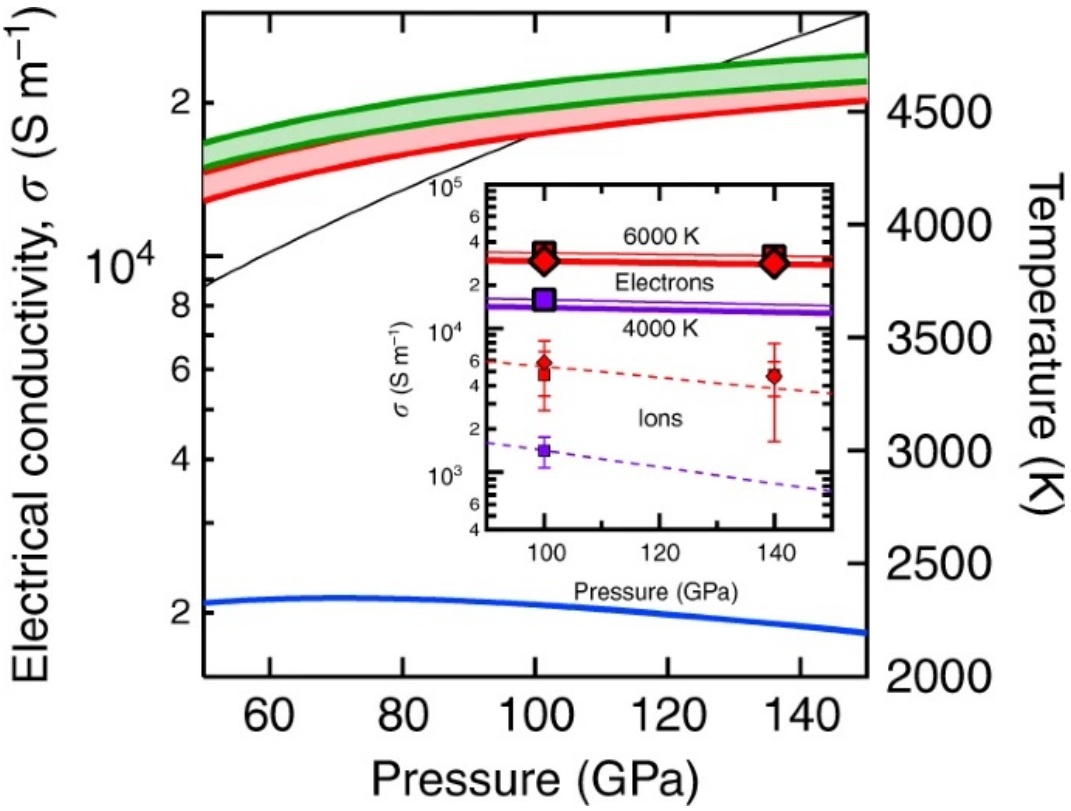


**Figure 1.7:** Electrical conductivity (red = electronic, blue = ionic, green = total) of a silicate dynamo from Stixrude et al. (2020).

## 1.5 Overview of Systems: Fe-MgO, Fe-$MgSiO_3$, and FeOOH

Because perovskite ($MgSiO_3$) and periclase (MgO) make up a large portion of the major constituent minerals in the Earth's mantle, investigating the interaction of the two with liquid Fe can provide insight on the interaction of the core-mantle boundary. The characterization of Fe-MgO and Fe-$MgSiO_3$ is poorly constrained due to the lack of a clear picture of the chemical reactions involved. It is not clear whether lithophile cations should be viewed as exchanging with Fe, a picture which is used to understand the partitioning of moderately siderophile elements (Wood, 2008), or dissolving as an oxide in the metal (Badro et al., 2018). These two pictures have contrasting implications for how we view the electronic structure and bonding of lithophile elements in the metal. My simulations of the Fe-MgO system turn

out to show unexpectedly simple symmetric regular solution behavior, and allows me to test the hypothesis that the early dynamo was driven by exsolution. The Fe-$MgSiO_3$ system is a first order model of chemical reaction between core and mantle and shows much richer behavior.

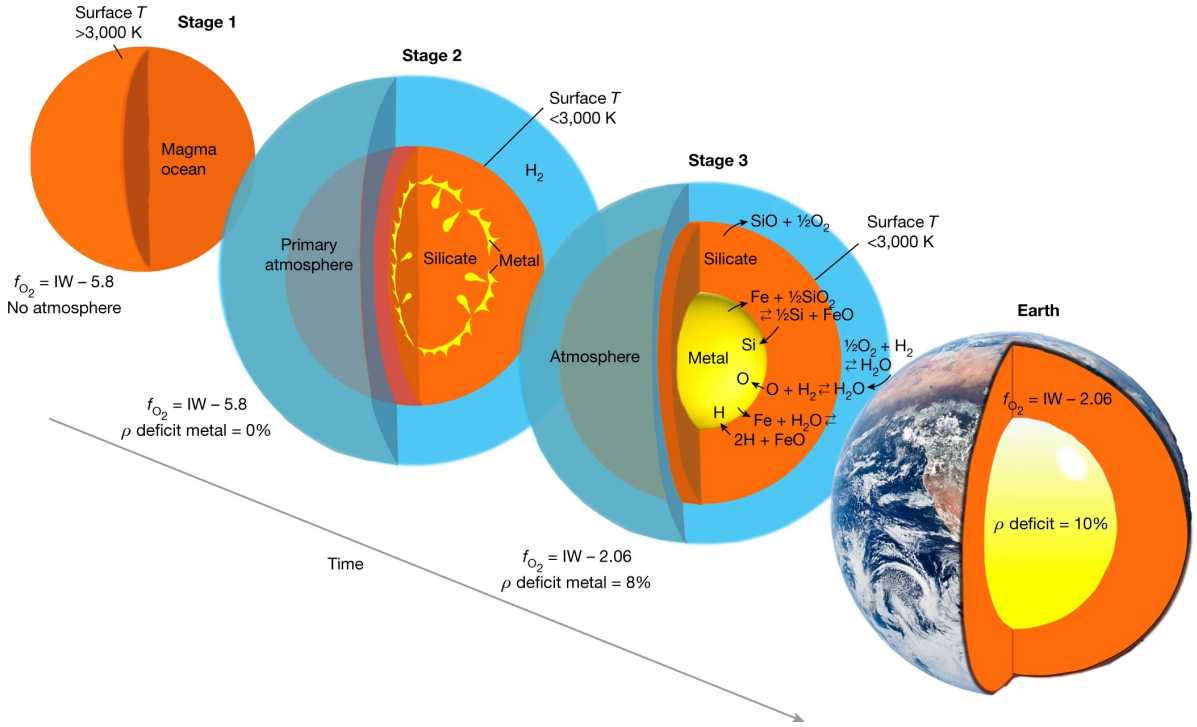


**Figure 1.8:** The proposed model for the evolution of Earth's progenitor embryos from Young et al. (2023). The figure illustrates the sequence of events leading to formation of $H_2O$ and light elements in metal.

The stability of $\varepsilon$-FeOOH and pyrite-structured FeOOH raises the possibility of chemical reactions between two major planetary forming components: metal and ice. But, very little is known still about the water content in the lower mantle. The oxy-hydroxides MOOH, including the FeOOH end-member have been proposed as important carriers of water in the lower mantle. Water may have been introduced to core-mantle boundary by tectonic activity originating from the Earth's surface, or primordial hydrogen in the Earth's mantle may have existed and derived from a hydrogen-rich primary atmosphere where interactions of oxygen,

iron, and hydrogen may have taken place early in Earth's history (Young et al., 2023). The physics of $\varepsilon$-FeOOH and pyrite-structured FeOOH show rich behavior, including high-spin to low-spin transitions, and pressure-induced changes in hydrogen bonding at high pressure.

# CHAPTER 2

# Density Functional Theory

In this chapter, I will cover a brief history of Density Functional Theory (DFT): the quantum mechanical theory used to describe the ground-state energies of a many-body system. Many Earth materials consists of elements containing multiple electrons, in addition to being solids with more than $10^{23}$ atoms, therefore making DFT an essential basis for all work done in this thesis. The history leading to the formation of DFT is rich and can be stemmed from the work of many leading scientists discovering quantum mechanics. We will begin the overview with Planck's constant, which is arguably the most important constant in the formation of quantum mechanics.

## 2.1 Planck's Constant

The German physicist Max Karl Ernst Ludwig Planck (April 23, 1858 - October 4, 1947) made many substantial contributions to theoretical physics and has been regarded as the father of quantum theory through his theoretical work on black body radiation. In the 19th century, numerous experiments were conducted to understand radiation given off by materials when heated. Observations showed that when a metal was heated, a shift in color occurred from red to yellow to blue as the metal was continuously heated. In other words, the radiation emitted from the metal showed transitions from a lower frequency to a higher frequency with respect to temperature. The frequency spectrum emitted is dependent on the material body itself, so one can consider an ideal body where all frequencies are emitted and absorbed - otherwise known as *black body radiation*.

The relationship observed experimentally between the intensity of black body radiation and frequency proved difficult for theoretical physicists to derive consistent expressions. The expression derived from 19$^{\text{th}}$ century physics is:

$$d\rho(\nu, T) = \rho_\nu(T)d\nu = \frac{8\pi k_B T}{c^3}\nu^2 d\nu \tag{2.1}$$

where $\rho_\nu(T)d\nu$ is the radiant energy density between frequencies $\nu$ and $\nu + d\nu$, $k_B$ is the Boltzmann constant, $T$ is the temperature, and $c$ is the speed of light. Equation 2.1 is known as the Rayleigh-Jeans Law and reproduces the experimental data at low frequencies, but predicts divergence of the radiant energy density at high frequencies - termed the ultraviolet catastrophe.

Like Rayleigh and Jeans, Planck assumed that the black body radiation was due to electron oscillations of the material body. However, Rayleigh and Jean assumed that the energies of electronic oscillations could have any value. Planck then made a revolutionary assumption that energies of oscillators were discrete and proportional to an integer multiple of the frequency (Planck, 1901), or quantized energy, winning him the 1918 Nobel Prize in physics and is now known as the Planck's postulate:

$$E = nh\nu \tag{2.2}$$

where $n$ is an integer ($n = 1, 2, 3, ...$), $h$ is a proportionality constant, and $\nu$ is the frequency of radiation. Using Planck's postulate and Ludwig Boltzmann's statistical interpretation of the second law of thermodynamics, Planck derived the equation

$$d\rho(\nu, T) = \rho_\nu(T)d\nu = \frac{8\pi h}{c^3}\frac{\nu^3 d\nu}{e^{h\nu/k_B T} - 1} \tag{2.3}$$

where the previously labeled proportionality constant $h$ in equation 2.2 has the value 6.626 x $10^{-34}$ Joule·seconds and is now a fundamental constant of physics: *Planck's constant*. The

value of Planck's constant yields excellent agreement with the experimental data for all frequencies and temperatures, and equation 2.3 is now known as the *Planck's distribution for black body radiation* (McQuarrie, 2008).

The Planck's constant is of fundamental importance, and its notion forms the cornerstone of quantum theory where quantized energy levels pin the stability and discrete nature of electronic states within atoms. In 1913, Niels Bohr introduced the third quantized model of the atom (Bohr, 1913) and solved the paradox where a classical electron orbiting a nucleus would lose its energy due to electromagnetic radiation and spiral down into the nucleus. Bohr solved this paradox with explicit reference to Planck's work where the atom could only have defined and discrete energies $E_n$:

$$E_n = -\frac{hcR_\infty}{n^2} \tag{2.4}$$

where $R_\infty$ is the Rydberg constant. The electron cannot get closer to the nucleus once the electron has reached the lowest energy ($n = 1$).

## 2.2 Wave-Particle Duality

The nature of light has always been difficult for scientists to describe because many experiments show light displaying wave-like behavior, and many other experiments show light behaving like discrete particles. This disparity of light is known as the wave-particle duality of light. In 1924, the French Physicist Louis de Broglie (August 15, 1892 - March 19, 1987) hypothesized that the reverse could be true for matter, which displays particle-like characteristics and may also display wave-like characteristics (De Broglie, 1923). Einstein proposed that light could be viewed in terms of photons with wavelength $\lambda$ and the momentum $p$ related by (Einstein, 1905):

$$\lambda = \frac{h}{p}. \tag{2.5}$$

De Broglie thought that if light obeyed this relationship, then it must also be true that matter obeys this relationship, leading to the *de Broglie wavelength*: $\lambda = h/mv$, where the momentum of the particle matter is $mv$. If one calculates the de Broglie wavelength of an electron traveling at 1.0% of the speed of light, the resultant de Broglie wavelength is 243 pm (where the mass of an electron is 9.109 x $10^{-31}$ kg), corresponding to the wavelength of X-rays and predicting that electrons can be observed to act like X-rays. The wave-like nature of matter was confirmed by the experiments of Davisson and Germer demonstrating diffraction of electrons by a crystal lattice, much like x-ray diffraction (Davisson and Germer, 1927).

Interestingly, J.J. Thompson showed experimentally in 1895 that the electron was a subatomic particle and his son, G.P. Thompson, showed in 1926 experimentally that the electron could act as a wave. The father won the Nobel Prize in 1906 for showing that the electron is a particle, and the son won a Nobel Prize in 1937 for showing that the electron is a wave (McQuarrie, 2008).

If we take the momentum of a particle of mass $m$ to be the mean value of an ideal gas of that particle at temperature $T$, then Eq. 2.5 yields the de Brogile thermal wavelength

$$\Lambda_{TH} = \frac{h}{2\pi m k_B T} = 43 \text{ Å} \left(\frac{m_e}{m}\right)^{1/2} \left(\frac{300 \text{ K}}{T}\right)^{1/2} \tag{2.6}$$

where $k_B$ is the Boltzmann constant and $m_e$ is the mass of the electron. $\Lambda_{TH}$ is much larger than the typical interparticle separation in planetary interiors ($\sim$1 Å), and we must treat the electron as a quantum object. For atomic nuclei, however, the de Brogile thermal wavelength is much smaller (0.25 Å for an oxygen nucleus) and these can be treated as classical objects for the temperatures of interest ($T >> 300$ K).

## 2.3 Schrödinger Equation

Erwin Schrödinger (August 12, 1887 - January 4, 1961) was an Austrian-Irish theoretical Physicist whose work with Paul Dirac won him the Nobel Prize in Physics in 1933 for the "discovery of new productive forms of atomic theory." The Schrödinger equation is the fundamental equation of quantum mechanics and is a linear partial differential equation for the wave function of a particle (Schrödinger, 1926). It is regarded to be a fundamental postulate of quantum mechanics, just as Newton's laws are fundamental postulates of classical mechanics.

The time-dependent Schrödinger equation describes a system evolving with time and takes the form:

$$i\hbar\frac{\partial}{\partial t}|\psi(t)\rangle = \hat{H}|\psi(t)\rangle \tag{2.7}$$

where $i$ is the imaginary unit, $\hbar$ is the reduced Planck's constant ($\hbar = h/2\pi$), $\psi(t)\rangle$ is the state vector of the quantum system: the wave function, $t$ is time, and $\hat{H}$ is the observable, or Hamiltonian operator. As an aside, the bracket notation used in equation 2.7 is the standard notation "Bra-ket" and is a standard notation for describing quantum states in quantum mechanics. Bra-ket notation is a notation for linear algebra and linear operators on complex vector spaces with their dual space. It is composed of angle brackets and vertical bars and represents the dot product of two states denoted by a bracket: $\langle\Phi|\Psi\rangle$.

More generally, the time-independent Schrödinger equation is used in this work. Going from the time-dependent to time-independent Schrödinger equation is a fundamental approximation that is justified from the Born-Oppenheimer approximation (section 2.10) due to the de-coupling of electronic and nuclear motions. The time-independent Schrödinter equation with stationary state wave functions is:

$$-\frac{\hbar^2}{2m}\nabla^2\psi + V(\mathbf{r})\psi(\mathbf{r}) = E\psi(\mathbf{r}) \tag{2.8}$$

whose solutions $\psi(\boldsymbol{r})$ describes a particle with mass $m$ with position $\mathbf{r}$ in a potential field $V(\boldsymbol{r})$. $\nabla^2$ is the Laplacian and $E$ is the total energy of a particle:

$$E = \frac{p^2}{2m} + V(\mathbf{r}) \tag{2.9}$$

It is important to note that classical mechanics deals with dynamics variables, such as position and momentum, and a measurable dynamical variable is called an observable.

A postulate of quantum mechanics states that a wave function $\psi(\boldsymbol{r})$ completely specifies the state of a quantum mechanical system. This is an incredibly powerful statement declaring that knowledge of the wave function provides total information about the system in question. However, in practice, the Schödinger equation becomes mathematically impossible to solve exactly for systems with more than one electron. Therefore, various approaches to approximating multi-electron systems have been formulated, seeking to find ways to solve the many-body Schrödinger equation.

## 2.4 Slater Determinant

The Slater determinant is named after John C. Slater, introduced in 1929, and ensures the anti-symmetry of a many-electron wave function (Slater, 1928, 1930). The anti-symmetric wave function arises from satisfying the Pauli exclusion principle (Pauli, 1925a, 1940), where two or more identical particles with half-integer spins (fermions) cannot occupy the same quantum state simultaneously. The Slater determinant consequently changes sign upon exchange of two electrons (recall that electrons are fermions).

We begin by approximating the wavefunction of a two particle system as the product of the wavefunctions of the individual particles, the so-called Hartree product:

$$\Psi(\mathbf{x}_1, \mathbf{x}_2) = \psi_1(\mathbf{x}_1)\psi_2(\mathbf{x}_2) \tag{2.10}$$

where $\psi_i(\mathbf{x}_j)$ is the wavefunction of particle $i$ at position $\mathbf{x}_j$. However, this wave function is not anti-symmetric under exchange of any two fermions, violating the Pauli exclusion principle, which requires anti-symmetry upon exchange

$$\Psi(\mathbf{x}_1, \mathbf{x}_2) = -\Psi(\mathbf{x}_2, \mathbf{x}_1). \tag{2.11}$$

A combination of the one-particle wavefunctions that does satisfy the anti-symmetry requirement is:

$$\Psi(\mathbf{x}_1, \mathbf{x}_2) = \frac{1}{\sqrt{2}} \{\psi_1(\mathbf{x}_1)\psi_2(\mathbf{x}_2) - \psi_1(\mathbf{x}_2)\psi_2(\mathbf{x}_1)\} \tag{2.12}$$

$$= \frac{1}{\sqrt{2}} \begin{vmatrix} \psi_1(\mathbf{x}_1) & \psi_2(\mathbf{x}_1) \\ \psi_1(\mathbf{x}_2) & \psi_2(\mathbf{x}_2) \end{vmatrix} \tag{2.13}$$

and becomes the determinant of the matrix, where the coefficient $1/\sqrt{2}$ assures that the wave function in equation 2.12 is normalized. The wave function in equation 2.12 is now anti-symmetric and makes fermions indistinguishable, such that the indices are now interchangeable. Furthermore, the wave function vanishes if the two particles occupy the same state at the same position, satisfying the Pauli exclusion principle.

The Slater determinant can be generalized to a system of $N$ fermions:

$$\Psi(\mathbf{x}_1, \mathbf{x}_2, ..., \mathbf{x}_N) = \frac{1}{\sqrt{N!}} \begin{vmatrix} \psi_1(\mathbf{x}_1) & \psi_2(\mathbf{x}_1) & \dots & \psi_N(\mathbf{x}_1) \\ \psi_1(\mathbf{x}_2) & \psi_2(\mathbf{x}_2) & \dots & \psi_N(\mathbf{x}_2) \\ \vdots & \vdots & \ddots & \vdots \\ \psi_1(\mathbf{x}_N) & \psi_2(\mathbf{x}_N) & \dots & \psi_N(\mathbf{x}_N) \end{vmatrix} \tag{2.14}$$

In this case, the Slater determinant vanishes if the set $\{\psi_i\}$ is linearly dependent, which is the case when two (or more) spin orbitals are the same thus violating the Pauli exclusion principle. In other words, the fact is expressed by stating that no two electrons with the same spin can occupy the same orbital.

## 2.5 Hartree-Fock

Soon after the discovery of the Schrödinger equation in 1926, Douglas Hartree introduced a procedure to calculate the approximate wave function and energies for atoms and ions from fundamental physical principles (ab initio), which he called the self-consistent field method (Hartree, 1928a,b,c). However, in his proposed method known as the Hartree product (mentioned in the Slater determinants section), the principle of anti-symmetry of the wave function was not obeyed, and thus not satisfying the Pauli exclusion principle. Vladimir Fock pointed this out and improved the algorithm by using Slater determinants (Fock, 1930), leading to what is now known as the Hartree-Fock method.

To derive the Hartree-Fock method, we begin with the Hartree approximation:

$$\Psi(r_1, r_2, ..., r_N) = \psi_1(r_1)\psi_2(r_2)...\psi_N(r_N) \tag{2.15}$$

making the initial assumption that the wave function of an N-body system can be written this way, and the electrons are independent and interact only through a Coulomb potential. This leads to the single-electron Schrödinger equation for state $i$:

$$\left[ -\frac{\hbar^2}{2m}\nabla^2 + V(r) \right] \psi_i(r) = \epsilon_i \psi_i(r) \tag{2.16}$$

and *V(r)* includes the contribution from nuclear-electron interaction:

$$V_{Ne}(r) = -Ze^2 \sum_R \frac{1}{r-R} \tag{2.17}$$

where $e$ is the electron charge, $R$ is the nucleus position, $r$ is the electron location, and $Z$ is the atomic number. The potential *V(r)* also includes the potential due to the other electrons: the Hartree potential

$$V_H(r) = -e \int \frac{n(r')}{|r-r'|} dr \tag{2.18}$$

with the electron charge density

$$n(r) = \sum_i |\psi_i(r)|^2 \tag{2.19}$$

However, as mentioned earlier, the Hartree approximation disobeys the principle of anti-symmetry, leading Fock to make modifications. The resulting Hartree-Fock theory assumes that the N-body wave function can be approximated using the Slater determinant, accounting for the anti-symmetry of electron wave functions:

$$\Psi^{HF} = \frac{1}{\sqrt{N!}} \det(\psi_1(r_1)\psi_2(r_2)...\psi_N(r_N)) \tag{2.20}$$

where $\psi^{HF}$ is the Hartree-Fock wave function. In deriving the Hartree-Fock theory, we carry out a variational calculation for which we must minimize:

$$\frac{\delta}{\delta\psi_i} E[\Psi^{HF}] = \delta\langle\Psi^{HF}|H^e|\Psi^{HF}\rangle = 0 \tag{2.21}$$

where $H^e$ is the Hamiltonian. A requirement of the derivation is that the change of energy with respect to the variation of orbitals vanishes as long as orbitals $\psi_i$ remain orthogonal, or

$$\langle\psi_i|\psi_j\rangle = \delta_{ij}. \tag{2.22}$$

as represented by Kronecker delta notation, $\delta_{ij}$. Once the variation is performed, the following equations are found:

$$\hat{F}(r_k)\psi_i(r_k) = \varepsilon_i\psi_i(r_k) \tag{2.23}$$

where the eigenvalue is called the Hartree-Fock orbital energy and introduce the Fock operator $\hat{F}(r_k)$ with the form:

$$\hat{F}(r_k) = \hat{h}(r_k) + \sum_j^N [2\hat{J}_j(r_k) - \hat{K}_j(r_k)] \tag{2.24}$$

$$\hat{h}(r_k) = -\frac{1}{2}\nabla^2 - \frac{Z}{r_k} \tag{2.25}$$

where the first term is the kinetic energy and the second term is the nuclear-electron interaction potential. The Coulomb operator $\hat{J}_j(r_k)$ is given by

$$\hat{J}_j(r_k)\psi_i(r_k) = \psi_i(r_k)\int dr_j \frac{\psi_j^*(r_j)\psi_j(r_j)}{|r_j - r_k|} \tag{2.26}$$

and the exchange operator $\hat{K}_j(r_k)$ is given by

$$\hat{K}_j(r_k)\psi_i(r_k) = \psi_j(r_k)\int dr_j \frac{\psi_j^*(r_j)\psi_k(r_j)}{|r_j - r_k|}. \tag{2.27}$$

To obtain the total energy E of a system using Hartree-Fock, we use the expectation value for a single determinant of spin orbitals

$$E = \langle \Psi^{HF}|\hat{H}|\Psi^{HF}\rangle = \sum_{j=1}^N I_j + \frac{1}{2}\sum_{i,j}(J_{ij} - K_{ij}) \tag{2.28}$$

with

$$I_j = \langle j|\hat{h}|j\rangle = \int dr\left(\psi_j^*\hat{h}_j(r)\psi_j\right) \tag{2.29}$$

$$J_{ij} = \int\int dr dr' \frac{\psi_i^*(r)\psi_j^*(r')\psi_i(r)\psi_j(r')}{|r' - r|} \tag{2.30}$$

$$K_{ij} = \int\int dr dr' \frac{\psi_i^*(r)\psi_j^*(r')\psi_i(r')\psi_j(r)}{|r' - r|} \tag{2.31}$$

where $J_{ij}$ and $K_{ij}$ are called the Coulomb integrals and exchange integrals, respectively if $i \neq j$. Note that $K_{ii} = J_{ii}$, however. The Hartree-Fock equations must be solved by a self-consistent procedure, where an initial guess of the $\psi_i(r)$ is made to calculate $\hat{F}(r)$ and then the result is used for $\hat{F}(r)$ to calculate a new set of $\psi_i(r)$. The iteration is continued until a self-consistent set of orbitals is obtained.

Because the exchange contribution is calculated exactly in Hartree-Fock theory, this method is very accurate when electron correlation contributions are minimal and is still widely used in quantum chemistry, and has been used to compute the high pressure properties of some Earth materials (Dovesi et al., 2017). However, the neglect of correlation contribution can result in large deviations from experimental results. Moreover, the single Slater determinant is inadequate in systems with un-paired electrons, as in metals or the iron cation. DFT takes a different approach, including both exchange and correlation, albeit approximately, which turns out to be a better choice for planetary materials.

## 2.6 Thomas-Fermi

The Thomas-Fermi model (Thomas, 1927; Fermi, 1927), developed independently and named after Llewellyn Thomas and Enrico Fermi, is seen as a precursor to DFT due to it being formulated in terms of the electronic density *n(r)* alone rather than from wave function theory. The model treats the many-body electronic structure system as semi-classical, where operations from classical mechanics is used, and its application of the uncertainty principle and Fermi statistics stem from quantum mechanics. The Thomas-Fermi theory makes three

assumptions for calculating the electric field of an atom: 1) All relativistic corrections are ignored, 2) the potential field about a nucleus depends only on the distance from the nucleus $r^n$ such that: $V \to 0$ as r $\to \infty$ and $V_r \to E$ (the nuclear charge) as $r \to 0$, and 3) the electrons are uniformly distributed spatially in phase space.

Variations in the de Broglie wavelength (eq. 2.5) must be small to satisfy the semi-classical regime, resulting in the treatment of the momentum operator $p$ as a spatial function rather than a quantum mechanical operator. Now, we can derive the Thomas-Fermi model starting with a small volume element $\Delta V$ and an atom in its ground state. We can fill up the spherical momentum space volume $V_F$ up to the Fermi momentum $p_F$

$$V_F = \frac{4}{3}\pi p_F^3(\mathbf{r}) \tag{2.32}$$

where $\mathbf{r}$ is the position vector of a point in $\Delta V$, the corresponding phase space volume is

$$\Delta V_{ph} = V_F \Delta V = \frac{4}{3}\pi p_F^3(\mathbf{r})\Delta V \tag{2.33}$$

and the electrons in $\Delta V_{ph}$ are uniformly distributed with two electrons per $h^3$. The number of electrons within this small volume phase space element is $\Delta N = n(\mathbf{r})\Delta V$, or

$$n(r) = \frac{8\pi}{3h^3} p_F^3(\mathbf{r}) \tag{2.34}$$

where $n(\mathbf{r})$ is the electron density. Both the momentum and electron density are solely functions of position $\mathbf{r}$, still asserting the assumption that the potential field is dependent only on distance from the nuclei. We now use the classical expression for the kinetic energy per unit vollume of an electron with mass $m_e$

$$t(\mathbf{r}) = n(\mathbf{r}) \int_0^{p_F(\mathbf{r})} \frac{p^2}{2m_e} \frac{4\pi p^2}{\frac{4}{3}\pi p_F^3(\mathbf{r})} dp \tag{2.35}$$

$$= C_{kin}[n(\mathbf{r})]^{5/3} \tag{2.36}$$

where the relationship between $n(\mathbf{r})$ and $p_F(\mathbf{r})$ from equation 2.34 has been utilized, and

$$C_{kin} = \frac{3h^2}{40m_e}\left(\frac{3}{\pi}\right)^{\frac{2}{3}}. \tag{2.37}$$

The total kinetic energy of the electrons can be obtained by integrating the kinetic energy per unit volume, resulting in

$$T = C_{kin}\int [n(\mathbf{r})]^{5/3} d^3r. \tag{2.38}$$

Now we can consider the potential energy sources in the Thomas-Fermi model. We begin with the potential energy due to the attraction between the negatively charged electrons and positively charged nucleus

$$V_{Ne} = \int n(\mathbf{r})V_N(\mathbf{r})d^3r \tag{2.39}$$

where $V_N$ is the potential energy of an electron at $\mathbf{r}$ due to the electric field of nucleus, and is expressed by

$$V_N(\mathbf{r}) = -\frac{Ze^2}{r} \tag{2.40}$$

where the nucleus is centered at $\mathbf{r} = 0$ with charge $Ze$. $Z$ is a positive integer (number of protons within the nucleus) and $e$ is the elementary charge, and $r$ is the distance of the electron from the nucleus.

We now consider the potential energy of the electrons due to their mutual repulsion

$$V_{ee} = \frac{1}{2}e^2 \int \frac{n(\mathbf{r})n(\mathbf{r}')}{|\mathbf{r}-\mathbf{r}'|} d^3r d^3r' \tag{2.41}$$

where $n(\mathbf{r})$ and $n(\mathbf{r}')$ are the electron densities at positions $\mathbf{r}$ and $\mathbf{r}'$, respectively.

The total energy of the electrons from the Thomas-Fermi model can be obtained through the sum of their kinetic and potential energies $E = T + V_{Ne} + V_{ee}$, resulting in

$$E = C_{kin} \int [n(\mathbf{r})]^{5/3} d^3r + \int n(\mathbf{r}) V_N(\mathbf{r}) d^3r + \frac{1}{2} e^2 \int \frac{n(\mathbf{r}) n(\mathbf{r}')}{|\mathbf{r} - \mathbf{r}'|} d^3r d^3r' \tag{2.42}$$

The Thomas-Fermi model was an important step towards DFT through the use of the electron density to calculate the total energy. However, the kinetic energy term is only an approximation, the exchange energy is not representative of an atom obeying the Pauli exclusion principle (anti-symmetry of electrons is neglected), and the electron correlation is also neglected. The Thomas-Fermi model is still used to approximate material properties in the stellar interior in the limit of infinite density, where it can be shown to become accurate.

## 2.7 Hohenberg-Kohn

The theoretical framework of DFT was first realized by Walter Kohn and Pierre Hohenberg in the two Hohenberg-Kohn theorems (Hohenberg and Kohn, 1964). The first theorem states that the total energy is a unique functional of the charge density: a scalar function of three spatial coordinates. In other words, the electron density uniquely determines the Hamiltonian operator and thus all system properties. The second theorem states that the ground-state electron density minimizes the total energy.

Here, we will begin with the first Hohenberg-Kohn theory, which states (directly quoted): *"The external potential $V_{ext}(r)$ is (to within a constant) a unique functional of $\rho(r)$; since, in turn $V_{ext}(r)$ fixes $\hat{H}$ we see that the full many particle ground state is a unique function of $\rho(r)$"*. The proof requires a system with two different external potentials $V_{ext}$ that differ by more than a constant, but give rise to the same electron density. The two external potentials give rise to two Hamiltonians, $\hat{H}$ and $\hat{H}'$, that differ by the external potential and hence

belong to two different ground state wave functions, $\psi$ and $\psi'$, but have the same electron density in the ground state $n_0(r)$. The two Hamiltonians take the form

$$\hat{H} = \hat{T} + \hat{V}_{ee} + \hat{V}_{ext} \tag{2.43}$$

$$\hat{H}' = \hat{T} + \hat{V}_{ee} + \hat{V}'_{ext} \tag{2.44}$$

Because $\psi'$ is the wave function not associated with $\hat{H}$, we can show

$$E = \langle\psi|\hat{H}|\psi\rangle < \langle\psi'|\hat{H}|\psi'\rangle \tag{2.45}$$

With $\psi$ and $\psi'$ being different, we can use $\psi'$ as a trial function for $\hat{H}$, and by the variational principle

$$E_0 < \langle\psi'|\hat{H}|\psi'\rangle = \langle\psi'|\hat{H}'|\psi'\rangle + \langle\psi'|\hat{H} - \hat{H}'|\psi'\rangle \tag{2.46}$$

Because the two Hamiltonian operators only differ in the external potential, we can expand and rewrite equation (2.46) as

$$E_0 < E'_0 + \langle\psi'|\hat{T} + \hat{V}_{ee} + \hat{V}_{ext} - \hat{T} - \hat{V}_{ee} - \hat{V}'_{ext}|\psi'\rangle \tag{2.47}$$

$$E_0 < E'_0 + \int n_0(\mathbf{r})\{V_{ext} - V'_{ext}\}d\mathbf{r} \tag{2.48}$$

By repeating the steps above and interchanging the un-primed and primed quantities, we obtain

$$E'_0 < E_0 - \int n_0(\mathbf{r})\{V_{ext} - V'_{ext}\}d\mathbf{r} \tag{2.49}$$

and sum of the two inequalities leads us to the contradiction

$$E_0 + E_0' < E_0' + E_0 \tag{2.50}$$

or that $0 < 0$. This proof shows that there cannot be two different external potentials that yield the same ground state electron density, or in other words $V_{ext}$ within some constant value is a unique functional of $n(r)$.

Next, we will discuss the second Hohenberg-Kohn theorem which states that the functional of the ground-state energy gives the lowest energy only if the input density is the true ground-state density. To prove this, we take a trial density $\tilde{n}(\mathbf{r})$ that defines its own Hamiltonian $\tilde{\hat{H}}$ and its own wave function $\tilde{\psi}$. This wave function can be taken to be the trial wave function for the Hamiltonian generated from the true external potential $V_{ext}$, leading to

$$\langle\tilde{\psi}|\hat{H}|\tilde{\psi}\rangle = T[\tilde{n}(r)] + V_{ee}[\tilde{n}(r)] + \int \tilde{n}(r)V_{ext}dr = E[\tilde{n}(r)] \geq E_0[\tilde{n}_0(r)] = \langle\psi_0|\hat{H}|\psi_0\rangle \tag{2.51}$$

and achieving our desired result, again, from the variational principle. We define the Hohenberg-Kohn functional as

$$F_{HK}[n(r)] \equiv \langle\psi|\hat{T} + \hat{V_{ee}}|\psi\rangle \tag{2.52}$$

which is valid for any number of particles and any external potential. Recall that all properties of a system are determined by the ground state density and is defined by an external potential $V_{ext}$. The ground state energy associated with $n(r)$ is given through the functional

$$E[n(r)] = \int n(r)V_{ext}dr + F_{HK}[n(r)] \tag{2.53}$$

and is minimized if the correct input density is the true ground state density.

## 2.8 Kohn-Sham Equations

Walter Kohn and Lu Jeu Sham continued to develop the Hohenberg-Kohn and ultimately produced the Kohn-Sham equations, or what is now known as the Kohn-Sham equations of DFT (Kohn and Sham, 1965). This work, and previous development in DFT, won Kohn and John Pople the 1998 Nobel Prize in Chemistry for the development of understanding the electronic properties of materials.

The Kohn-Sham equations allowed a system to be treated as non-interacting particles that yields the same electron density as an interacting system. This treatment assumes that the ground-state of the non-interacting system is equal to the ground-state of the interacting system. In practice, this involves solving the Schrödinger equation for each electron in the system as opposed to solving the mathematically impossible differential equation that is a function of all electrons. The derivation begins by consideration of the total energy of the system:

$$E = \int n(r)v_{ext}(r) + T_S[n(r)] + E_H[n(r)] + E_{XC}[n(r)]dr \tag{2.54}$$

where $T_S[n(r)]$ is the Kohn-Sham kinetic energy, $v_{ext}(r)$ is the external potential, $E_H[n(r)]$ is the Hartree or Coulomb energy, and $E_{XC}[n(r)]$ is the exchange and correlation energy effects (repulsive and attractive interactions). The terms are defined individually as:

$$T_S[n(r)] = \sum_{i=1}^{N} \int dr\varphi_i^*(r)\bigg( -\frac{\hbar^2}{2m}\nabla^2\bigg)\varphi_i(r), \tag{2.55}$$

where the Kohn-Sham kinetic energy is expressed in terms of the Kohn-Sham orbitals. The Hartree energy is expressed as:

$$E_H[n(r)] = \frac{e^2}{2}\int dr \int dr' \frac{n(r)n(r')}{|r-r'|} \tag{2.56}$$

and the exchange-correlation energy contribution is expressed within the Kohn-Sham potential, or effective potential,

$$v_{eff}(r) = v_{ext}(r) + e^2 \int \frac{n(r')}{|r - r'|} dr' + \frac{\delta E_{XC}[n(r)]}{\delta n(r)} \tag{2.57}$$

where the last term is the exchange-correlation potential and is expressed by the functional derivative:

$$v_{XC}(r) \equiv \frac{\delta E_{XC}[n(r)]}{\delta n(r)}. \tag{2.58}$$

As a result, we're left with the Schrödinger equation for a one-electron system:

$$\varepsilon_i \psi_i(r) = \left[ -\frac{\hbar^2}{2m} \nabla^2 + v_{eff}(r) \right] \psi_i(r) \tag{2.59}$$

where $\varepsilon_i$ is the orbital energy, or eigenvalue, of the $i^{th}$ electron of the corresponding Kohn-Sham orbital $\varphi_i$, and the electron density for an N-particle system is

$$n(r) = \sum_{i}^{N} |\varphi_i(r)|^2. \tag{2.60}$$

The exchange-correlation potential and energy are the only unknown terms in the Kohn-Sham equations, and thus the only unknowns of DFT. An exact form of the exchange-correlation potential that includes the contributions from exchange and correlation could be produced if the exchange-correlation energy were known exactly. As a result, the Kohn-Sham equations must be solved self-consistently such that the electron density produces the electronic potential used to construct the equations.

## 2.9 Exchange-Correlation Approximations

The exact form of the exchange-correlation (XC) potential is not known and must be approximated. Approximations are guided by limits and sum rules (Perdew et al., 1996) that the exchange-correlation potential must satisfy. In this section, I will discuss various XC approximations used in DFT and begin with discussing exchange and correlation itself.

### 2.9.1 Exchange

Distinguishing electrons from their physical properties is difficult as they are all identical. In order to distinguish electrons, their position and momentum must be defined. As discussed previously, the position and momentum of an electron is described by their wavefunction - probability of finding an electron at a particular position and time. In a system with two electrons, the probability of locating one electron depends on the probability of locating the second electron, in which the wavefunctions of the two electrons will intersect at some point. Exchange is possible because each electron is indistinguishable at this point. In the case of bosons, or integer spin particles, more than one boson may occupy the same quantum state, allowing symmetric wavefunctions to exchange while remaining the same. However, in the case of fermions, the wavefunction changes sign due to anti-symmetry because of the Pauli exclusion principle (Pauli, 1925b).

In practice, the exchange interaction is approximated in most DFT functionals such as the Local Density Approximation (LDA) (Kohn and Sham, 1965) and Generalized Gradient Approximation (GGA) (Perdew et al., 1992). However, a hybrid functional exists where DFT is combined with Hartree-Fock theory - incorporating a portion of exact exchange.

### 2.9.2 Correlation

The negative charge on electrons impart a repulsion on one another. Correlation is a measure of how the position of one electron is affected by the presence of other electrons. In a

system with thousands of atoms, calculating the dependence and influence of every other electron becomes an expensive computational feat. Therefore, approximating the correlation of electrons is necessary, as the full computation is not possible.

### 2.9.3 Local Density Approximation

The local density approximation (LDA) is the simplest method of describing the XC energy. This method assumes that the XC potential at every position in space is the same as that of a uniform electron gas (UEG, also known as 'Jellium') having the same density as found at that position. For a spin-unpolarized system, the LDA for the exchange-correlation energy is written as

$$E_{xc}^{LDA}[n(r)] = \int n(r)\varepsilon_{xc}[n(r)]dr \tag{2.61}$$

where $\varepsilon_{xc}$ is the XC energy per particle of the uniform electron gas of the electron density $n[(r)]$. The exchange-correlation is simply a linear combination and can be decomposed into

$$\varepsilon_{xc} = E_x + E_c \tag{2.62}$$

such that there are separate expressions for the exchange and correlation energy.

The XC potential is known analytically for the UEG and is defined by the Dirac Exchange (Dirac, 1930) yielding

$$E_x^{LDA}[n(r)] = -\frac{3}{4}\left(\frac{3}{\pi}\right)^{1/3}\int n(r)^{4/3}dr. \tag{2.63}$$

A correlation term for all densities is difficult to formulate. However, analytic expressions for the UEG correlation energy have been formluated for the high density (Gell-Mann and Brueckner, 1957) and low density (Wigner and Huntington, 1935) limit, corresponding to infinitely-weak and infinitely-strong correlations. The analytical expressions for the

high-density (eq. 2.64) and low-density (eq. 2.65) limit of the correlation energy density, respectively, are

$$E_c = A\ln(r_s) + B + r_s(C\ln(r_s) + D) \tag{2.64}$$

$$E_c = \frac{1}{2}\left(\frac{g_0}{r_s} + \frac{g_1}{r_s^{3/2}} + \dots\right) \tag{2.65}$$

where the Wigner-Seitz parameter $r_s$ is dimensionless and is defined as the radius of a sphere which encompasses exactly one electron, divided by the Bohr radius:

$$\frac{4}{3}\pi r_s^3 = \frac{1}{n} \tag{2.66}$$

Several expressions for the UEG correlation energy spanning the full range of densities have been obtained by fitting the results of accurate quantum Monte Carlo simulations (Ceperley and Alder, 1980) and parameterized for a given analytic form (Perdew and Zunger, 1981). These analytic expressions agree with the proposed from the many-body perturbation theory.

The LDA XC potential in a finite system decays asymptotically with an exponential form. However, the true XC potential decays more in a Coulombic manner, and hence more slowly than the rapid decay of the LDA XC potential. The rapid decay results in a preference to overbind ions in close proximity and ultimately yields lower calculated volumes as compared to other XC solutions. The LDA proves to be a poor approximation in applications of highly inhomogeneous densities such as atoms and molecules. Despite the inaccuracies of atoms and molecules, the LDA works remarkably well for a wide variety of condensed matter systems and agrees with experimental results within 10% for cell parameter and bulk moduli from well-converged calculations, to name a few. LDA still remains a popular method for solids due to its low computational cost and predictable shortcomings.

### 2.9.4 Generalized Gradient Approximation

An improvement in the over-binding inaccuracies by the LDA can be obtained by the Generalised Gradient Approximation (GGA) functionals. The electron density in GGA depend not just on the value of the density at a point (as in the LDA case), but also on its gradient. The XC functional for the GGA takes the form:

$$E_{xc}^{GGA}[n(r)] = \int n(r)\varepsilon_{xc}[n(r), \nabla n(r)]dr \tag{2.67}$$

where $E_{xc}$ is the integral of the electron density and the exchange-correlation has an additional fluctuation gradient term, $\nabla n(r)$.

Most GGA functionals are constructed by addition of a correction term to the LDA functionals. The addition of the extra parameter $\nabla n(r)$ allows for the GGA functional to be formulated in many various ways. Some GGA functionals contain empirical parameters whose values have been fitted to reproduce experiments or more accurate calculations (dubbed the "Chemists' functionals") such as B88 (from Becke (Becke, 1988)), FT97 (Filatov and Thiel, 1997), and LYP (Lee et al., 1988). Meanwhile, other functionals contain no empirically determined parameters (dubbed the "Physicists' functionals") such as PBE (Perdew et al., 1996), PBEsol (Perdew et al., 2008), and PW91 (Perdew and Wang, 1992).

The physics community used PW91 as the dominant GGA functional for many years until the PBE functional was developed by Perdew et al. (1996) and Perdew et al. (1998). The PBE functional is equivalent to PW91 but the formulation is much simpler. The PBE functional can be cast in terms of an enhancement factor that depends on the charge density gradient

$$E_{xc}^{PBE}[n(r)] = \int n(r)e_x(n)F_{xc}(r_s, \zeta, t) \tag{2.68}$$

where $r_s$ is the Wigner-Seitz radius, $\zeta$ is the relative spin polarization, and $t$ is a dimensionless

density gradient with $t = |\nabla n|/2\phi k_s n$ (where $\phi(\zeta) = [(1+\zeta)^{2/3} + (1-\zeta)^{2/3}/2$ and is a spin-scaling factor, and $k_s = \sqrt{4k_F/\pi a_0}$ is the Thomas-Fermi screening wave number and $a_0 = \hbar^2/2me^2$). The enhancement factor form is specified by forcing $E_{xc}^{PBE}$ to obey within well-known limits of $t \to 0$ and $t \to \infty$, which is a slowly varying limit and a rapidly varying limit (making the correlation vanish), respectively. While GGA corrects for the over-binding of LDA in condensed matter, PBE tends to under-bind by a larger amount such that PBE is not an improvement for silicate and oxide systems of interests to geophysicists (Zhang et al., 2013).

More recently, the PBEsol functional (Perdew et al., 2008) was developed for condensed matter applications, with "sol" standing for solid. The work from Perdew et al. (2008) showcases the idea that making different non-empirical choices to the enhancement factor that are more appropriate to smaller density gradients, as seen in condensed matter, produce better agreement with material properties (Holmström and Stixrude, 2015). As a result, the GGA functional PBEsol is the preferred functional of choice for the work within this thesis.

### 2.9.5 Hybrid Functionals

Hybrid functionals, also called Adiabatic Connection Method (ACM) functionals, include fractions of exact Hartree-Fock exchange energy. They are calculated as a funtional of the Kohn-Sham molecular orbitals rather than density, and are thus termed *implicit* density functionals. The exchange part of the hybrid functional consists of a linear combination of Hartree-Fock and semi-local exchange (e.g. GGA):

$$E_{xc}^{hybrid} = \alpha E_x^{HF} + (1-\alpha)E_x^{GGA} + E_c^{GGA} \tag{2.69}$$

where $\alpha$ determines the amount of Hartree-Fock and semi-local exchange. Hybrid functionals can be split into families according to the inter-electronic range at which the Hartree-Fock exchange is applied: at full range (un-screened hybrids) or at either short- or long-range

(screened or range-separated hybrids). In the case of solids, short-range functionals may be preferable for periodic solids because of faster convergence with respect to the size of the unit cell.

One of the most successful (and accurate) examples of a hybrid functional is the B3LYP 3-parameter functional, which stands for: Becke (Becke, 1988), 3-parameter (Stephens et al., 1994), and Lee-Yang-Parr (Lee et al., 1988) and incorporates the Becke 88 exchange functional and the correlation functional of Lee, Yang, and Parr. The 3-parameters defining B3LYP take the form:

$$E_{xc}^{B3LYP} = (1-a)E_x^{LSDA} + aE_x^{HF} + b\Delta E_x^B + (1-c)E_c^{LSDA} + cE_c^{LYP} \tag{2.70}$$

where $a = 0.20$, $b = 0.72$, $c = 0.81$, and $E_c^{LSDA}$ is the local spin density approximation to the correlation functional. Other popular hybrid functionals look similar to the B3LYP formalism where fractions of Hartree-Fock exchange is incorporated in various ratios to the exchange-correlation energy such as PBE0 (Adamo and Barone, 1999) and HSE (Heyd et al., 2003).

Meta-GGA (MGGA) functionals seek to improve accuracy by including the Laplacian (second derivative) of the electron density gradient. Example of MGGA include TPSS (Tao et al., 2003), M06L (Zhao and Truhlar, 2006), and SCAN (Strongly constrained and approximately normed - considered a gold-standard for water in chemistry) (Sun et al., 2015).

### 2.9.6 DFT+U

One major problem with DFT is that it poorly accounts for strongly correlated electrons in $d$ and $f$ orbitals. When using an XC-functional such as PBE or PBEsol, the Coulomb repulsion between electrons is too small, and thus the spin transition of Fe-bearing Earth materials occurs at a much lower pressure than observed in experiments. A formalism that has been proposed to improve the description of systems with strongly correlated $d$ and $f$

electrons is the DFT+U method, or also known as the Hubbard +U correction - a corrective functional inspired by the Hubbard model (an approximate model used to describe the transition between conducting and insulating systems). The +U is an additional term that makes two electrons within the same sub-level energetically unfavorable. Note: often times the +U method will be seen as LDA+U, where this indication denotes a correction to the approximate DFT functional, such as LDA in this case. However, it can also be applied to the Local Spin Density Approximation (LSDA) or GGA functional.

The DFT+U is one of the simplest approaches formulated to improve the description of the ground state of correlated systems (Himmetoglu et al., 2014). It is based on describing the strongly correlated electronic states using the Hubbard model (Hubbard, 1964a,b, 1965, 1967a,b) and treating the rest of the valence electrons at the standard approximation level of DFT functionals. Within LDA+U, the total energy of the system is written as:

$$E_{LDA+U}[n(r)] = E_{LDA}[n(r)] + E_{Hub}[\{\rho^{\sigma}_{mm'}\}] - E_{dc}[\{n^{\sigma}\}] \tag{2.71}$$

where $m, m'$ are the projection of the orbital momentum ($m, m' = -2, -1, ..., 2$ in the case of $d$ electrons), $\rho_{ij}$ is the density matrix, which in the case of an isolated ion is diagonal with eigenvalues equal to the occupation numbers of the orbitals, $E_{LDA}$ is the DFT total energy functional being corrected, $E_{Hub}$ contains the Hubbard Hamiltonian to model corrected states, and $E_{dc}$ is the "double-counting (dc)" which occurs from the additive nature of $E_{LDA}$ and $E_{Hub}$. $E_{dc}$ models the contribution of correlated electrons to the DFT energy as a mean field approximation of $E_{Hub}$, but the dc functional is not uniquely defined. As such, different possible formulations have been implemented and used in various cases, but two popular choices for the dc term have led to the so-called "around mean-field" (AMF) and "full localized limit" (FLL). As the names suggest, the first is suitable to treat fluctuations of the local density in systems characterized by quasi-homogeneous distribution of electrons (as in metals and weakly correlated systems), whereas the second is suitable for materials whose electrons are more localized on specific orbitals.

The flavor used in the majority of this dissertation work is the simplified (rotationally invariant) approach introduced by Dudarev et al. (1998), taking the form (Dudarev et al., 1998):

$$E_{DFT+U} = E_{LSDA} + \frac{\bar{U} - \bar{J}}{2} \sum_{\sigma} \left[ \left( \sum_{m} \rho^{\sigma}_{m,m} \right) - \left( \sum_{m,m'} \rho^{\sigma}_{m,m'} \rho^{\sigma}_{m',m} \right) \right] \tag{2.72}$$

where $\bar{U}$ and $\bar{J}$ are the spherically averaged matrix elements of the screen Coulomb electron-electron interaction, and $\hat{n}^{\sigma} = \hat{n}^{\sigma}\hat{n}^{\sigma}$ which could be understood as adding a penalty functional to the semi-local total energy expression that forces the on-site occupancy matrix in the direction of idempotency (Dudarev et al., 1998).

The addition of the +U term results in a spin-transition pressure occurring at higher pressures than when calculated without it. This leads to the low-spin phase being energetically less favorable until much higher pressures are reached. The method primarily used in this work to calibrate the spin-transition pressure and the $U - J$ interaction term is by comparison to experimental observations. Self-consistent methods of calculating the $U - J$ interaction term exists, as in the work published by Cococcioni and De Gironcoli (2005) (Cococcioni and De Gironcoli, 2005). This method is not useful for our purposes because it is not generalizable to the dynamical high-temperature state in which each atom would in general have a different vale of $U$ at each time step.

## 2.10 Born-Oppenheimer Approximation

The German physicist Max Born won the 1954 Nobel Prize in Physics for his "fundamental research in quantum mechanics, especially in the statistical interpretation of the wave function," and J. Robert Oppenheimer never won the Nobel Prize, despite being nominated three times. The work of Born and Oppenheimer in 1927 led to an approximation used in molecular dynamics simulations (described in chapter 3). The Born-Oppenheimer approxi-

mation is an assumption that the wave functions of nuclei and electrons in a molecule can be treated separately due to the mass of the nuclei being substantially larger than the mass of the electrons (Born and Oppenheimer, 1927). Due to the mass differences, the same momentum applied to the nuclei and electrons would result in the nuclei moving more slowly than the electrons.

The total wave function of a molecule can be written as the product of the electronic and nuclear (vibrational and rotational) wave functions:

$$\Psi_{total} = \Psi_{electronic}\Psi_{nuclear} \tag{2.73}$$

which can be separated into an electronic and nuclear term in the Hamiltonian operator of the system (cross-terms are neglected for efficiency). To begin the approximation, the nuclear kinetic energy $T_n$ is neglected by subtraction of the total molecular Hamiltonian

$$H = H_e + T_n. \tag{2.74}$$

$$T_n = -\sum_A \frac{1}{2M_A}\nabla_A^2 \tag{2.75}$$

Nuclear positions are no longer variable in the remaining electronic Hamiltonian $H_e$, but are constant. However, the electron-nucleus interactions are not removed. The electronic Schrödinger equation now takes the form

$$H_e(\mathbf{r},\mathbf{R})\chi(\mathbf{r},\mathbf{R}) = E_e\chi(\mathbf{r},\mathbf{R}) \tag{2.76}$$

where $\chi(\mathbf{r},\mathbf{R})$ is the electronic wave function for given positions of nuclei and $\mathbf{R}$ is fixed. $\mathbf{r}$ represents all electronic coordinates, $\mathbf{R}$ represents all nuclear coordinates, and $E_e$ is the electronic energy eigenvalue (or potential energy surface).

The second step of the Born-Oppenheimer Approximation reintroduces the nuclear kinetic energy term $T_n$, and the Schrödinger equation for the nuclear motion is solved takes the form:

$$[T_n + E_e(\mathbf{R})]\phi(\mathbf{R}) = E\phi(\mathbf{R}). \tag{2.77}$$

This step involves separation of vibrational, translation, and rotational motion, which is achieved by applying the Eckart conditions (Eckart, 1935; Sayvetz, 1939). The nuclear position is an average over electronic configurations of the sum of the electron-nuclear and internuclear electronic potentials according to the Hellmann-Feynman theorem

$$\frac{dE_\lambda}{d\lambda} = \left\langle \psi_\lambda \left| \frac{d\hat{H}_\lambda}{d\lambda} \right| \psi_\lambda \right\rangle \tag{2.78}$$

where $\lambda$ is a continuous parameter.

## 2.11 Hellmann-Feynman Theorem

The Hellmann-Feynman theorem (Hellmann, 1937; Feynman, 1939) relates the total energy of the system with respect to a parameter and the expectation value of the derivative of the Hamiltonian with respect to the same parameter:

$$\frac{dE_\lambda}{d\lambda} = \left\langle \psi_\lambda \middle| \frac{d\hat{H}_\lambda}{d\lambda} \middle| \psi_\lambda \right\rangle \tag{2.79}$$

where $\hat{H}_\lambda$ is a Hermitian operator depending on a continuous parameter $\lambda$, and $E_\lambda$ is the energy (eigenvalue) of the eigenstate $|\psi_\lambda\rangle$, an eigenfunction of the Hamiltonian. We can utilize this theorem to calculate the forces exerted on the ions from the derivative of the total energy with respect to $r_i$, the chosen $\lambda$ parameter, where

$$F_i = -\frac{\partial E}{\partial r_i} = -\left\langle \psi \middle| \frac{\partial \hat{H}}{\partial r_i} \middle| \psi \right\rangle \tag{2.80}$$

This theorem requires that the wavefunction be an eigenfunction of the Hamiltonian and that the identity of normalized wavefunctions is employed, meaning that the derivatives of the overlap of the wavefunction with itself must be equal to zero. These conditions can be written out as

$$\hat{H}_\lambda |\psi_\lambda\rangle = E_\lambda |\psi_\lambda\rangle \tag{2.81}$$

$$\langle \psi_\lambda | \psi_\lambda \rangle = 1 \Rightarrow \frac{d}{d\lambda} \langle \psi_\lambda | \psi_\lambda \rangle = 0 \tag{2.82}$$

## 2.12 Mermin Functional

Solutions to the electronic structure in the Hohenberg-Kohn theory are treated as being in the ground state, but the need to account for the finite temperature of electrons increases with various applications of the theory. David Mermin, an American solid-state physicist, furthered the work of Hohenberg and Kohn by including finite temperatures (non-zero) through the Mermin functional (Mermin, 1965). His proof shows that in the grand canonical ensemble at a given temperature and chemical potential, no two $v(r)$ have the same equilibrium density, or that $v(r)$ is uniquely determined by $n(r)$. This fact enables one to define a functional of the density $F[n(r)]$ that is independent of $v(r)$, such that $\Omega = \int v(r)n(r)dr + F[n(r)]$ is at a minimum and equal to the grand potential when $n(r)$ is the equilibrium density in the grand canonical ensemble in the presence of $v(r)$.

To begin this proof, we will work in the grand canonical ensemble at a fixed temperature and chemical potential and show that no two $v(r)$ give the same equilibrium density. We begin with the grand potential analogous to that of the ground state energy. If

$$\Omega[\rho] = \mathrm{Tr}\rho\bigg(H - \mu N + \frac{1}{\beta} ln[\rho]\bigg), \tag{2.83}$$

then the grand potential

$$\Omega = -\frac{1}{\beta} \ln \mathrm{Tr} e^{-\beta(H-\mu N)} \tag{2.84}$$

is given by $\Omega[\rho_0]$ where $\rho_0$ is the grand canonical density matrix

$$\rho_0 = \frac{e^{-\beta(H-\mu N)}}{\mathrm{Tr} e^{-\beta(H-\mu N)}} \tag{2.85}$$

The functional satisfies $\Omega[\rho] > \Omega[\rho_0]$, $\rho \neq \rho_0$ for all density matrices $\rho$. We will now consider a grand canonical ensemble of electrons in an external potential $v(r)$ and recall that the Hamiltonian is $H = T + V + U$ where

$$T = \frac{\hbar^2}{2m} \int \nabla\psi^*(r)\nabla\psi(r)dr \tag{2.86}$$

$$V = \int v(r)\psi^*(r)\psi(r)dr \tag{2.87}$$

$$U = \frac{1}{2} \int \frac{e^2}{|r - r'|} \psi^*(r)\psi^*(r')\psi(r')\psi(r)drdr'. \tag{2.88}$$

The equilibrium electron density is then

$$n(r) = \mathrm{Tr}\rho_0\psi^*(r)\psi(r) \tag{2.89}$$

which appears to be a functional of $v(r)$. However, Mermin proves that $v(r)$ is uniquely determined by $n(r)$ through the variational principle. We consider another potential $v'(r)$ that gives rise to the same density $n(r)$ and an associated $H'$, $\rho'$, and $\Omega'$. Because $v'(r) \neq v(r)$ and $\rho'_0 \neq \rho_0$, we have

$$\Omega' = \mathrm{Tr}\rho_0'\left(H' - \mu N + \frac{1}{\beta} ln[\rho_0']\right) < \mathrm{Tr}\rho_0\left(H' - \mu N + \frac{1}{\beta} ln[\rho_0]\right) = \Omega + \mathrm{Tr}\rho_0(V' - V) \quad (2.90)$$

such that

$$\Omega' < \Omega + \int dr[v'(r) - v(r)]n(r) \quad (2.91)$$

When the primed and unprimed quantities are interchanged, the reasoning remains valid and yields

$$\Omega < \Omega' + \int dr[v(r) - v'(r)]n(r). \quad (2.92)$$

The sum of the two equation leads to the contradiction

$$\Omega' + \Omega < \Omega + \Omega' \quad (2.93)$$

proving that only one $v(r)$ can result in a given $n(r)$. We can see that this is similar to the derivation of the first Hohenberg-Kohn theorem where the external potential is a unique functional of $n(r)$ and demonstrates that the extension of the Hohenberg-Kohn theory to finite temperatures remains consistent.

# CHAPTER 3

# Methods

In this chapter, I will cover various methods used in my dissertation work. These methods include solution of the electronic structure problem, generation of dynamical trajectories of large sets of atoms responding to Hellman-Feynman forces under various statistical mechanical ensembles, and interpretation of these molecular dynamics simulations, including analysis of time series, computation of thermodynamic properties, and analysis of dynamics.

## 3.1 Electronic Structure

The solution of the electronic structure problem is central to my work. It is the most time-consuming part of my computations by far as it must be solved at every time step of my dynamical trajectories. Efficiency is therefore an important consideration, and modern density functional theory codes make use of a variety of fundamental physical concepts to develop fast numerical strategies for solving the Kohn-Sham equations. These numerical strategies have been developed over the last few decades and help account for the widespread use of density functional theory to study material properties in virtually all fields of science. Much of the development below is general and applies to most density functional theory codes, although I make occasional reference to the particular one that I have used: the Vienna *ab initio* Simulation Package (VASP) (Kresse and Furthmüller, 1996).

### 3.1.1 Plane Wave Basis Set

All of my calculations employ periodic boundary conditions, these being the natural choice for crystal lattices, but also useful for the study of materials lacking long-range order such as liquids. In a periodic system, the Bloch theorem states that the wavefunction can be represented by

$$\psi_{\mathbf{k}}(\mathbf{r}) = u_{\mathbf{k}}(\mathbf{r})e^{i\mathbf{k}\cdot\mathbf{r}} \tag{3.1}$$

where $e^{i\mathbf{k}\cdot\mathbf{r}}$ is a plane wave and $u_k(\mathbf{r})$ is a periodic function

$$u_{\mathbf{k}}(\mathbf{r}) = u_{\mathbf{k}}(\mathbf{r}+\mathbf{R}). \tag{3.2}$$

where $\mathbf{R}$ is a lattice vector. The Bloch theorem is also sometimes stated in the equivalent form

$$\psi_{\mathbf{k}}(\mathbf{r}+\mathbf{R}) = e^{i\mathbf{k}\cdot\mathbf{R}}\psi(\mathbf{r}) \tag{3.3}$$

The Bloch wave vector $\mathbf{k}$ must be real by imposing an appropriate boundary condition on the wave functions. The condition introduced is the Born-von Karman boundary condition, named after Max Born and Theodore von Karman, which imposes the restriction that the wave function must be periodic on a certain Bravais lattice. We can generalize the periodic boundary condition to:

$$\psi(\mathbf{r}+N_iR_i) = \psi(\mathbf{r}) \tag{3.4}$$

where $N_i$ are integers.

Because $u_{\mathbf{k}}(\mathbf{r})$ is periodic from equation 3.2, it can be represented as a wave in the form

$$u_{\mathbf{k}}(\mathbf{r}) = \sum_{\mathbf{G}} c_{\mathbf{k},\mathbf{G}} e^{i\mathbf{G}\cdot\mathbf{r}} \tag{3.5}$$

where $c_{k,G}$ is a constant and $\mathbf{G}$ is a reciprocal lattice vector. The wave function can now be represented in terms of a sum of plane waves

$$\psi_{\mathbf{k}}(\mathbf{r}) = \sum_{\mathbf{G}} c_{\mathbf{k}+\mathbf{G}} e^{i(\mathbf{k}+\mathbf{G})\cdot\mathbf{r}} \tag{3.6}$$

At first glance, the summation suggests an infinite series that requires an infinite number of plane waves to solve the wave function accurately. In practice only a finite number of plane waves are needed to demonstrate convergence to the infinite basis set size limit. The finite size of the basis set is expressed in terms of the kinetic energy

$$\frac{\hbar^2}{2m}|k+G|^2 \tag{3.7}$$

so that all plane waves are included which satisfy

$$\frac{\hbar^2}{2m}|k+G|^2 < E_{\text{cutoff}} \tag{3.8}$$

where $E_{\text{cutoff}}$ is the cutoff energy. Testing must be performed for every system to determine a value of the cutoff energy that yields accurate results. For much of the work done in this thesis, an energy cut-off of 500 eV was sufficient. However, for unit cell systems containing hydrogen, we found an energy cut-off of 1000 eV was required.

### 3.1.2 Brillouin Zone Sampling

Sampling the Brillouin zone is constrained by how one specifies the Bloch vectors $\mathbf{k}$. Computing the energy at many values of $\mathbf{k}$ (known as k-points) is necessary to compute the potential energy and charge density in the Kohn-Sham equations. Obtaining accurate energy calculations can be done by either having a dense mesh of k-points within the Brillouin

zone where electronic states are sampled at regular intervals, or one can increase the number of atoms in the simulations. Having a larger system results in a smaller Brillouin zone in reciprocal space, which requires fewer k-points to accurate sample the energies. The Brillouin zone size is determined by

$$V_{BZ} = \frac{4\pi^3}{V_{cell}} \tag{3.9}$$

where $V_{cell}$ is the volume of the unit cell in real space. For static (ionic relaxation) simulations, small systems containing only a few atoms typically need many k-points such as a 4 x 4 x 4 grid. In this example, the Brillouin zone is sampled at 64 regularly spaced points. Metallic systems with small unit cells can require considerably more k-points to obtain accurate results.

The calculation of the electronic density of states and very accurate calculations of the total energy in the limit of zero temperature for semi-conductors and insulators can be done using the tetrahedron method with Blöchl corrections (Blöchl, 1994). If the size of the cell is large, a small k-point mesh such as a 2 x 2 x 2 grid is acceptable. In our semi-conductor density of states calculations, our cell is small ($\varepsilon$-FeOOH unit cell), so we choose a 20 x 20 x 20 k-point mesh a result.

In molecular dynamics simulations containing hundreds of atoms, using just one k-point [the $\Gamma$-point for which $\mathbf{k} = (0, 0, 0)$] is reasonable. The size of the simulation cell reduces the Brillouin zone in addition to saving on computational expense. For the majority of molecular dynamics simulations done in this work, sampling the $\Gamma$-Point has proven to be sufficient for energy convergence.

### 3.1.3 Pseudopotentials

A pseudopotential was first introduced by Hans Hellmann in 1934 (Schwerdtfeger, 2011). In principle, DFT tells us how to calculate the electron orbitals and eigenvalues, but the prac-

tical implementation is technically difficult. A problem that arises is that the core orbitals are strongly localized around the nuclei and have very deep binding energies. However, the valence orbitals are more weakly bound and extend throughout the material. The pseudopotential theory exploits these difficulties and recognizes that the core electrons play very little or no role in the material energetics, wihch instead depends almost entirely on the valence electrons. The theory recognizes the manner in which valence electrons are scattered by atomic cores and can be accurately mimicked by weak valence-core potentials (these are the pseudopotentials). The theory also showcases this point by showing that the strong potential attracting the valence electrons to the cores is largely cancelled out by the effects of orthogonality between the valence and the core states, which have the effect of a repulsive potential (Gillan et al., 2006).

As a result, the total energy of the material can be calculated by solving the Kohn-Sham equations for the valence electrons alone, which interact with the atomic cores via pseudopotentials (figure 3.1).

Two common forms of the pseudopotential used in modern codes are *norm-conserving* and *ultra-soft*. Pseudopotentials with a larger cut-off radius are said to be *softer*, which are considerably more efficient, but in practice are less *transferable* (where transferable means less accurate to reproduce realistic features in different environments. i.e. when the atom is transferred from one environment to another). A property of norm-conserving pseupotentials is that they are transferable, and ultra-soft pseudopotentials are considerably more efficient by requiring a lower energy cut-off to the plane waves when compared to norm-conserving ones. In practice, they are at least as transferable, if not more so.

Closely related to the ultra-soft pseudopotential is an all-electron technique known as the Augmented Plane Wave (APW) method The eigenfunctions of the Kohn-Sham equation are represented within spheres surrounding the nuclei by spherical harmonics multiplied by radial functions, and the region between the spheres by plane wave (Gillan et al., 2006). The potential is assumed to be spherically symmetric in the muffin-tin region and constant in

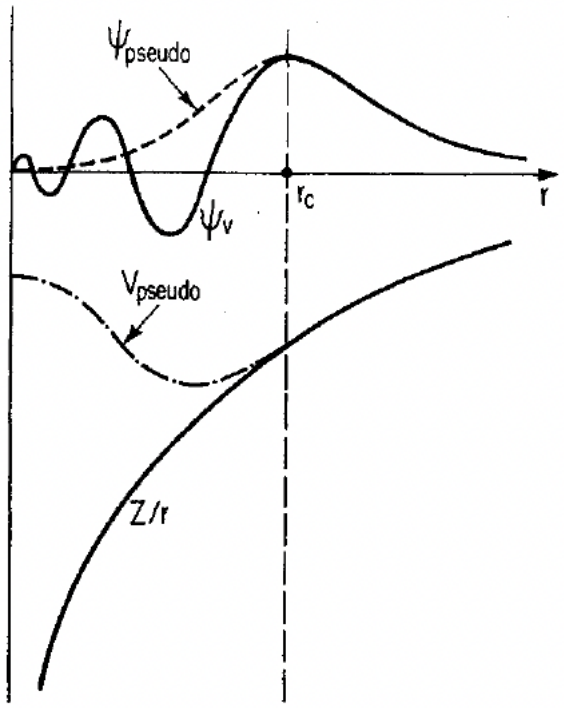


**Figure 3.1:** A schematic illustration of an all electron (solid lines) and pseudoelectron (dashed lines) potential and their corresponding wave functions, taken from Payne et al. (1992). The radius at which all-electron and pseudoelectron values match is designated as $r_c$.

the interstitial region: the so-called muffin-tin picture. Wave functions are constructed by matching solutions of the Schrödinger equation within each sphere with plane-wave solutions in the interstitial region. APW was used in the first density functional theory computations of deep Earth materials, which were performed at UCLA (Bukowinski, 1977). APW has been proven to be useful in calculating electrical properties such as band properties, superconductivity, and field gradients in complex systems (Mattheiss and Hamann, 1986; Blaha et al., 1985). However, this method is computationally expensive and inefficient for large or long duration calculations. The inefficiency is due to the non-linearity of the function defining the core region, in which the energy is a function of and requires an iterative solving

approach. While the linearized versions (LAPW) mitigates some of these challenges, and continues to be used to explore the behavior of matter at extremely high pressure where the pseudopotential approximation tends to fail (Stixrude et al., 1994) it is still much more cumbersome to use than the methods I focus on in this thesis.

It goes without say that it would be impossible to use plane-wave basis sets without pseudopotentials. The core orbitals vary rapidly on extremely short length scales, which would require a large amount of plane waves to represent them. This representation of valence and conduction orbitals would also be equally impossible because orthogonality requires these too to vary rapidly in the region of atomic cores. Pseudopotentials solve both of these problems because of the smoothness in the core region makes the pseudo-wavefunctions of valence and conduction orbitals in these regions smooth as well.

### 3.1.4 Projector Augmented Wave Method

The projector augmented wave method (PAW) is a generalization of the pseudopotential and LAPW methods, which allows DFT to be computed with greater efficiency (Blöchl, 1994; Kresse and Joubert, 1999). As mentioned earlier, the valence wave functions tend to have rapid oscillations near the ion cores due to the demand of orthogonality to core states. As a result, this becomes problematic because it requires many Fourier components to accurately describe the wave function. The PAW method addresses this problem by transforming the rapidly oscillating wave functions into smooth wave functions, making it more computationally efficient and providing a way to calculate all-electron properties from the smooth wave functions.

A linear transformation $\mathcal{T}$ transforms the fictitious pseudo wave function $|\tilde{\psi}\rangle$ to the all-electron wave function $|\psi\rangle$:

$$|\psi\rangle = \mathcal{T}|\tilde{\psi}\rangle \tag{3.10}$$

We let $|\tilde{\psi}\rangle$ and $|\psi\rangle$ differ only in the regions in the ion core by writing:

$$\mathcal{T} = 1 + \sum_R \hat{\mathcal{T}}_R \tag{3.11}$$

where $\hat{\mathcal{T}}_R$ is non-zero only within some spherical augmentation region $\Omega_R$ enclosing atom $R$. Around each atom, it is convenient to expand the pseudo wave function into pseudo partial waves:

$$|\tilde{\psi}\rangle = \sum_i |\tilde{\phi}_i\rangle c_i \tag{3.12}$$

within $\Omega_R$. The coefficients $c_i$ can be written as an inner product with a set of "projector" functions $|p_i\rangle$ due to the operator $\mathcal{T}$ being linear:

$$c_i = \langle p_i|\tilde{\psi}\rangle \tag{3.13}$$

where $\langle p_i|\tilde{\phi}_j\rangle = \delta_{ij}$. The all-electron partial waves $|\phi_j\rangle = \mathcal{T}|\tilde{\phi}_i$ are typically chosen to be solutions to the Kohn-Sham equation for an isolated atom. As a result, the transformation $\mathcal{T}$ is specified by three quantities:

1.) A set of all-electron partial waves, $|\phi_i\rangle$

2.) A set of pseudo partial waves, $|\tilde{\phi}_i$

3.) A set of projector functions, $|p_i$

and can be explicitly written as:

$$\mathcal{T} = 1 + \sum_i (|\phi_i\rangle - |\tilde{\phi}_i\rangle)\langle p_i| \tag{3.14}$$

The pseudo partial waves are equal to the all-electron partial waves outside of the augmentation regions, but they can be any smooth continuations (such as a linear combination of polynomials or Bessel functions) inside of the spheres.

The work in this dissertation uses the PAW method, and the valence properties for each element used are given in table 3.1

| **Element** | **Valence electrons** | **Core Radius (Å)** |
|---|---|---|
| Fe | 14 | 1.164 |
| Mg | 8 | 1.058 |
| Si | 4 | 1.312 |
| O | 6 | 0.820 |
| H | 1 | 0.370 |

**Table 3.1:** Electronic properties of elements used in this dissertation. The core radius is the Wigner-Seitz radius (in Å) for each atom type.

### 3.1.5 Convergence Energy

The break condition in the electronic self-consistency loop within most DFT codes can be chosen. This value is the difference between the total energy change and the band-structure-energy change between the current and previous electronic step. The convergence speed decays exponentially in most cases, as long as the cost for a few iterations is small, and values below $10^{-5}$ eV are not necessary. The bulk of this work uses an energy convergence of $10^{-5}$ eV. However, this value is decreased to $10^{-8}$ eV for our finite difference calculations (e.g. phonons and elastic tensor) to obtain very accurate and precise results.

### 3.1.6 Electronic Bands

Before talking about electronic bonds in solids, let us first consider the formation of a lithium-row diatomic molecule. As the two atoms are brought together, the total number of electron states is conserved with orbitals coupling to each other and forming simple bonding and anti-bonding combinations (figure 3.2).

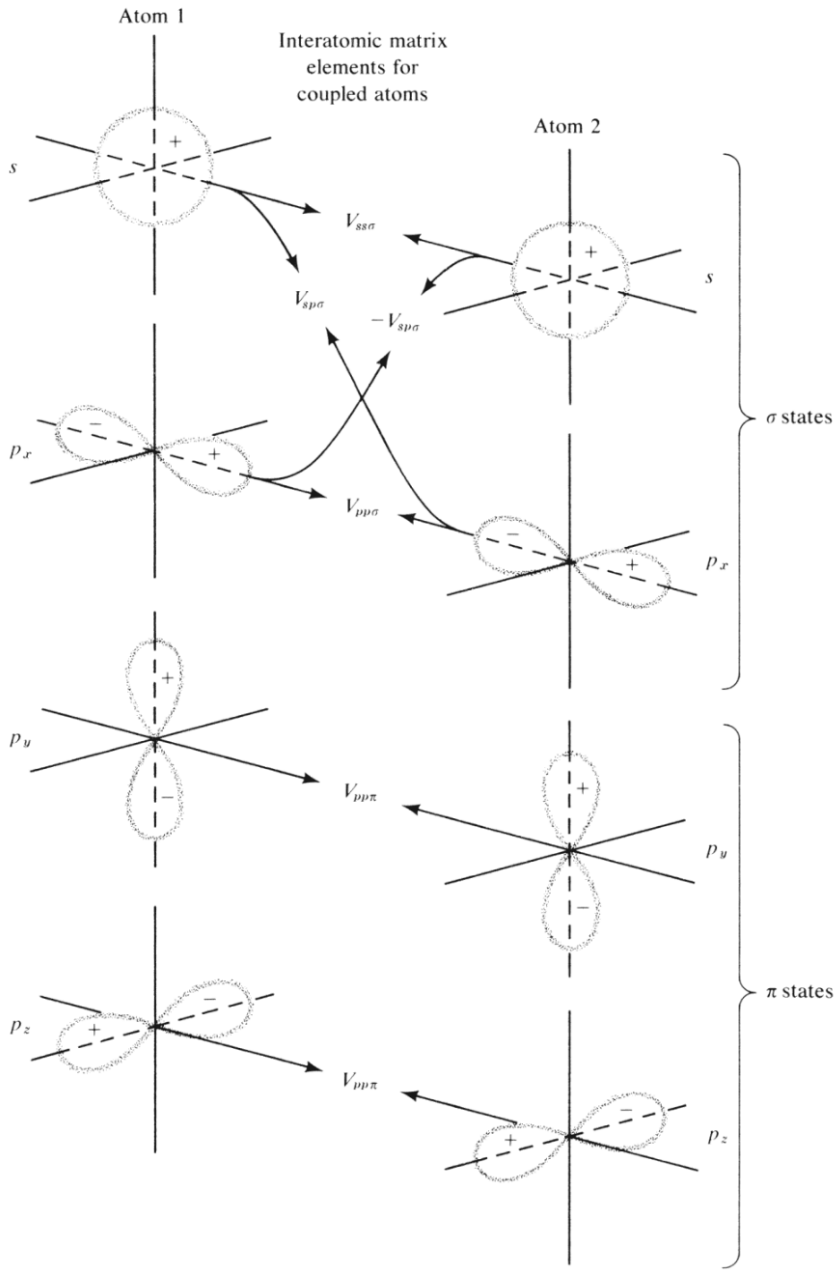


**Figure 3.2:** Atomic orbital coupling in lithium-row diatomic molecules, and the resultant bond designations on the right taken from Harrison (2012).

The formation of solids behave similarly to the formation of molecules. However, the number of states in solids is far greater than that of molecules (on the order of Avogadro's

constant, $N_A$, $10^{23}$), and one must also consider that there is an atomic *s*- and *p*-orbital for each atom (and *d*-orbitals for Fe in this thesis). The difficulty of solving a problem with 4 x $10^{23}$ equations can be circumvented by considering the simplicity of a crystalline solid system where periodicity can be utilized. The atomic energy levels are now split into *bands* when the atoms are brought together, analogously to the states in diatomic molecules and in figure 3.3. Now, rather than splitting into single bonding and anti-bonding states, the atomic levels are split into entire bands of states that are distributed between the extreme bonding and anti-bonding limits (Harrison, 2012).

The choice in the number of electronic bands strongly depends on the system. In VASP, the bands defines the number of Kohn-Sham orbitals in the calculation. The minimum requirement for VASP requires all occupied states plus one empty band; However, by default, VASP sets the number of bands equal to half the number of valence electrons plus half the number of ions. Although the empty states do not contribute to the total energy in electronic minimization calculations, empty states are required for better convergence due to its effect on the matrix-diagonalization algorithm.

### 3.1.7 Parallelization

The computational time for a single VASP run varies with respect to the number of atoms in the system, the number of valence electrons per atom, the number of k-points, and the size of the basis set, in addition to the speed of the processing unit(s). Because a single core cannot perform enough operations for complex problems, parallelization is necessary for computational efficiency. Most of this work was carried out locally on an 8-core MacBook Pro or through High Performance Computing (HPC) such as the Hoffman2 Shared Cluster provided by UCLA Institute for Digital Research and Education's Research Technology Group.

Running VASP in parallel on CPUs requires proper usage of the INCAR flags, NPAR or NCORE, which efficiently determines the number of bands that are treated in parallel.

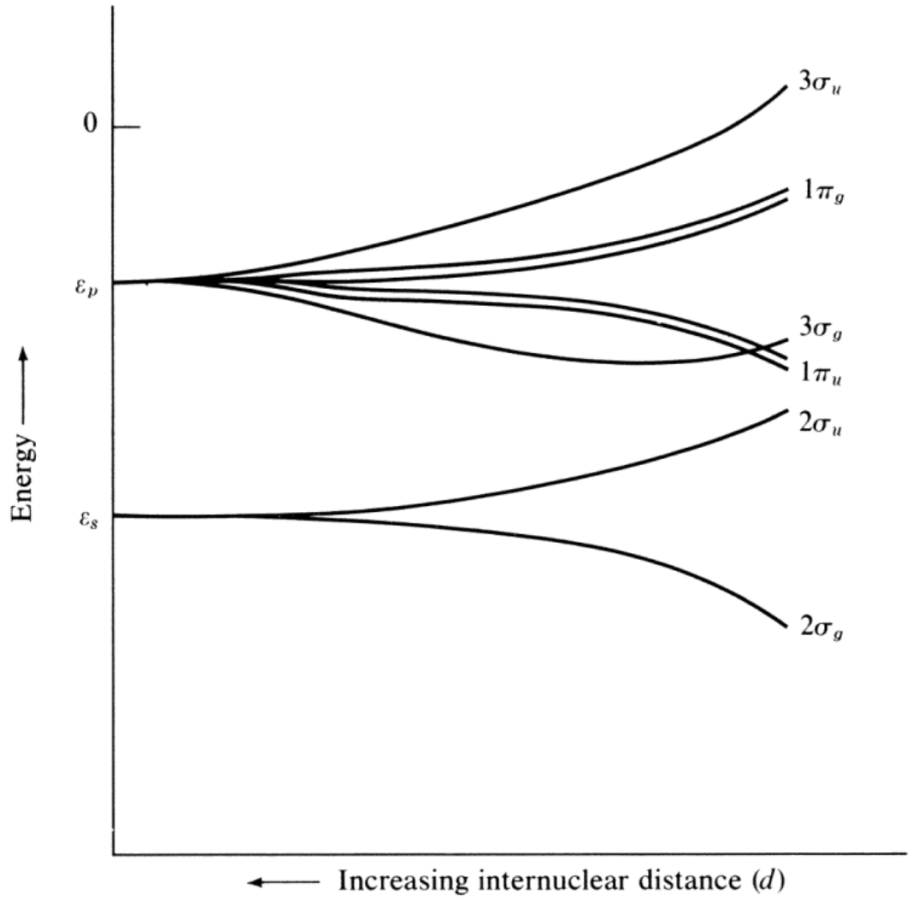


**Figure 3.3:** The molecular energy levels as a pair of lithium-row atoms is brought together (Harrison, 2012). In this example, the $\pi$ and $\sigma$ notations represent $\pi$ states and $\sigma$ states. $\pi$ states result from $p_y$-orbital coupling and $p_z$-orbital coupling in atom 1 and atom 2. $\sigma$ states result from the $p_x$-orbital and s-orbital coupling in atom 1 and atom 2. The notations $g$ and $u$ stand for *gerade* and *ungerade* - German for "even" and "odd", respectively - and depend on whether the wave function of the orbital is even or odd when inverted through the midpoint of the atoms.

For massively parallel systems and modern multi-core machines, VASP strongly recommends setting the NPAR flag to

$$\text{NPAR} \approx \sqrt{\#\text{ of Cores}} \tag{3.15}$$

or setting NCORE to

$$\text{NCORE} = \#\text{ of cores per compute node} \tag{3.16}$$

resulting in performance improvement by a factor of four.

If a simulation requires more than the Γ-point sampling of k-points in the Brillioun zone, the flag KPAR determines the number of k-points run in parallel. It is suggested that the value of KPAR be an integer divisor of the total number of cores.

As of VASP 6.3.0 (the latest version of VASP used in this work), parallelization on a GPU requires slight differences in INCAR setup. For performance reasons, the use of parallel Fast Fourier Transforms (FFTs) of the wave functions (NCORE > 1) should be avoided, and instead, the OpenACC GPU port of VASP will switch NCORE = 1 by default if a value other than 1 is specified. GPU testing of VASP, performed through the Pittsburgh Supercomputing Center Bridges-2, show that the flag NSIM is an important parameter for increasing performance (Table 3.2). Others, such as researchers at NVIDIA and Peter Larsson at the National Supercomputer Centre at Linköping University, report similar findings for VASP GPU performance and suggest that the GPU calculation will run faster with increased values of NSIM. However, the drawback is that the memory consumption increases with higher NSIM as well, so the user is encouraged to increase the number of NSIM until the physical memory is run out. A general suggestion is

$$\text{NSIM} = \frac{\text{NBANDS}}{2 * \#\text{ of cores}} \tag{3.17}$$

to fully utilize the GPUs.

| Number of GPUs | NSIM | mpirun -n | Timesteps | Runtime (min) |
|---|---|---|---|---|
| 1 | 1 | 2 | 29 | 30 |
| 1 | 4 | 2 | 55 | 30 |
| 1 | 4 | 4 | 55 | 30 |
| 1 | 8 | 2 | 56 | 30 |
| 1 | 8 | 4 | 57 | 30 |
| 1 | 12 | 2 | 59 | 30 |
| 1 | 16 | 2 | 61 | 30 |
| 2 | 36 | 4 | 104 | 30 |
| 8 | 72 | 8 | 202 | 30 |

**Table 3.2:** VASP GPU convergence tests run on Pittsburgh Supercomputing Center Bridges-2 GPU nodes. One node includes 8 NVIDIA Tesla V100 GPUs. The table lists a small sample of convergence tests done on a system comprised of 55 Fe atoms where *ab initio* Molecular Dynamics simulations were performed. *Note: Performance tests were done using VASP6 ported from CUDA-C between years 2021 - 2022. Recent work has found that the OpenACC GPU port has significantly better performance with respect to increased NSIM values.*

## 3.2 Molecular Dynamics Simulations

All discussion of DFT thus far has been in regards to systems at static conditions, which refers to absolute zero temperature (0 K) and in the absence of zero-point motion. In order to investigate systems at high temperatures, we perform Molecular Dynamics (MD) simulations where the temperature of interest may be specified. This temperature is then used to create a Maxwell-Boltzmann distribution of velocities (Maxwell, 1860a,b; Boltzmann, 1872, 1877), which are randomly assigned to the particles from the probability distribution

$$f(v) = \left[\frac{m}{2\pi k_B T}\right]^{3/2} 4\pi v^2 \exp\left(-\frac{mv^2}{2k_B T}\right) \tag{3.18}$$

where $m$ is the mass of the particle, $v$ is the velocity, $k_B$ is Boltzmann's constant, and $T$ is temperature.

Im the micro-canonical or $NVE$ ensemble (constant number of atoms $N$, volume $V$, and internatl energy $E$) MD simulations propagate ionic trajectories according to Newton's equations of motion

$$F_i = m_i a_i \tag{3.19}$$

where $F_i$ is the force driving the acceleration $a_i$ of a particle with mass $m_i$, and the forces acting on the nuclei can be computed from the Hellman-Feynman theory.

### 3.2.1 Velocity Verlet Algorithm

While the forces are calculated quantum mechanically from the Hellman-Feynman theory, the propagation of trajectories is calculated classically according to Newton's equations of motion. Stability of the propagation is an important numerical issue. Consider the Verlet algorithm (Verlet, 1967): a particle with an initial position $r_{i0}$ and velocity $v_{i0}$ with a force $F_i$ for a time interval $\Delta t$, results in a new position $r_i$

$$r_i = r_{i0} + (v_{i0}\Delta t + \frac{1}{2} a_i \Delta t^2) \tag{3.20}$$

The acceleration of the particle $a_i$ is given by $a_i = F_i/m_i$, where $m_i$ is the mass of the particle. If we assume that $r_i(t)$ is the particle's current position at time $t$, then we can compute the Taylor expansions of the position in different time directions $r_i(t \pm \Delta t)$:

$$r_i(t + \Delta t) = r_i(t) + v_i(t)\Delta t + \frac{a_i(t)\Delta t^2}{2} + \frac{b_i(t)\Delta t^3}{6} + O(\Delta t^4) \tag{3.21}$$

$$r_i(t-\Delta t) = r_i(t) - v_i(t)\Delta t + \frac{a_i(t)\Delta t^2}{2} - \frac{b_i(t)\Delta t^3}{6} + O(\Delta t^4) \tag{3.22}$$

where $b_i$ is the third derivative of the position with respect to time. Addition of equations 3.21 and 3.22 results in the velocity dropping out of the equation, giving us the position:

$$r_i(t+\Delta t) = 2r_i(t) - r_i(t-\Delta t) + a_i(t)\Delta t^2 + O(\Delta t^4) \tag{3.23}$$

and subtracting equation 3.22 from 3.21 results in the velocity:

$$v_i(t) = \frac{1}{2\Delta t}\Big[r_i(t+\Delta t) - r_i(t-\Delta t)\Big] + O(\Delta t^3) \tag{3.24}$$

A problem that arises with the Verlet algorithm is the requirement to know the positions at a given time direction at $t \pm \Delta t$ to determine the velocity at a given $t$. Additionally, the velocity always lags a step behind the positions due to the discretization method, causing problems with velocity-dependent quantities. Alternatively, if one simply integrates equation 3.20, this would lead to the following dynamical trajectory (Euler method):

$$r_i(t+\Delta t) = r_{i0}(t) + (v_{i0}(t)\Delta t + \frac{1}{2}a_i(t)\Delta t^2) \tag{3.25}$$

$$v_i(t+\Delta t) = v_i(t) + a_i(t)\Delta t \tag{3.26}$$

and lead to unstable results depending on the step size chosen.

These problems are circumvented by the **velocity Verlet algorithm**, which is known to be very stable. The velocity and position are calculated at the same value of the time variable, based on central differences. In this method, the forces need to be determined at the updated position:

$$F_i(t+\Delta t) = F_i(r_i(t+\Delta t)) \tag{3.27}$$

in which the position and velocity are simultaneously determined at $r(t + \Delta t)$ as:

$$r_i(t) = r_i(t + \Delta t) - v_i(t + \Delta t)\Delta t + \frac{F_i(t + \Delta t)}{2m_i}\Delta t^2 \tag{3.28}$$

$$v_i(t + \Delta t) = v_i(t) + \frac{F_i(t) + F_i(t + \Delta t)}{2m_i}\Delta t \tag{3.29}$$

### 3.2.2 Thermostat and Barostat

Most of the computational work done in this thesis was calculated in the canonical ensemble ($NVT$), with a few calculations performed in the $NPT$ ensemble, rather then the micro-canonical ensemble. Both of these ensembles require a thermostat to regulate the temperature throughout the simulation. Though there are several methods developed for thermostats, I have primarily chosen the Nosé-Hoover thermostat and Langevin thermostat due to the rigorous demonstrations in reproducing the $NVT$ and $NPT$ ensembles, respectively.

#### 3.2.2.1 Nosé-Hoover Thermostat

The Nosé-Hoover thermostat was originally developed by Shuichi Nosé in 1984 (Nosé, 1984a) and further improved by William Graham Hoover in 1985 (Hoover, 1985). It is commonly used for maintaining constant temperature in the canonical ensemble $NVT$ by means of exchanging energy with an external heat bath. By fixing the number of particles $N$, the volume $V$, and the temperature $T$, the three quantities do not fluctuate and the system temperature is connected to the average kinetic energy via:

$$\langle E_{\text{kin}} \rangle = \frac{3}{2} N k_B T \tag{3.30}$$

with instantaneous kinetic energy (from particle velocities) fluctuating in time. In the ap-

proach of Nosé, a Hamiltonian with an extra degree of freedom is introduced for the heat bath, $s$, allowing the total energy of the physical system to fluctuate with an associated potential energy $(f+1)k_BT_{eq}$, where $f$ is the number of degrees of freedom in the physical system and $T_{eq}$ is the externally set temperature value. The interaction between the physical system and $s$ is expressed by the scaling of the particle velocities $\mathbf{v}_i = s\mathbf{r}_i$ and $\mathbf{v}_i$ is the real velocity of particle $i$ and can be interpreted as an exchange of heat between the physical and external (heat bath) system. The Hamiltonian of the extended system takes the form:

$$H_{\text{Nosé}} = \sum_i \frac{\mathbf{p}_i^2}{2m_i s^2} + \Phi(\mathbf{r}) + \frac{p_s^2}{2Q} + f k_B T_{eq} \ln(s) \tag{3.31}$$

where $p_s$ is a conjugate momentum and $Q$ is an imaginary mass relating $p_s$ and $s$ by $\dot{s} = p_s/Q$ with dimensions of energy $\cdot$ (time)$^2$ and determines the time scale of the temperature fluctuations. This defines the potential and kinetic energy of the heat bath, and the particle momentum is now scaled by $\mathbf{p}_i = m_i \mathbf{v}_i s$.

To prove that configurations in the canonical ensemble at temperature $T_{eq}$ is produced, consider the partition function of this ensemble:

$$Z = \frac{1}{N!} \int dp_s \int ds \int d\mathbf{p} \int d\mathbf{r} \delta\Big( \sum_i \frac{\mathbf{p}_i^2}{2m_i s^2} + \Phi(\mathbf{r}) + \frac{p_s^2}{2Q} + f k_B T_{eq} \ln(s) - E \Big) \tag{3.32}$$

with $\delta$ denoting the Dirac delta function. By choosing $f = 3N + 1$, the partition function of the external system is equivalent to the physical system in the canonical ensemble except for a constant factor:

$$Z = C \int \exp\Big[ - H(\mathbf{p}, \mathbf{r}) / k_B T_{eq} \Big] d\mathbf{p} d\mathbf{r} \tag{3.33}$$

In the formulation above, it is difficult to implement Nosé's form to MD simulations due to the time-scaling of the momentum $p_s$. Hoover reformulated Nosé's Hamiltonian by

introducing a thermodynamic friction coefficient, $\xi$, and replacing the momentum of the heat bath by $\xi \equiv p_s/Q$, redefining $p_i \equiv m_i dr_i/dt$, and replacing Nosé's $(f+1)$ by $f$, leading to :

$$H = \sum_i \frac{\mathbf{p}_i^2}{2m_i s^2} + \Phi(\mathbf{r}) + \frac{\xi^2 Q}{2} + 3Nk_B T_{eq} \ln(s) \tag{3.34}$$

The time evolution of equation 3.34 can be obtained and now takes the forms:

$$\frac{dr_i}{dt} = \frac{p_i}{m_i} = v_i \tag{3.35}$$

$$\frac{dp_i}{dt} = F(r_i) - \xi p_i \equiv \frac{dv}{dt} = -\frac{\partial \Phi(\mathbf{r})}{\partial r_i} - \xi m_i v_i \tag{3.36}$$

$$\frac{d\xi}{dt} = \frac{\sum p_i^2/m - 3Nk_B T_{eq}}{Q} = \frac{\sum m_i v_i^2 - 3Nk_B T_{eq}}{Q} \tag{3.37}$$

$$\frac{d\ln(s)}{dt} = \xi \tag{3.38}$$

and closely resemble Newton's equations of motion with the additional thermodynamic friction coefficient included. The friction term is proportional to velocity (equation 3.38) and is determined from the requirement that the total kinetic energy (temperature) is constant:

$$\frac{dE_{\text{kin}}}{dt} = 0 \tag{3.39}$$

or

$$\sum \frac{p_i}{m_i} \frac{dp_i}{dt} = 0 \tag{3.40}$$

leading to

$$\xi = -\sum \frac{p_i}{m_i} \frac{\partial \Phi(r)}{\partial r_i} \Big/ \sum \frac{p_i^2}{m_i} \tag{3.41}$$

which recovers the canonical distribution by this method of "velocity scaling" (Hoover, 1985). This is advantageous because the thermodynamic friction coefficient does not vary with time like in Nosé's formulation when $\langle E_{\text{kin}} \rangle = \frac{3}{2} N k_B T$.

In VASP, the choice of the imaginary mass, $Q$, bears importance in the Nosé-Hoover thermostat and controls the frequency of the temperature oscillations. The chosen value in this thesis corresponds to a period of 40 time steps, set by the flag "SMASS = 0", which approximately shows the same frequencies as a typical "phonon"-frequency for the system.

#### 3.2.2.2 Parrinello-Rahman Barostat and Langevin Thermostat

In an $NPT$ simulation, the pressure remains constant due to the volume of the cell varying over time. The volume fluctuations are controlled using a barostat in addition to a thermostat controlling temperature fluctuations. The barostat in all $NPT$ simulations in this work follow the Parrinello-Rahman barostat algorithm (Parrinello and Rahman, 1980, 1981) which incorporates a time-dependent metric tensor, allowing the volume and shape of the MD cell to vary with time.

The Parrinello-Rahman formalism allows the cell to have an arbitrary shape and volume described by three lattice vectors $\vec{a}$, $\vec{b}$, $\vec{c}$ that span the edges of the MD cell. These lattice vectors can also be described by a 3 x 3 matrix $\vec{h}$ with a volume $\Omega$:

$$\Omega = ||\vec{h}|| = \vec{a} \cdot \vec{b} \times \vec{c} \tag{3.42}$$

The position of the particle $r_i$ can be written in terms of $\vec{h}$ and vector $\vec{s}$ with components $\xi_i$, $\eta_i$, $\zeta_i$:

$$r_i = \vec{h}\vec{s}_i = \xi_i\vec{a} + \eta_i\vec{b} + \zeta_i\vec{c} \tag{3.43}$$

where $0 \leq \xi_i, \eta_i, \zeta_i \leq 1$ and $i = 1, ..., N$. The square distance of the particles $i$ and $j$ is:

$$r_{ij}^2 = (\vec{s}_i - \vec{s}_j)^\intercal \vec{G}(\vec{s}_i - \vec{s}_j) \tag{3.44}$$

where the metric tensor, $\vec{G} = \vec{h}^\intercal\vec{h}$. The size and shape of the cell varies by a set of $3N$ dynamical variables that describe the positions of all particles $N$ in addition to the 9 components of $\vec{h}$, leading to $3N + 9$ variables. The Lagrangian takes the form:

$$\mathcal{L} = \frac{1}{2}\sum_i m_i \dot{\vec{s}}_i^\intercal \vec{G}\dot{\vec{s}}_i - \sum_{i=N}^{N}\sum_{j>i}^{N}\phi(r_{ij}) + \frac{1}{2}W\dot{\vec{h}}^\intercal\dot{\vec{h}} - p\Omega \tag{3.45}$$

where $p$ is the hydrostatic pressure imposed on the system, the variable $W$ has dimensions of mass, and the term $\dot{\vec{h}}^\intercal\dot{\vec{h}}$ can be physically understood as the rate of volume change of the system. Because the system is not subject to time-dependent external forces, the corresponding Hamiltonian can be constructed as:

$$H = \sum_i \frac{1}{2}m_i v_i^2 + \sum_{i=N}^{N}\sum_{j>i}^{N}\phi(r_{ij}) + \frac{1}{2}W\dot{\vec{h}}^\intercal\dot{\vec{h}} - p\Omega \tag{3.46}$$

At equilibrium, the temperature $T = 9/2k_BT$ and is contributed by $W$ and $3N/2k_BT$ from other kinetic terms, resulting in the constant of motion being equal to the enthalpy such that

$$H = E + p\Omega \tag{3.47}$$

where $E = \sum_i \frac{1}{2}m_i v_i^2 + \sum_{i=N}^{N}\sum_{j>i}^{N}\phi(r_{ij})$ and the Lagrangian in equation 3.45 is in an $NPH$ (constant enthalpy) ensemble.

Here, $W$ determines the relaxation time for recovery between the external pressure and internal stress, and the choice of $W$ varies depending on the system and is set by the flag "PMASS". The value of $W$ is chosen to be

$$\frac{1}{W} = \frac{4\pi^2\beta}{2\tau_p^2 L} \tag{3.48}$$

where $\beta$ is the compressibility, $L$ is the cell dimension, and $\tau_p$ is a time constant. We can combine this with the suggestion of Andersen (Andersen, 1980) where $W$ is on the same order of magnitude as the time $L/c$, where $c$ is the bulk sound velocity and

$$\tau_p = L/c \tag{3.49}$$

If we ignore the difference between isothermal and adiabatic compressibility, we have

$$c^2 = \frac{1}{\beta\rho} \tag{3.50}$$

where $\rho$ is the mass density and $\rho = M/L^3$, with $M$ being equal to the mass of the cell. Combining all of the equations results in our determination of $W$:

$$W = \frac{3M}{4\pi^2} \tag{3.51}$$

The Parrinello-Rahman algorithm leads to an $NPH$ ensemble, and a thermostat must be added to recover the $NPT$ ensemble. In VASP, the thermostat coupled to the Parrinello-Rahman algorithm is a Langevin thermostat (Allen and Tildesley, 2017; Hoover et al., 1982; Evans, 1983), which involves temperature control by introducing a friction term. The Langvein thermostat maintains the temperature by adding the term to Newton's equations of motion:

$$\dot{r}_i = p_i/m_i \tag{3.52}$$

$$\dot{p}_i = F_i - \gamma_i p_i + f_i \tag{3.53}$$

where $F_i$ is the force acting on the atom $i$ by means of an interaction potential, $\gamma_i$ is the friction coefficient, and $f_i$ is a random force from particle collisions by the damping of particles caused by friction. The random force is chosen from a Gaussian distribution with a variance equal to:

$$\sigma_i^2 = 2m_i\gamma_i k_B T/\Delta t \tag{3.54}$$

where $\Delta t$ is the MD time step.

By coupling the Parrinello-Rahman algorithm with the Langevin thermostat, we generate an $NPT$ ensemble in which the pressure and temperature are held constant while undergoing volume fluctuations. A consequence of the volume fluctuations is the possibility of cell shape fluctuations or shearing, which is particularly noticeable in liquid systems. This problem can be mitigated by defining geometric parameters that constrain the volume and/or shape of the simulation cell (specified in the file "ICONST" in VASP). By utilizing these constraints, we can fix the lattice angles and allow a cubic cell to have variable volume but fixed shape, for example, which can be extremely helpful for two-phase simulation setups and calculations (more in section 3.8).

## 3.3 Averages, Uncertainty, and Error Analysis

MD simulations typically produce finite time data sets that are correlated, where each point in the simulation depends on the result from the previous time step. In order to investigate stationary states, such as temperature and pressure, the first step is to calculate time averages. However, the time averages are computed over finite times and are fluctuating quantities, meaning another simulation of the same system may give a different value for the

same quantity. Comparing the two simulations should give the same average values within uncertainty; Therefore, estimating the variance of finite time averages is essential.

Before calculating averages and uncertainties, we first must determine when equilibrium occurs and discard the transient portion of the simulation, which typically reaches equilibrium within 1 - 2 ps as shown in figure 3.4. Once discarded, we can calculate the averages and uncertainties through the blocking method (Flyvbjerg and Petersen, 1989).

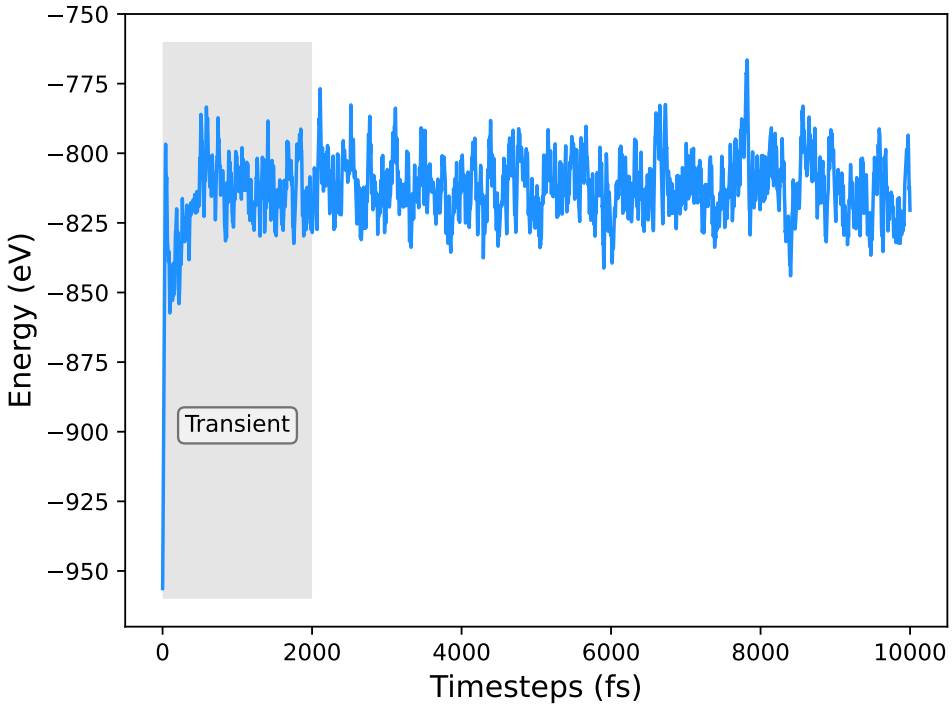


**Figure 3.4:** Internal energy $NVT$ time series data of $MgSiO_3$ at 6000 K, 1137.89 Å$^3$, and 58.6 GPa. The shaded area is the transient portion of the simulation that is discarded prior to calculating averages and uncertainties.

### 3.3.1 The Blocking Method

Although the blocking method was not invented by Flyvbjerg and Petersen, they proposed an efficient algorithm that is now widely used. The blocking method involves a renormalization group technique that is applied in the one-dimensional, discrete space of simulation time (Flyvbjerg and Petersen, 1989). We begin by estimating the expectation value of some fluctuation quantity by its time-average

$$m \equiv \bar{x} = \frac{1}{n}\sum_{i=1}^{n} x_i \tag{3.55}$$

where $n$ is the total number of time steps and $x_i$ is the value of the fluctuating quantity at time step $i$. An estimator for the variance of $m$ is

$$\sigma^2(m) = \langle m^2 \rangle - \langle m \rangle^2 \tag{3.56}$$

Inserting equation 3.55 into equation 3.56

$$\sigma^2(m) = \frac{1}{n^2}\sum_{i,j=1}^{n} \gamma_{i,j} = \frac{1}{n}\left[\gamma_0 + 2\sum_{i=1}^{n-1}\left(1 - \frac{t}{n}\right)\gamma_i\right] \tag{3.57}$$

where the correlated function $\gamma_{i,j} \equiv \langle x_i x_j \rangle - \langle x_i \rangle \langle x_j \rangle$ is introduced, and the expression makes use of it invariance under time translations to define $\gamma_i \equiv \gamma_{i,j}$ and $t = |i - j|$.

While the mean is straightforward to determine, computing the uncertainty, $\sigma^2$, takes some consideration. The name "blocking" in the blocking method suggests the approach taken here, which involves repeated blocking of data. First, the data set $x_1, ..., x_n$ is transformed into a new data set $x'_1, ..., x'_n$ that is half as large:

$$x'_i = \frac{1}{2}(x_{2i-1} + x_{2i}) \tag{3.58}$$

$$n' = \frac{1}{2}n \tag{3.59}$$

and $m'$ is defined as $\bar{x}'$, the average of the $n'$ "new" data set and $m' = m$. The terms $\gamma'_{i,j}$ and $\gamma'_i$ must also be defined, but from primed variable $x'_i$. It can be shown that

$$\gamma'_t = \left\{ \begin{array}{ll} \frac{1}{2}\gamma_0 + \frac{1}{2}\gamma_1, & \text{for } t = 0 \\ \frac{1}{4}\gamma_{2t-1} + \frac{1}{2}\gamma_{2t} + \frac{1}{4}\gamma_{2t+1}, & \text{for } t > 0 \end{array} \right\} \tag{3.60}$$

and

$$\sigma^2(m') = \frac{1}{n'^2}\sum_{i,j=1}^{n'} \gamma'_{i,j} = \sigma^2(m) \tag{3.61}$$

showing that $m$ and $\sigma^2(m)$ are invariant under the blocking method transformation and no information is lost. The advantage of the blocking method is revealed: the value of $\sigma^2(m)$ is unraveled gradually from $\gamma_t$ by repeating blocking transformations, and we know from equation 3.57 that

$$\sigma^2(m) > \frac{\gamma_0}{n} \tag{3.62}$$

Every time a blocking transformation is applied, $\gamma_0/n$ increases unless $\gamma_1 = 0$, making $\gamma_0/n$ invariant. Utilizing and manipulating a biased estimator:

$$\langle c_t \rangle = \gamma_t - \sigma^2(m) \tag{3.63}$$

can eliminate $\gamma_0$ altogether from the calculation, resulting in

$$\sigma^2(m) > \left\langle \frac{c_0}{n-1} \right\rangle \tag{3.64}$$

where $c_0$ is known from:

$$c_t = \frac{1}{n-t}\sum_{k=1}^{n-1}(x_k - \bar{x})(x_{k+1} - \bar{x}) \tag{3.65}$$

Knowing this, one can proceed by starting with the data set $x_1, ..., x_n$, computing $c_0/(n-1)$ and using it as an estimate for $\langle c_0/(n-1)\rangle$. Then, the blocking transformation is applied to the data set and $c_0'/(n'-1)$ is computed as an estimate for $\langle c_0'/(n'-1)\rangle$. We repeat the process until $n' = 2$, and the sequence of values from $c_0/(n-1)$ will increase until a fixed point is reached and it remains constant within fluctuations. The constant value is the estimate for $\sigma^2(m)$

We can estimate the standard deviation on the estimate for $c_0'/(n'-1)$ for $\sigma^2(m)$ at the fixed point, which is $(\sqrt{2/(n-1}c_0'/(n'-1)$:

$$\sigma^2(m) \approx \pm\sqrt{\frac{2}{n'-1}}\frac{c_0'}{n'-1} \tag{3.66}$$

$$\sigma(m) \approx \sqrt{\frac{c_0'}{n'-1}}\left(1 \pm \frac{1}{\sqrt{2(n'-1)}}\right) \tag{3.67}$$

Knowing the error determines whether the fixed point has been reached or not. If the fixed point isn't reached before $n' = 2$, it is signaled by $c_0/(n-1)$ not becoming constant, in which the largest value for $c_0/(n-1)$ is then a lower bound on $\sigma^2(m)$.

This method is the standard approach for the work in this thesis for calculating time average quantities and their uncertainties such as internal energy, pressure, temperature, and enthalpy.

### 3.3.2 Error Propagation

The average and uncertainty quantities can now be utilized for computing other properties of interest, in which error propagation must be taken into consideration. The approach taken here is (Bevington and Robinson, 2003):

$$\sigma_x^2 \approx \sigma_u^2 \left(\frac{\partial x}{\partial u}\right)^2 + \sigma_v^2 \left(\frac{\partial x}{\partial v}\right)^2 + ... \tag{3.68}$$

where $u$ and $v$ are variables of the function of interest, and similar terms for additional variables. Error propagation for simple sums and differences is given by a relative uncertainty:

$$\frac{\sigma_x}{x} = \frac{\sigma_u}{x} = \frac{\sigma_u}{u \pm a} \tag{3.69}$$

where the dependent variable $x$ is related to a measured quantity $u$ by the relation $x = u \pm a$.

Error propagation proves to be extremely important when making use of averaged quantities and their uncertainty to further compute other properties of the system such as the enthalpy of the system, where $H = U + PV$. The average and uncertainty of the internal energy and pressure must be considered when computing similar quantities for enthalpy. Thus, proper error propagation is always considered in this thesis.

## 3.4 Thermodynamic Properties

### 3.4.1 Heat Capacity

Many thermodynamic quantities can be related to the magnitude of the fluctuations in time variable quantities. For example, the magnitude of fluctuations in the internal energy in the $NVT$ ensemble are related to the isochoric heat capacity. Start by considering the partition function

$$Z = \sum_i e^{-E_i \beta} \tag{3.70}$$

where $i$ is the index for the microstates of the system, $\beta = 1/k_B T$ where $k_B$ is the Boltzmann constant and $T$ is the temperature, and $E_i$ is the total energy of the system in the respective microstate. The expectation value of the internal energy

$$\langle E \rangle = \frac{\sum_i E_i e^{-E_i \beta}}{Z} = -\frac{\partial \ln Z}{\partial \beta} \tag{3.71}$$

which represents the sum of the microstate energies weighted by their probabilities. We also have

$$\langle E^2 \rangle = \frac{\sum_i E_i^2 e^{-E_i \beta}}{Z} \tag{3.72}$$

and temperature derivative of equation 3.71 is:

$$\begin{aligned} C_v = \frac{\partial \langle E \rangle}{\partial T} &= \frac{1}{Z} \sum_i \frac{E_i^2}{k_B T^2} e^{-E_i \beta} + \left( \sum_i E_i e^{-E_i \beta} \right) \left( -\frac{1}{Z^2} \frac{\partial Z}{\partial \beta} \right) \\ &= \frac{1}{k_B T^2} \langle E^2 \rangle - \langle E \rangle \frac{\partial \ln Z}{\partial \beta} \\ &= \frac{1}{k_B T^2} (\langle E^2 \rangle - \langle E \rangle^2) \end{aligned} \tag{3.73}$$

where $C_v$ is the isochoric heat capacity. While this method is convenient, the uncertainties tend to be larger than those of the energy itself, requiring proportionately longer simulations to obtain accurate values.

### 3.4.2 Bulk Modulus

The isothermal bulk modulus

$$K_T = -V \frac{dP}{dV} \tag{3.74}$$

is related to the variance of the volume $V$ in the $NPT$ ensemble

$$\langle \Delta V^2 \rangle = (\langle V^2 \rangle - \langle V \rangle^2) \tag{3.75}$$

The derivation is similar to that for the heat capacity above, and we quote the final result (Allen and Tildesley, 2017):

$$K_T = \frac{\langle V \rangle k_B T}{\langle V^2 \rangle - \langle V \rangle^2} \tag{3.76}$$

As for the heat capacity, the bulk modulus derived from volume fluctuations can be compared, for example, with the value computed from the definition (Eq. 3.74) and the results of simulations at two different pressure via finite difference.

### 3.4.3 Grüneisen Parameter

The Grüneisen parameter

$$\gamma \equiv V \left( \frac{\partial P}{\partial E} \right)_V = \frac{V \alpha K_T}{C_v} = \frac{V \alpha K_S}{C_P} = -\left( \frac{\partial \ln T}{\partial \ln V} \right)_S \tag{3.77}$$

is dimensionless, of order unity for many materials, and useful in many geophysical contexts, including the understanding of the adiabatic temperature gradient in planetary interiors: $V$ is the volume, $C_P$ and $C_v$ are the heat capacities at constant pressure and volume, respectively $E$ is internal energy, $S$ is entropy, $\alpha$ is the isothermal expansion coefficient, $K_T$ and $K_S$ are the isothermal and adiabatic bulk modulus, respectively. We can determine the value of $\gamma$ from fluctuations, using formulas already presented, and from cross-fluctuations of pressure and energy, which yield the product $\alpha K_T$ (Allen and Tildesley, 2017).

The Grüneisen parameter can also be related to the following quantities

$$\gamma_i = -\frac{V}{\omega_i} \frac{\partial \omega_i}{\partial V} \tag{3.78}$$

where $\omega_i$ is the frequency of vibrational mode $i$, and the negative sign appears in the definition because vibrational frequencies typically increase on compression. For example, in the case of the Einstein model, in which we approximate the vibrational spectrum by a single

characteristic frequency $\omega_E$, we have $\gamma = \gamma_E$.

## 3.5 Dynamic Properties

### 3.5.1 Mean Squared Displacement

Dynamical properties such as diffusion are of interest for geophysical and planetary evolution processes. The diffusion coefficient can be extracted from an MD simulation through the mean squared displacement (MSD) of the atoms:

$$\mathrm{MSD}(\tau) = \left\langle |\vec{r} - \vec{r}_0|^2 \right\rangle = \frac{1}{N} \sum_{i=1}^{N} |(\vec{r}_i(t+\tau) - \vec{r}_i(t))|^2 \tag{3.79}$$

where $\vec{r}$ is the position of the $i^{th}$ atom and $N$ is the total number of atoms. The MSD represents the average squared distance between a particle's position and its new position after a time-lag $\tau$. At small times, the MSD shows a ballistic regime and a diffusive regime at longer times. Summing over all time origins $t$ significantly improves the statistics of the MSD. We can relate the gradient of the MSD to the self-diffusion coefficient, $D_\alpha$:

$$D = \lim_{t \Rightarrow \infty} \frac{\mathrm{MSD}(\tau)}{6t} \tag{3.80}$$

In practice, we fit a straight line to the function $MSD(\tau)$ beyond the ballistic regime, and relate the slope fo $D$.

### 3.5.2 Velocity Auto-correlation Function

The velocity auto-correlation function (VACF) measures the average correlation between the particle velocity at different times. The function is normalized

$$\Phi_i(\tau) = \frac{\langle \vec{v_i}(t+\tau) \cdot \vec{v_i}(t) \rangle}{\langle \vec{v_i}(t) \cdot \vec{v_i}(t) \rangle} \tag{3.81}$$

where $\vec{v}$ is the velocity of particle $i$ at time-lag $\tau$ compared to a time origin $t$, and the angle brackets represent the average over time origins. The denominator represents the mean-squared velocity, which normalizes the VACF to 1 when $t = 0$.

The diffusion coefficient can also be determined by taking the integral of the VACF:

$$D = \frac{1}{3} \int_{t=0}^{t=\infty} \left\langle \vec{v_i}(\tau) \cdot \vec{v_i}(0) \right\rangle d\tau \tag{3.82}$$

Like the MSD, the VACF can provide information for characterizing the material properties. A VACF typical of a solid shows oscillations that correspond to vibrational periods and amplitudes that decay with time due to anharmonicity. The VACF of a liquid system tends to decay more rapidly in time as compared with that of a solid due to greater anharmonicity and the presence of diffusive modes. Because the uncertainty in the value of the VACF can become large for long times, one typically convolves the VACF with a Gaussian filter before computing integrals such as Eq. 3.82.

The VACF also yields the vibrational density of states

$$F(\nu) = \int_0^\infty \Phi(t) \cos(2\pi\nu t) dt \tag{3.83}$$

where $\nu$ is the vibrational frequency. The vibrational density of states for liquids and solids look very similar, with differences arising in sharp peaks, or more structure, for solid phases, and in the value at zero frequency. In the liquid, the vibrational density of states show a finite value at zero frequency, which arises from diffusive modes that are not present in the solid phase. The self-diffusion coefficient can be related to the liquid phase's zero frequency value:

$$D = \frac{k_B T}{m} F(0) \tag{3.84}$$

which also provides another method for calculating the self-diffusion coefficient.

### 3.5.3 Ionic Conductivity

The ionic conductivity is a property that can be determined from the dynamics of an MD simulation. The ionic conductivity can be calculated from the electric current auto-correlation

$$J(t) = \sum_{i,j} z_i z_j \langle \vec{v}_i(t + t_0) \cdot \vec{v}_j(t_0) \rangle \tag{3.85}$$

where $z$ is the ionic charge of atom $i$ or $j$. For example, the ionic charges of FeOOH would be +3, -2, and +1 for Fe, O, and H, respectively. From the electric current auto-correlation function, the ionic part of the electrical conductivity is computed as the integral:

$$\sigma_{ion} = \frac{q^2}{3k_B T\Omega} \int J(t)dt \tag{3.86}$$

where $q$ and $\Omega$ represent the elementary charge and volume of the system.

Because it is widely used in the literature, we also record an approximate method for estimating the ionic conductivity, which neglects correlated motion of the ions: the Nernst-Einstein relation

$$\sigma = \frac{Dxq^2}{k_B T H_R} \tag{3.87}$$

where $x$ is the number of electrical carriers per volume, $q$ is the elementary charge, and $H_R$ is the Haven ratio which empirically accounts for correlated motion and can be shown to approach unity in the limit of small concentrations.

### 3.5.4 Radial Distribution Function

The radial distribution function (RDF) $g(r)$ gives the probability of finding a pair of atoms a distance $r$ apart, relative to that of a random arrangement at the same density. The function gives us a means of characterizing the structure of a liquid and demonstrates the presence

of short-range order, combined with long-range disorder. The RDF for atoms types $\alpha$ and $\beta$ is defined

$$g_{\alpha\beta}(r) = \frac{V}{N_\alpha N_\beta} \sum_{i=1}^{N_\alpha} \sum_{k \neq i}^{N_\beta} \left\langle \delta(r - |\vec{r}_k - \vec{r}_i|) \right\rangle \tag{3.88}$$

where $V$ is the volume, $N_i$ is the total number of atoms of type $i$, and $\delta$ is the Dirac delta function. The function is typically computed via binning: replacing the delta function with a bin of finite width. An alternative method has recently been described which shows reduced variance, and which, moreover, is independent of arbitrary choices such as the bin size (Coles et al., 2021).

First, a general expression for combining estimators is proposed

$$E_\lambda(x) = (1 - \lambda)E_0(x) + \lambda E_1(x) = E_0(x) + \lambda\Delta(x) \tag{3.89}$$

where $E_0(x)$ and $E_1(x)$ are estimators of the same property that depend on some parameter $x$ (i.e., distance or position), $\Delta(x) = E_1(x) - E_0(x)$, and $E_\lambda$ denotes another valid estimator of the same property, where the expectation value of $E_\lambda(x)$ is the same as that of $E_0(x)$ and $E_1(x)$. However,the variance of $E_\lambda$ is a quadratic function of $\lambda$, where $\mathrm{var}(E_\lambda(x)) = \langle [E_\lambda(x) - \langle E_\lambda(x)\rangle]^2\rangle$. Therefore, one can find for each $x$ a combination that minimizes the variance:

$$\lambda^*(x) = -\frac{\mathrm{cov}(E_0(x), \Delta(x))}{\mathrm{var}(\Delta(x))} = 1 - \frac{\mathrm{cov}(E_1(x), \Delta(x))}{\mathrm{var}(\Delta(x))} \tag{3.90}$$

which involves the covariances $\mathrm{cov}(A, B) = \langle (A - \langle A\rangle)(B - \langle B\rangle)\rangle$ and provides an optimal estimator $E^*_\lambda(x)$ for each $x$. In practice, the expectation values $\langle E_n(x)\rangle$ and covariances entering equation 3.90 are determined from two given estimators, which then leads to the corresponding optimal estimator $E^*_\lambda(x)$ from equation 3.89.

The two estimators chosen to calculate the RDF from the force-based method are:

$$\hat{g}_{\lambda=0}(r) = 1 + \frac{V}{N^2}\frac{\beta}{4\pi}\sum_i\sum_{i\neq j}\frac{\vec{f}_j - \vec{f}_i}{2}\cdot\frac{\vec{r}_{ij}}{r_{ij}^3}\mathrm{H}(r_{ij} - r) \tag{3.91}$$

$$\hat{g}_{\lambda=1}(r) = \frac{V}{N^2}\frac{\beta}{4\pi}\sum_i\sum_{i\neq j}\frac{\vec{f}_j - \vec{f}_i}{2}\cdot\frac{\vec{r}_{ij}}{r_{ij}^3}\mathrm{H}(r - r_{ij}) \tag{3.92}$$

where $\vec{f}_i$ and $\vec{f}_j$ are the forces acting on atoms $i$ and $j$, $r_{ij}$ is the displacement vector, and H is the Heaviside function. These expressions are derived by computing the density gradient in the canonical ensemble; the force arises from the operation of the gradient on the Boltzmann weight $\exp(-\beta U)$ (Rotenberg, 2020). The first expression integrates the density gradient from the exact limiting value $g \to 1$ as $r \to \infty$, whereas the second matches the exact value $g = 0$ at $r = 0$. This approach eliminates the need for binning due to the estimator's dependence on $r$ and all values of the RDF can be obtained with arbitrary resolution (Figure 3.5).

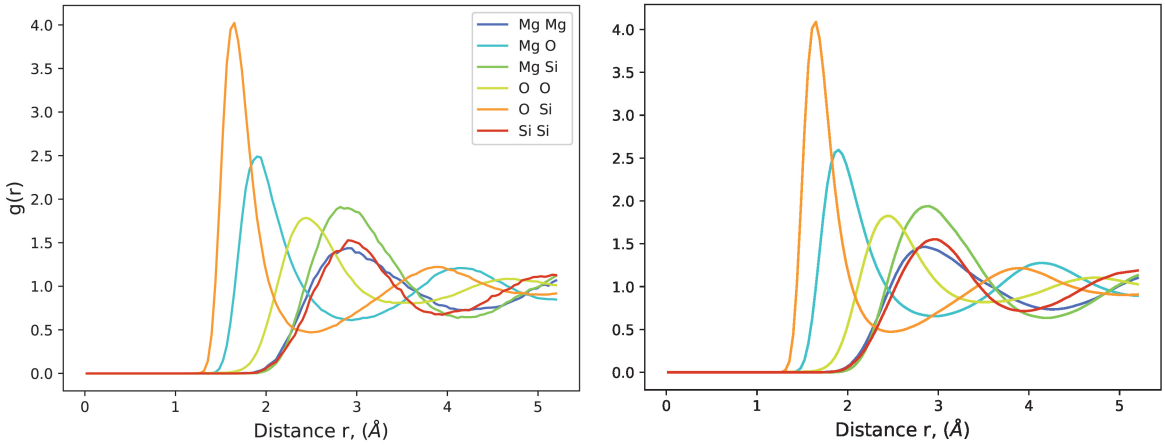


**Figure 3.5:** Radial distribution function comparing the binning method (left) versus the force estimator method (right) of $NVT$ $MgSiO_3$ at 6000 K, 1137.89 Å$^3$, and 58.6 GPa.

We also obtain from the RDF the coordination number

$$C_{\alpha\beta} = 4\pi\rho_\beta \int_0^{r_{\min}} r^2 g_{\alpha\beta}(r) dr \tag{3.93}$$

where $\rho_\beta$ is the number density of atom type $\beta$ and $r_{\min}$ is the distance to the first minimum in $g_{\alpha\beta}$. The coordination number provides insight on the number of atoms bonded to species of interest, for example, the Si-O coordination number in silicate liquids increases from 4 to 6 over the pressure regime of Earth's mantle, producing more efficiently packed configurations (Stixrude and Karki, 2005).

### 3.5.5 Bond Auto-correlation Function

In liquids, interatomic bonds constantly break and reform. This quantity gives us an estimate of typical bond lifetimes

$$B_x(t) = \left\langle \frac{b_{ij}(t_0) \cdot b_{ij}(t_0 + t)}{b_{ij}(t_0)^2} \right\rangle \tag{3.94}$$

where $b_{ij}(t) = 1$ if atoms $i$ and $j$ are bonded, that is are separated by a distance less than $r_{\min}$, and $b_{ij}(t) = 0$ otherwise.

The mean bond lifetime is then

$$\tau_x = \int_0^\infty B_x(t) dt'. \tag{3.95}$$

The subscript $x$ has to do with the details of how bonds are counted. At least two choices are possible. The continuous choice counts bonds until they break and then ignores them for all subsequent time, whereas the intermittent choice allows the bond to break and reform.

## 3.6 Entropy

### 3.6.1 Vibrational Entropy - The Two-Phase Thermodynamic (2PT) Method

Calculation of the entropy from *ab initio* MD simulations is a fundamentally difficult problem because, unlike energy or pressure, the entropy is not defined for any given snapshot of the trajectory, it can only be defined from the ensemble of configurations. The entropy is important, for example, for computing the Gibbs free energy, which determines phase equilibria

$$G = E + PV - TS \tag{3.96}$$

where all the quantities on the right hand side are readily available except for the entropy. The method for calculating the entropy directly in this thesis follows the work of Desjarlais (2013) and Wilson and Stixrude (2021) (Desjarlais, 2013; Wilson and Stixrude, 2021) and is known as the two-phase thermodynamic (2PT) method.

The 2PT method involves the decomposition of the vibrational density of states into solid- and gas-like portions

$$F_\alpha(\nu) = (1 - f_\alpha)F_\alpha^s(\nu) + f_\alpha F_\alpha^g(\nu) \tag{3.97}$$

where $\alpha$ refers to atom type and $F_\alpha^g$ and $F_\alpha^s$ are the gas-like and solid-like contributions that need to be determined, and the normalization is

$$\int_0^\infty 12F_\alpha(\nu)d\nu = 3 \tag{3.98}$$

satisfying the total density of states sum rule. The total entropy of the system

$$S(V,T) = S_{el}(V,T) + k_B \sum_{\alpha} \left( x_\alpha \int_0^\infty d\nu \left[ f_\alpha F_\alpha^g(\nu) W_\alpha^g + (1 - f\alpha) F_\alpha^s(\nu) W^s(\nu) \right] - x_\alpha \ln x_\alpha \right) \tag{3.99}$$

where the $W_\alpha^g$ and $W^s$ are the gas-like and solid-like kernels and $S_{el}$ is the electronic entropy. The solid-like kernel is the Bose-Einstein expression for a collection of harmonic oscillators (Born and Huang, 1996):

$$W^s(\nu) = 3 \left( \frac{h\nu/k_B T}{\exp(h\nu/k_B T) - 1} - \ln \left[ 1 - \exp(-h\nu/k_B T \right] \right) \tag{3.100}$$

and is independent of atom type. The gas-like kernel is given by the entropy of a hard-sphere fluid and is independent of frequency

$$W_\alpha^g = \frac{S_{IG\alpha}}{k_B} + \ln \left[ \frac{1 + \gamma_\alpha + \gamma_\alpha^2 - \gamma_\alpha^3}{(1 - \gamma_\alpha)^3} \right] + \frac{3\gamma_\alpha^2 - 4\gamma_\alpha}{(1 - \gamma_\alpha)^2} \tag{3.101}$$

where $\gamma_\alpha$ is the hard-sphere packing fraction, which is found numerically by solving:

$$\gamma_\alpha^{2/5} \Delta^{3/5} = \frac{2(1 - \gamma_\alpha)^3}{2 - \gamma_\alpha} \tag{3.102}$$

where $\Delta_\alpha$ is a parameter related to the self-diffusion coefficient:

$$\Delta_\alpha = \frac{8}{3} F_\alpha(0) \sqrt{\frac{\pi k_B T}{m_\alpha}} \bar{V}_\alpha^{-1/3} \left( \frac{6}{\pi} \right)^{2/3} \tag{3.103}$$

and $\bar{V}_\alpha$ is the partial molar volume of atom type $\alpha$. The ideal gas contribution of the entropy, $S_{IG\alpha}$ is:

$$\frac{S_{IG\alpha}}{k_B} = \frac{5}{2} + \ln \left( \frac{\bar{V}_\alpha}{\Lambda_\alpha^3 f_\alpha} \right) \tag{3.104}$$

and the de Broglie wavelength is $\Lambda_\alpha = h/\sqrt{2\pi m_\alpha k_B T}$.

We can express the VACF as an infinite MacLaurin series:

$$\Phi_\alpha(t) = \sum_{n=0}^{\infty} (-1)^n \frac{M_{2n}}{(2n)!} t^{2n} \tag{3.105}$$

with the coefficients given by the even moments of the vibrational density of states

$$M_k = \langle \nu^k \rangle = \frac{\int_0^\infty \nu^k F(\nu) d\nu}{\int_0^\infty F(\nu) d\nu} \tag{3.106}$$

Computing the moments in this way can be numerically unstable because of its sensitivity to the high-frequency, low-amplitude portion of the vibrational density of states. An alternative means of computation of the moments follows from the exact relation (Isbister and McQuarrie, 1972):

$$M_{2n} = \frac{\langle \vec{v}_i^{(n)}(t) \cdot \vec{v}_i^{(n)}(t) \rangle}{\frac{3k_B T}{m}} \tag{3.107}$$

where $\vec{v}^{(n)}$ is the $n^{th}$ time derivative of the velocity.

To further develope the gas-like portion of the vibrational density of state, introduce the memory function, which is defined by

$$\frac{d\Phi_\alpha}{dt} = -\int_0^t K_\alpha(\tau) \Phi_\alpha(t-\tau) d\tau \tag{3.108}$$

The memory function is known to be short-ranged: it decays much more rapidly in time than the VACF, and serves as a useful starting point for further approximation. The proposed functional form specifying the gas-like vibrational density of states is a Gaussian (Desjarlais, 2013):

$$K_\alpha^g(\tau) = A_\alpha \exp(-B_\alpha \tau^2) \tag{3.109}$$

with the Laplace transform:

$$\hat{K}_\alpha^g(s) = K_{0\alpha} w(-\eta) \tag{3.110}$$

where $K_{0\alpha} = A_\alpha \sqrt{\pi/4B_\alpha}$, $\eta = s/2\sqrt{B_\alpha}$, and $w$ is the Faddeeva function

$$w(z) = e^{-z^2} \mathrm{erfc}(-iz) \tag{3.111}$$

where $i$ is the imaginary unit.

The gas-like portion of the vibraitonal density of states is then

$$F_\alpha^g(\nu) = \frac{1}{2}\left[\frac{1}{\hat{K}_\alpha^g(i2\pi\nu) + i2\pi\nu} + \frac{1}{\hat{K}_\alpha^g(-i2\pi\nu) - i2\pi\nu}\right] \tag{3.112}$$

Combining all of the relations completes the definition of $F_\alpha^g$ by determining the values of $f_\alpha$, $A_\alpha$, and $B_\alpha$:

$$f_\alpha = \frac{F_\alpha(0)}{F_\alpha^g(0)} = \frac{A_\alpha F_\alpha(0)}{2}\sqrt{\frac{B_\alpha}{\pi}} \tag{3.113}$$

$$\frac{4B_\alpha}{A_\alpha} = 2 + \sqrt{\pi\left(1 + \frac{4B_\alpha F_\alpha^2(0)}{\gamma_\alpha^{4/5}\Delta_\alpha^{6/5}}\right)} \tag{3.114}$$

$$B_\alpha = \frac{f_\alpha(2M_2A_\alpha - M_4 - A_\alpha^2) + M_4 - M_2^2}{2f_\alpha(1-f_\alpha)A_\alpha} \tag{3.115}$$

Equation 3.113 ensures that the gas-like portion accounts for the DC limit of the VACF. Equation 3.114 arises from demanding the agreement of the low frequency portion of the vibrational density of states derived from the Gaussian and delta (simplest functional form) memory functions. Equation 3.115 guarantees that the first two even moments of the VACF are matched.

With the 2PT method, we can compute the total entropy of the system except for the electronic entropy $S_{el}$. The electronic entropy of the system is easily calculated from electronic structure of the system by summing over the bands:

$$S_{el} = \sum_{i}^{\text{bands}} f_i \ln f_i + (1 - f_i) \ln(1 - f_i) \tag{3.116}$$

and considers the occupation $f_i$ of band $i$. With this formulation, it is easily recognizable that an insulating system with a finite band gap will have zero electronic entropy due to the occupation of the bands being either 1 or 0. However, a conducting system with no band gap and partial occupation near the Fermi level will result in a non-zero electronic entropy.

## 3.7 Raman and Infrared Spectroscopy

From DFT, the phonon vibrational frequencies can be determined via density functional perturbation theory (DFPT). Phonon frequencies and eigenvectors are computed in the harmonic limit from the second-order force constant matrix $\Phi_{\alpha\beta}(jl, j'l')$, the elements of which are the change in force in the $\alpha$ Cartesian direction acting on atom $j$ in unit cell $l$, in response to the displacement of atom $j'$ in unit cell $l'$ in the $\beta$ direction. The phonon frequencies are the eigenvalues of the dynamical matrix at a given wavevector $\boldsymbol{q}$:

$$D^{jj'}_{\alpha\beta}(\mathbf{q}) = \frac{1}{\sqrt{m_j m_{j'}}} \sum_{l'} \Phi_{\alpha\beta}(jl, jl') \exp[i\mathbf{q} \cdot (\mathbf{r}(j', l') - \mathbf{r}(j, l))] \tag{3.117}$$

where $m_j$ are the atomic masses and $l$ and $l'$ are the unit cells of the two atoms.

The long-ranged Coulomb interactions lead to non-analytic corrections in the limit $\boldsymbol{q} \to 0$, that cause splitting of longitudinal optic (LO) and transverse optic (TO) modes (Pick et al., 1970; Gonze and Lee, 1997):

$$D^{jj'}_{\alpha\beta}(\mathbf{q}\to 0) = D^{jj'}_{\alpha\beta}(\mathbf{q}=\mathbf{0}) + \frac{1}{\sqrt{m_j m_{j'}}}\frac{4\pi}{\Omega_0}\frac{\left[\sum_\gamma q_\gamma Z^j_{\gamma\alpha}\right]\left[\sum_{\gamma'} q_{\gamma'} Z^{j'}_{\gamma'\beta}\right]}{\sum_{\alpha\beta} q_\alpha \varepsilon^\infty_{\alpha\beta} q_\beta} \tag{3.118}$$

where $\mathrm{Z}_{\alpha\beta}{}^{\mathrm{j}}$ is the Born effective tensor, $\varepsilon^\infty$ is the macroscopic dielectric tensor, and $\Omega_0$ is the volume of the cell.

Because DFPT does not compute the intensities, we utilize the open source python package Phonopy (Togo et al., 2023; Togo, 2023). The package uses an interface that includes VASP input files and require the converged unit-cell structure, calculation of force constants from DFPT, the Born effective tensor, and dielectric tensor. Phonopy efficiently produces all eigen-displacements around the Γ-point in the form of separate POSCAR files, in which the ground state energies of each eigen-displacement are computed to determine the Born effective tensor and dielectric of the respective eigen-displacement. The number of files produces is dependent on the number of atoms and the unit cell space group symmetry.

The Infrared (IR) intensities are computed from eigen-displacements around the Γ-point, where the atom's change in polarizability with respect to atomic displacement is captured by the Born effective-charge tensors (Giannozzi and Baroni, 1994):

$$I_{IR}(s) = \sum_\alpha \left| \sum_{j\beta} Z^j_{\alpha\beta} \frac{\mathbf{W}(s,j)}{\sqrt{m_j}} \right|^2 \tag{3.119}$$

where ***W(s,j)*** is the eigenvector of the dynamical matrix corresponding to mode s.

The Raman intensities are computed from the change in the polarizability tensor $\alpha$ along the mode eigenvectors in terms of the macroscopic high-frequency dielectric constant (Skelton et al., 2017), via a central finite-difference scheme:

$$I_{Raman} \propto \frac{\partial \alpha}{\partial Q(s)} \equiv \frac{\partial \varepsilon^\infty}{\partial Q(s)} \approx \frac{\Delta \varepsilon^\infty}{\Delta Q(s)} \tag{3.120}$$

$$I_{Raman,\alpha\beta}(s) = \frac{\Omega}{4\pi}\left[-\frac{1}{2}\frac{\varepsilon^\infty_{\alpha\beta}(-s)}{\Delta Q(s)} + \frac{1}{2}\frac{\varepsilon^\infty_{\alpha\beta}(+s)}{\Delta Q(s)}\right] \tag{3.121}$$

where $Q$ is the normal-mode coordinate at the $\Gamma$-point and is defined by $u(s,j) = Q(s)\mathbf{W}(s,j)/\sqrt{m_j}$, where $u(s,j)$ is the atomic displacement. The un-polarized Raman intensity takes the form:

$$I_{Raman} = 45\left[\frac{1}{3}(I_{xx}+I_{yy}+I_{zz}\right]^2 + \frac{7}{2}\left[(I_{xx}-I_{yy})^2+(I_{xx}-I_{zz})^2+(I_{yy}-I_{zz})^2+6(I_{xy}^2+I_{xz}^2+I_{yz}^2)\right]. \tag{3.122}$$

with subscripts representing the directions in Cartesian coordinates.

## 3.8 Electronic Spin Transition

Here, I will be discussing the electronic spin transition of Fe in the framework of crystal field theory where the geometry of the ligands plays a large role. It is important to note here that crystal field theory is typically used to discuss breaking of degenerate electron orbital states for molecular physics purposes. For simplicity, it is the model I will be using to discuss electronic spin transitions in this work.

In crystalline $\varepsilon$-FeOOH and pyrite-FeOOH, the $Fe^{3+}$ ion assumes an octahedral environment with 6 surrounding $O^{2-}$ ligands (Figure 3.6). The negatively charged ligands are aligned with the $3d_{z^2}$ and $3d_{x^2-y^2}$ orbitals ($e_g$ states) of the Fe atoms and thus an increased repulsion occurs relative to the other $d$-orbitals ($t_{2g}$ states), causing an energy separation or splitting, $\Delta_0$.

The distribution of the $3d$ electrons in $Fe^{3+}$ is controlled by two opposing tendencies (Burns, 1993): (1) The repulsion and exchange interactions between the electrons causes distribution over as many of the $3d$-orbitals as possible with parallel spins. Otherwise known as Hund's rule of spin multiplicity and the Pauli exclusion principle (Pauli, 1925a), where empty sub-shells will be preferentially filled and must each contain one electron of opposite spin before other orbitals in the same sub-shell are filled. (2) The Aufbau principle. Following the Aufbau principle, the electrons in $Fe^{3+}$ will fill the sub-shells of the lowest available

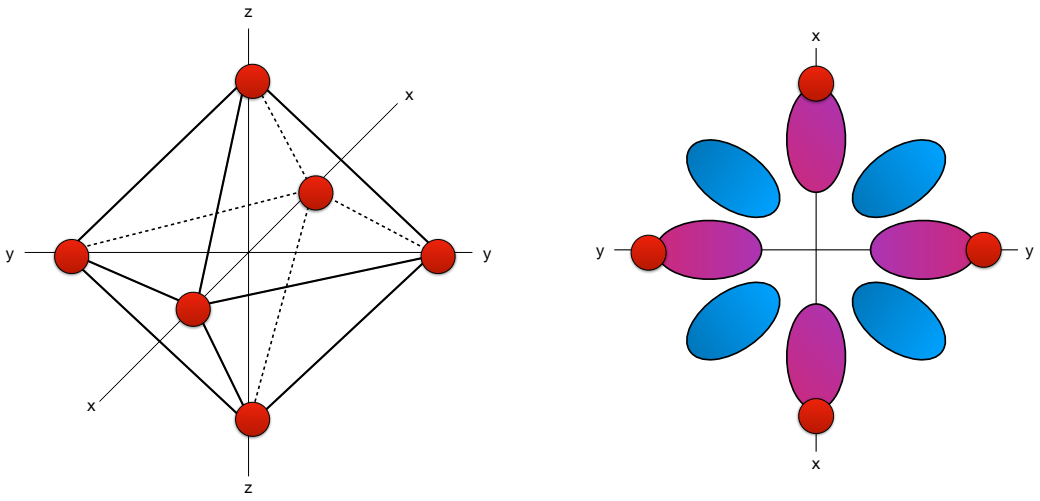


**Figure 3.6:** Orientation of ligands and $d$-orbitals of a $Fe^{3+}$ ion in an octahedral environment, modified from (Burns, 1993). Oxygen atoms (ligands) shown in red. (*Left*): Octahedral environment with respect to Cartesian coordinates. (*Right*) The x-y plane of an $Fe^{3+}$ ion in an octahedral crystal field. The $d_{xy}$-orbital is in blue and the $d_{x^2-y^2}$-orbital is shown in violet.

energy first and then subsequently filling the higher energy sub-shells. These two opposing tendencies lead to a high-spin and low-spin electronic configuration in $Fe^{3+}$ ions.

In the high-spin state of an $Fe^{3+}$ ion, all five valence electrons will singly occupy each $d$-orbital due to the energy separation $\Delta_0$ being low enough. As pressure increases, compression drives the physical distance between the ligands to decrease, resulting in a greater repulsion and a larger energy separation between the $e_g$ and $t_{2g}$ states. As a consequence, the electrons disobey Hund's rule and preferentially occupy and pair up in the $t_{2g}$ states first before occupying the $e_g$ states (Figure 3.7). This configuration is known as the low-spin state and is seen experimentally in the form of a volume collapse in many published studies.

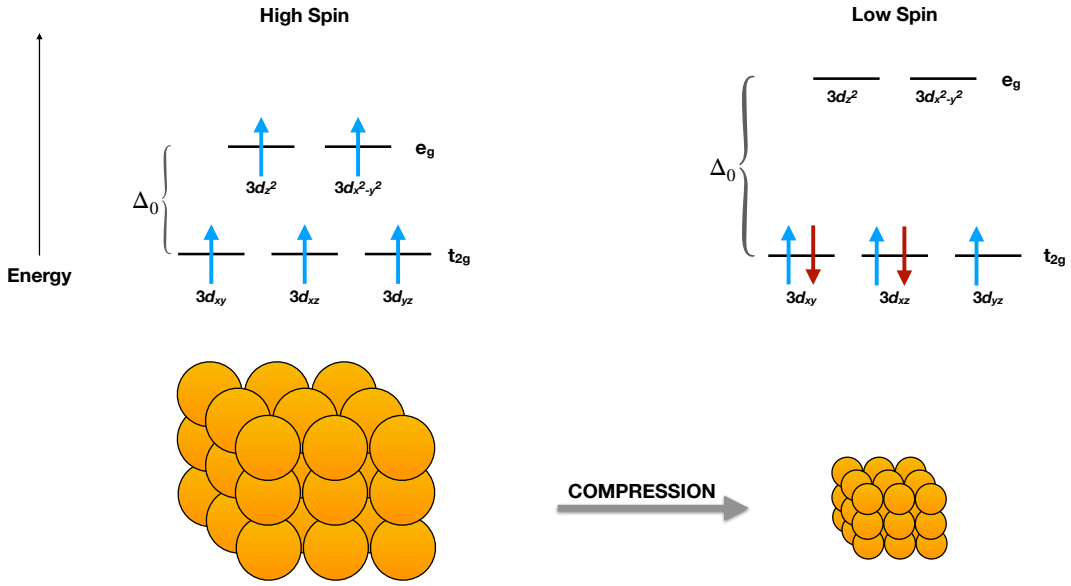


**Figure 3.7:** The high-spin and low-spin electronic configuration of an $Fe^{3+}$ ion driven by compression.

## 3.9 Two-Phase Systems

A large portion of the work in this thesis involves investigating the chemical reactions at the interface of the Earth's core and mantle. To do this, we set up a two-phase system where we juxtapose two homogeneous phases and allow them to react with one another. In this section, I will describe the set up of the simulations, quantify reaction that occurs in the simulation, and review the corresponding thermodynamics to construct a phase diagram.

### 3.9.1 Initial Conditions

The two-phase simulations are initiated as domains of pure core material and pure mantle material joined at planar interfaces. We choose to represent the core with an Fe-liquid and the mantle with a pure MgO-liquid phase or pure $MgSiO_3$-liquid phase. For simplicity, I will

choose MgO as the mantle phase to describe the interface set up.

We prepare the initial condition by first performing homogeneous simulations to ensure that the Fe-liquid and the MgO-liquid initially have the same pressure, temperature, and volume. In these homogeneous simulations, we first form a liquid phase by melting at 10,000 K for 5-10 ps before cooling to 6000 K and equilibrating for another 10 ps. We examined two different regimes for which we chose the number density such that the equilibrated pressure was 60 GPa at 6000 K. During the course of the two phase simulations the system responds by establishing a dynamic equilibrium in which the composition of the two coexisting phases is stationary.

### 3.9.2 Two-Phase Interfaces

We quantify the compositions of the two coexisting phases in two ways following the work of Xiao and Stixrude (2018): (1) A 1D density profile normal to the interface (Widom, 1982) and (2) A coarse grained density field (Willard and Chandler, 2010).

#### 3.9.2.1 Widom Hyperbolic Tangent Method

We define the one-dimensional density profile of an atom type (Mg, Fe, O) in the direction normal to the interface ($z$)

$$\rho(z) = \langle \rho(z,t) \rangle \tag{3.123}$$

where the angle brackets represent the time-average and

$$\rho(z,t) = \sum_i \delta(z - z_i(t)) \tag{3.124}$$

where $z_i(t)$ is the $i^{th}$ particle's position at time $t$ along the $z$ axis.

We find that the one-dimensional density profile follows the expected hyperbolic tangent form:

$$\rho(z) = \rho_2 + \frac{\rho_1 - \rho_2}{2} \sum_{j=1}^{2} (-1)^j \tanh \frac{(z - z_1) - \mathrm{nint}(z - z_1) + (-1)^j w}{\delta} \tag{3.125}$$

where $\rho_1$ is the number density of an atom type (Fe, Mg, or O) in the phase whose center of mass is located at scaled coordinate $z_1$, $w$ is the half-width of the phase, $\rho_2$ is the number density of that atom type in the other phase, $\delta$ is the width of the interface, the nint function accounts for periodic boundary conditions, and the sum accounts for the presence of two interfaces. An example of a fit of this form to our results is shown in Figure 3.8.

Determination of the density profile (Eq. 3.123, 3.124) requires binning and can lead to relatively poor statistics for feasible run duration. I have therefore also explored an alternative method for computing the density profile, which uses the interatomic forces. Recalling the force-based estimators from the RDF, we can apply a similar methodology to the 1D density profile (Coles et al., 2021). To compute the 1D density from the force field method, consider the force density:

$$\nabla \rho(\mathbf{r}) = \beta \left\langle \sum_i \delta(\mathbf{r} - \mathbf{r}_i) \mathbf{f}_i \right\rangle \tag{3.126}$$

where $\nabla$ is the gradient operator, $\mathbf{r}_i$ is the position of the particle $i$, $\delta$ is the Dirac delta function, $\beta = 1/k_B T$, and $\mathbf{f}_i$ is the force acting on atom $i$. The density can be obtained by integrating the force density from either side of the simulation cell, leading to the two estimators:

$$\Delta\rho_0(z) = \langle \Delta\hat{\rho}_{\lambda=0}(z) \rangle = \left\langle \frac{1}{S} \sum_i \mathrm{H}(z - z_i) \beta f_{z,i} \right\rangle \tag{3.127}$$

$$\Delta\rho_1(z) = \langle \Delta\hat{\rho}_{\lambda=1}(z) \rangle = \left\langle \frac{1}{S} \sum_i \mathrm{H}(z_i - z) \beta f_{z,i} \right\rangle \tag{3.128}$$

where H is the Heaviside function. The integration constant is determined from the average density $\rho_0$

$$\rho_\alpha(z) = \Delta\rho_\alpha(z) - \frac{\int \Delta\rho_\alpha(z)dz}{L} + \frac{N_\alpha}{V} \tag{3.129}$$

where $L$ is the length along the $z$ axis, $N_\alpha$ is the total number atom type $\alpha$, and $V$ is the volume of the system. Following the general expression for combining estimators from equations 3.89 and 3.90, we can obtain the optimal expression for the 1D density profile without the need for any binning (Figure 3.8).

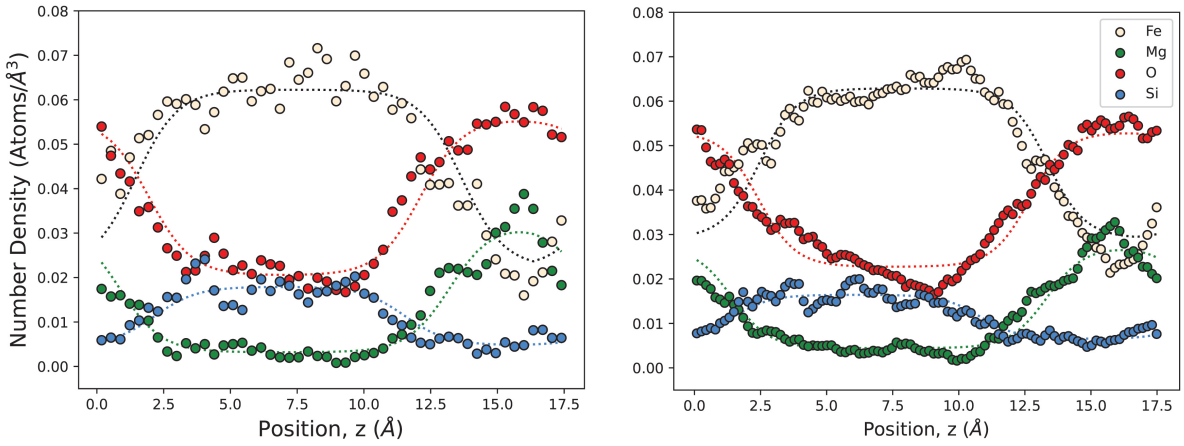


**Figure 3.8:** Comparison of number density calculation methods for discrete binning from equation 3.124 (*left*) versus the force field method from equation 3.89 (*right*) of Fe-$MgSiO_3$ at 5000 K, 57 GPa, and 1356.79 Å$^3$. The dotted lines are best fits determined by fitting equation 3.125.

Once the density of each atom types in each phase (Fe-rich or Fe-poor) has been determined, computing the respective concentrations in mol % and/or wt % is straightforward. For example, the mol % of MgO species in the Fe-rich or Fe-poor phase follows:

$$x_{MgO} = \frac{\frac{1}{2}(\rho_{Mg} + \rho_O)}{\frac{1}{2}(\rho_{Mg} + \rho_O) + \rho_{Fe}} \times 100\% \tag{3.130}$$

from which then the compositions of each phase can be determined.

#### 3.9.2.2 Willard and Chandler Method

In the second approach following Willard and Chandler (2010), we first define a coarse-grained density field by convolving atomic positions with a Gaussian:

$$\bar{\rho}(\vec{r},t) = \sum_i (2\pi\xi^2)^{-3/2} \exp\left[-\left(\vec{r}-\vec{r}_i\right)^2 / 2\xi^2\right], \tag{3.131}$$

where $\vec{r}_i$ is the position of atom $i$, the sum is over the Fe atoms, and $\xi$ is the coarse-graining length, which we take to be 2.4 Å. The interface, $\mathbf{s}$, is located at every time step such that:

$$\bar{\rho}(\mathbf{s},t) = c \tag{3.132}$$

where the density of the interface $c$ is set to approximately 1/2 the bulk density of the Fe atoms. The interfaces determined in this way are shown in Figure (show figure). The time-averaged interface is planar and represents the Gibbs dividing surface.

With this definition of the interface, we can now assign each atom to one of the two phases. The proximity of each atom to the interface is:

$$a_i(t) = \{[\mathbf{s} - \mathbf{r}_i(t)] \cdot \mathbf{n}(t)\}|_{\mathbf{s}(t)=\mathbf{s}_i^*(t)} \tag{3.133}$$

where $\mathbf{s}_i^*(t)$ is the point on $\mathbf{s}(t)$ nearest to $\mathbf{r}_i(t)$ and $\mathbf{n}(t)$ is the unit vector normal to the interface in the direction of the local density gradient $\nabla\bar{\rho}(\mathbf{r},t)\ _{\mathbf{r}=\mathbf{s}^*(t)}$. For definiteness and without loss of generality, we take the value of $a_i$ to be positive if atom $i$ is on the Fe-poor side of the interface and negative if on the Fe-rich side. We can then count how many atoms of each type exist in each of the two phases at every time step of the simulation. In performing this count, we exclude those atoms in the interfacial region, for which $|a_i| < \delta$. Then, similarly to the density profile determined by the (Widom, 1982) method, we can determine the compositions of each phase.

### 3.9.3 Two-Phase Phase Diagrams

A phase diagram of the two co-existing phases can be constructed independently from two-phase interface methods discussed above. We can relate the compositions of the two coexisting phases by setting the chemical potentials of each phase, $\mu_A$ and $\mu_B$, equal to each other such that:

$$\mu_A = \mu_B \equiv W(1 - x_A)^2 + RT \ln x_A = W x_A^2 + RT \ln(1 - x_A) \tag{3.134}$$

where $W$ is an interaction parameter (to be discussed below), $R$ is the universal gas constant, and $x_A + x_B = 1$. Note: I will refer to phase $A$ as the MgO phase. Equation 3.134 can be rearranged such that:

$$\frac{x_{MgO}}{1 - x_{MgO}} = \exp\left[-\frac{W(P,T)(1 - 2x_{MgO})}{RT}\right] \tag{3.135}$$

in which a root finding algorithm is implemented to solve for $x_{MgO}$. To computed the interaction parameter $W$, homogeneous MD simulations at intermediate compositions on the phase $A$ and $B$ join are performed. The enthalpy $H$, the volume $V$, and the entropy $S$ using the 2PT method are determined. We find that the results are well represented by a symmetric regular solution with excess quantities:

$$\Delta H_{ex} = W_H x_{MgO}(1 - x_{MgO}) \tag{3.136}$$

$$\Delta S_{ex} = W_S x_{MgO}(1 - x_{MgO}) \tag{3.137}$$

$$\Delta V_{ex} = W_V x_{MgO}(1 - x_{MgO}) \tag{3.138}$$

and are the excess enthalpy, entropy, and volume of mixing. $W_i$ are the interaction parameters, and $x_{MgO}$ is the composition. Combining the three interaction parameters leads us to:

$$W(P,T) = W_H - TW_S + PW_V \tag{3.139}$$

which can be substituted into equation 4.5. The critical temperature, above which a single phase exists is:

$$T_C = \frac{W_H + PW_V}{2R + W_S} \tag{3.140}$$

so that $dT_C/dP = W_V/(2R + W_S)$.

We find that determining the solvus closure temperature from the homogeneous MD simulations agrees very well with the results from the two-phase simulations, and leads to an independent method of determining the coexistence of two-phases by from the energetics of mixing.

# CHAPTER 4

# Miscibility of MgO in Liquid Iron

## 4.1 Introduction

Lithophile elements have very limited solubility in Earth's core today. However, the chemical interaction between core and mantle in the early Earth may have been more extensive (Chidester et al., 2022a; Badro et al., 2016; Hirose et al., 2017). Higher temperatures in the early Earth, due to accretional energy, and increased radioactive heat production, may have lead to much greater lithophile element solubility in the core. Lithophile elements may therefore serve as tracers of processes occurring during the hottest portions of Earth's history. Super-Earths are expected to have much higher temperatures in their interiors than Earth and it is possible that lithophile element solubility in the Fe-rich cores of such bodies is more extensive than in Earth (Stixrude, 2014). The temperature in the interiors of terrestrial planets early may be sufficiently high that oxide and metals are completely miscible, forming a single homogeneous liquid (Walker et al., 1993; Wahl and Militzer, 2015). Such a situation may have existed in portions of the earliest Earth, and may exist in the interiors of super-Earths.

Hindering our knowledge of lithophile element solubility in metallic cores is the lack of a clear picture of the chemical reactions involved. For example, it is not clear whether lithophile cations should be viewed as exchanging with Fe, a picture which is used to understand the partitioning of moderately siderophile elements (Wood, 2008), or dissolving as an oxide in the metal (Badro et al., 2018). These two pictures have contrasting implications for how we

view the electronic structure and bonding of lithophile elements in the metal.

A better understanding of lithophile solubility in the core is also important for testing a model of the generation of Earth's earliest magnetic field. Paleomagnetic evidence shows that the existence of Earth's field extends back to at least 3.5 Ga (Biggin et al., 2009) and possibly earlier (Tarduno et al., 2015), but how this field was produced prior to onset of inner core growth at 0.5-1.0 Ga (Labrosse, 2003), is unclear. It has been proposed that exsolution of lithophiles upon cooling of the core, and in particular Mg, may have driven the early dynamo (O'Rourke and Stevenson, 2016; O'Rourke et al., 2017; Badro et al., 2018; Wilson et al., 2022). However, the rate of exsolution of lithophiles on cooling is still poorly constrained.

To address these issues, we explore the interaction between the most abundant lithophile component (MgO) and Fe metal over a wide range of pressure and temperature that encompasses their complete miscibility and the conditions expected during the lithophile exsolution that may have driven the early magnetic field. We perform two-phase simulations, which allow us to determine the way in which lithophile elements are incorporated in the metal, to quantify the composition of the two coexisting phases (Fe-rich and oxide-rich), their structure, and bonding. To provide additional constraints on the phase diagram and to gain additional insight core-mantle reaction, we also perform a series of homogeneous phase calculations to quantify the energetics of mixing, which confirm that the MgO-Fe system displays remarkably simple, symmetric regular solution behavior.

## 4.2 Theory

Our two-phase simulations are initiated as domains of pure Fe liquid and pure MgO liquid joined at planar interfaces (Fig. 4.1 left). During the course of the two phase simulations the system responds by establishing a dynamic equilibrium in which the composition of the two coexisting phases is stationary (Fig. 4.1 center). We quantify the compositions of the two

coexisting phases in two ways (Xiao and Stixrude, 2018). First, we use the one-dimensional density profile normal to the interface, which we find follows the expected hyperbolic tangent form (Widom, 1982):

$$\rho(z) = \rho_2 + \frac{\rho_1 - \rho_2}{2} \sum_{j=1}^{2} (-1)^j \tanh \frac{(z - z_1) - \mathrm{nint}(z - z_1) + (-1)^j w}{\delta} \tag{4.1}$$

where $\rho_1$ is the number density of an atom type (Fe, Mg, or O) in the phase whose center of mass is located at scaled coordinate $z_1$, $w$ is the half-width of the phase, $\rho_2$ is the number density of that atom type in the other phase, $\delta$ is the width of the interface, the nint function accounts for periodic boundary conditions, and the sum accounts for the presence of two interfaces. An example of a fit of this form to our results is shown in Figure 4.1 (right).

Second, we use the approach of (Willard and Chandler, 2010). Define a coarse-grained density field by convolving atomic positions with a Gaussian

$$\bar{\rho}(\mathbf{r}, t) = \sum_i (2\pi\xi^2)^{-3/2} \exp\left[ -(\mathbf{r} - \mathbf{r}_i)^2 / 2\xi^2 \right], \tag{4.2}$$

where $\mathbf{r}_i$ is the position of atom $i$, the sum is over the Fe atoms, and $\xi$ is the coarse-graining length, which we take to be 2.4 Å. We locate the interface $\mathbf{s}$ at every time step such that

$$\bar{\rho}(\mathbf{s}, t) = c \tag{4.3}$$

where we set the density of the interface $c$ to approximately 1/2 the bulk density of the Fe atoms. The interfaces determined in this way are shown in Figure 4.1 (left, center). The interface remains quasi-planar throughout the course of the simulation, with the magnitude of fluctuations of the interface related to the surface tension (Buff et al., 1965). The time-averaged interface is planar and represents the Gibbs dividing surface.

With this definition of the interface, we can now assign each atom to one of the two phases. The proximity of each atom to the interface is

$$a_i(t) = \{[\mathbf{s} - \mathbf{r}_i(t)] \cdot \mathbf{n}(t)\}|_{\mathbf{s}(t)=\mathbf{s}_i^*(t)} \tag{4.4}$$

where $\mathbf{s}_i^*(t)$ is the point on $\mathbf{s}(t)$ nearest to $\mathbf{r}_i(t)$ and $\mathbf{n}(t)$ is the unit vector normal to the interface in the direction of the local density gradient $\nabla\bar{\rho}(\mathbf{r},t)\ _{\mathbf{r}=\mathbf{s}^*(t)}$. For definiteness and without loss of generality, we take the value of $a_i$ to be positive if atom $i$ is on the Fe-poor side of the interface and negative if on the Fe-rich side. We can then count how many atoms of each type exist in each of the two phases at every time step of the simulation. In performing this count, we exclude those atoms in the interfacial region, for which $|a_i| < \delta$.

We gain additional insight into our system by performing homogeneous molecular dynamics simulations at intermediate compositions on the MgO-Fe join. From these simulations, we determine the enthalpy $H$, the volume $V$, and the entropy $S$ using the two-phase thermodynamic (2PT) method (Desjarlais, 2013; Wilson et al., 2021). We find that our results are well represented by a symmetric regular solution, for which the excess quantities $\Delta H_{ex} = W_H x_{MgO}(1 - x_{MgO})$, $\Delta S_{ex} = W_S x_{MgO}(1 - x_{MgO})$, and $\Delta V_{ex} = W_V x_{MgO}(1 - x_{MgO})$ are the excess enthalpy, entropy, and volume of mixing, $W_i$ are the interaction parameters, and $x_{MgO}$ is the composition, which we take to be $x_{MgO} = [\mathrm{MgO}]/([\mathrm{MgO}] + [\mathrm{Fe}])$. The compositions of the two coexisting phases are then related by

$$\frac{x_{MgO}}{1 - x_{MgO}} = \exp\left[-\frac{W(P,T)(1 - 2x_{MgO})}{RT}\right] \tag{4.5}$$

where $W(P,T) = W_H – TW_S + PW_V$, and $R$ is the universal gas constant. The critical temperature, above which a single phase exists is

$$T_C = \frac{W_H + PW_V}{2R + W_S} \tag{4.6}$$

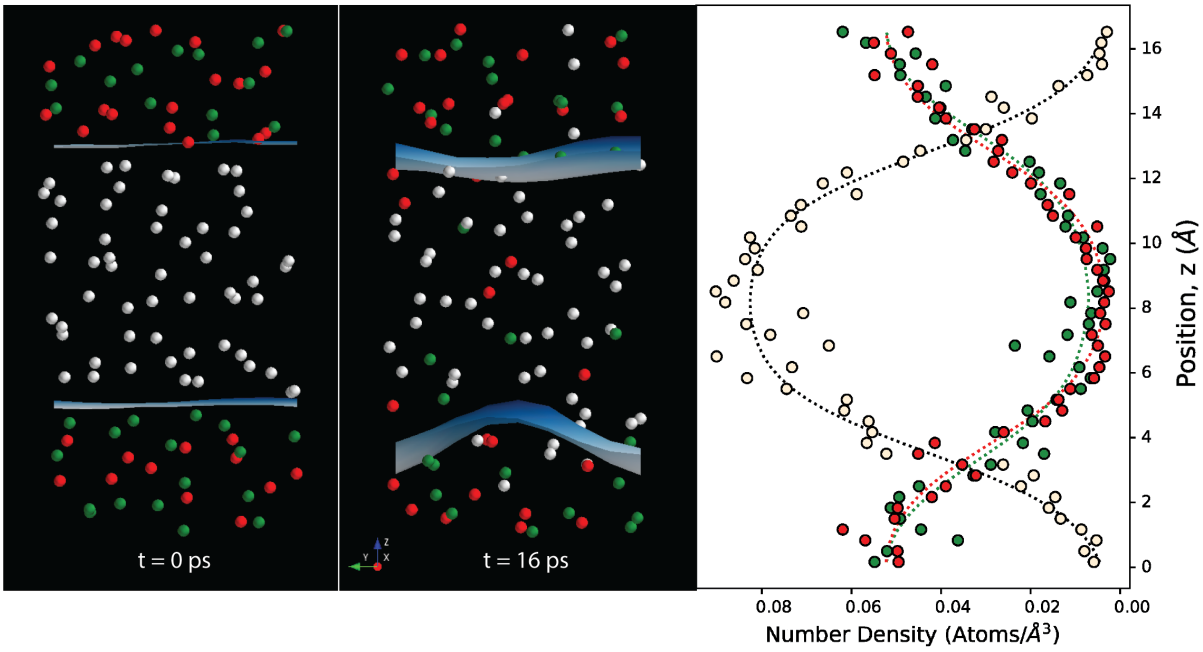


**Figure 4.1:** Simulation snapshots of the two-phase system at 6000 K and 60 GPa. Fe atoms are represented by tan spheres, Mg atoms by green spheres, and O by red spheres. The interface is illustrated by the blue surface, separating Fe-rich and oxide-rich phases. The initial configuration is on the left and an equilibrated snapshot at 16 ps in the center. The rightmost figure shows the one-dimensional density determined from the equilibrated portion of the simulation (16-18 ps) and the lines are fits to Eq. 5.1.

so that $dT_C/dP = W_V/(2R + W_S)$. The exsolution rate of MgO is then simply related to the temperature derivative of equation 4.5.

While our focus is on liquid-liquid phase equilibria, and all of our simulations are in the liquid state, for completeness, we can also use our results to estimate solid-liquid equilibria as well. The MgO content of liquid coexisting with (pure) MgO crystal is governed by

$$W(1 - 2x_{MgO}) + RT \ln x_{MgO} + G_{liq}^{MgO} = G_{xtl}^{MgO} \tag{4.7}$$

where $G_{liq}^{MgO}$ and $G_{sol}^{MgO}$ are the Gibbs free energy of pure liquid and solid MgO, respectively,

and $G_{xtl}^{MgO} - G_{liq}^{MgO} = \Delta S(T - T_{melt})$. For the purpose of this calculation, we adopt values of the temperature $T_{melt}$ and entropy $\Delta S$ of melting from the study of (Alfe, 2005).

We also use one phase simulations to derive additional insight into the structure of oxide-metal fluids on the MgO-Fe join by computing the radial distribution function (McQuarrie, 1975), ionic charges, and bond lifetimes. We compute ionic charges according to the Bader analysis (Tang et al., 2009; Sanville et al., 2007; Henkelman et al., 2006; Yu and Trinkle, 2011). The lifetime of each atom-pair is estimated from

$$\tau = \int_0^\infty \beta(t) dt'. \tag{4.8}$$

with bond auto-correlation function

$$\beta(t) = \left\langle \frac{b_{ij}(t_0) \cdot b_{ij}(t_0 + t)}{b_{ij}(t_0)^2} \right\rangle \tag{4.9}$$

where $b_{ij}(t) = 1$ if a bond between atoms $i$ and $j$ exist at time $t$, and $b_{ij}(t) = 0$ otherwise. We take the bond cutoff criteria to be the distance to the first minimum in the corresponding radial distribution function.

## 4.3 Computation

All simulations are based on density functional theory, using the projector augmented wave (PAW) method (Kresse and Joubert, 1999) as implemented in the Vienna *ab initio* Simulation Package (VASP) (Kresse and Furthmüller, 1996). We use the PBEsol generalized gradient approximation (Perdew et al., 2008), which we have previously shown to yield excellent agreement with experiment in Fe-bearing oxides (Holmström and Stixrude, 2015). To account for strong correlation, we use the +U method (Anisimov et al., 1997) with $U - J$ =2.5 eV (Holmström and Stixrude, 2015). We use PAW potentials of 14, 8, and 6 valence electrons of Fe, Mg, and O with core radii of 1.16, 1.06, and 0.82 Å, respectively.

Our simulations are spin-polarized. In order to compare with previous results, which were non-spin polarized, we also perform non-spin polarized simulations. We sample the Brillouin zone at the Gamma point and use a plane-wave cutoff of 500 eV, which we find yields pressure and energy convergence to within 0.5 GPa and 3 meV/atom, respectively. We assume thermal equilibrium between ions and electrons via the Mermin functional (Mermin, 1965), and thermodynamic averages are computed after discarding 20 % of the time steps to allow for transients; uncertainties are computed via the blocking method (Flyvbjerg and Petersen, 1989).

We perform two-phase simulations in the canonical ensemble (constant $NVT$) using a Nóse-Hoover thermostat (Nosé, 1984b, 1991; Hoover, 1985; Frenkel and Smit, 2001) with a time step of 1 fs for a duration of 10-25 ps. We prepare the initial condition by first performing homogeneous simulations to ensure that the Fe liquid and the MgO liquid initially have the same pressure, temperature, and volume. In the lower pressure regime, the volume of the cell is 1162.83 $\text{Å}^3$ and contains 31 MgO units and 55 Fe atoms, while in the higher pressure regime, the volume of the cell is 910.12 $\text{Å}^3$. In these isochoric simulations the pressure increases linearly on heating: the pressure of equilibrated systems range from 55 GPa (5000 K) to 68 GPa (7000 K) in the lower pressure regime and from 135 GPa (5000 K) to 171 GPa (9000 K) in the higher pressure regime.

For the homogeneous systems our simulations are in the $NPT$ ensemble (Parrinello and Rahman, 1980, 1981), with a Langevin thermostat (Allen and Tildesley, 2017; Hoover et al., 1982; Evans, 1983), and a time step of 1 fs for 15 ps. These simulations were run at 60 GPa and 10,000 K and consisted of 64 atoms comprising several compositions across the MgO-Fe join. We derive the enthalpy and the volume from these $NPT$ simulations. For the entropy, we found that the $NPT$ simulations were not appropriate as the Langevin thermostat biases the velocity auto-correlation function. Therefore, once we determine the equilibrium volume at a given pressure, we continue at that volume in the canonical ensemble for an additional 15 ps, from which we derive the absolute entropy using the two-phase thermodynamic (2PT)

method (Desjarlais, 2013; Wilson and Stixrude, 2021).

## 4.4 Results

We find two coexisting phases in dynamic equilibrium each with a stationary composition: one Fe-rich and one oxide-rich. In both phases, the concentration of Mg and O are equal to each other, i.e. MgO behaves as a component at all pressure-temperature conditions we investigated. Figure 4.1 shows the result of a typical simulation at 60 GPa and 6000 K, showing small, non-zero concentration of MgO in the Fe-rich phase and a nearly equal concentration of Fe in the MgO-rich phase.

The concentration of MgO in the Fe-rich phase and the concentration of Fe in the MgO-rich phase increase on heating (Fig. 4.2). The two phases become completely miscible at a critical temperature of 7000 K at 68 GPa, and at 9000 K at 171 GPa. Our results are consistent with symmetric regular solution behavior. We find good agreement with previous experiments (Badro et al., 2018), but disagree with a previous theoretical study, which found a significantly lower critical temperature (Wahl and Militzer, 2015). We attribute the latter disagreement to the neglect of spin-polarization in the previous study. To test the significance of spin-polarization, we also determined the phase diagram with non spin-polarized simulations and find a significantly lower critical temperature, in better agreement with (Wahl and Militzer, 2015).

We compute the phase diagram independently, from our determinations of the energetics of mixing, and find excellent agreement with our two-phase simulations (Fig. 4.2). The energetics of mixing show that immiscibility originates in a positive enthalpy of mixing, and that the increase of the critical temperature with increasing pressure originates in a positive volume of mixing (Fig. 4.3). The excess entropy of mixing is also positive and similar in magnitude to the ideal entropy of mixing of MgO and Fe components. We confirm that the Gibbs free energy of mixing is negative across the join at super-critical temperature,

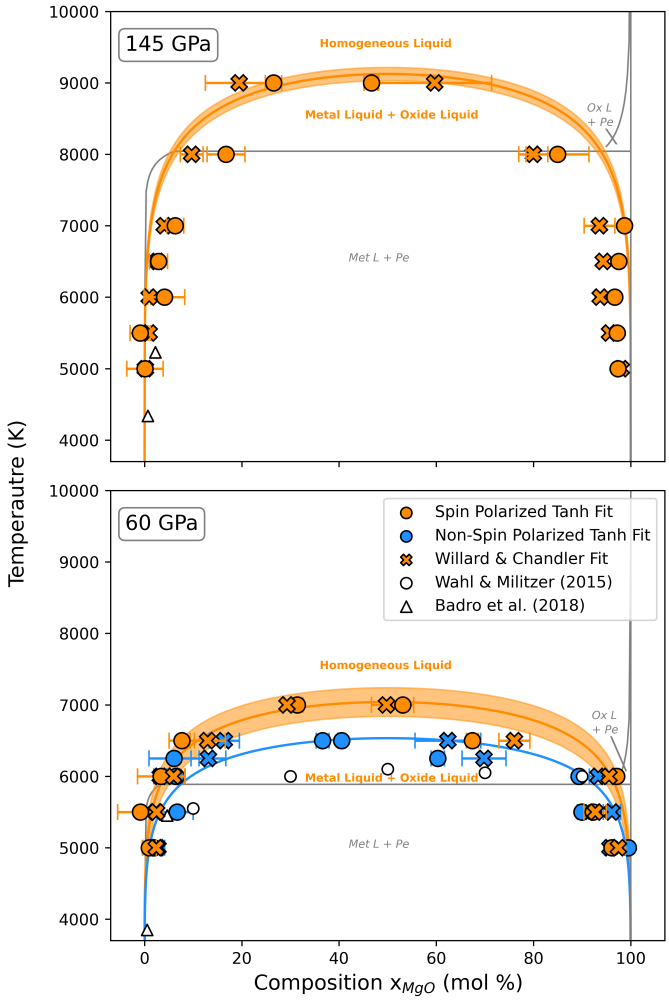


**Figure 4.2:** Phase diagrams in the low (bottom) and high (top) pressure regimes. Composition determined from equation 5.1 are in circles (orange = spin-polarized and blue = non-spin polarized), and from the (Willard and Chandler, 2010) method in X's. White symbols represent previous studies: theoretical results from (Wahl and Militzer, 2015) in circles and experimental data from (Badro et al., 2018) in triangles. The orange curve is the regular symmetric solvus computed from equation 4.5. The gray lines represent the computed phase diagram including the stability of crystalline MgO. The figures are labelled by the pressure at 6000 K.

consistent with our finding of a single homogeneous fluid in our two-phase simulations.

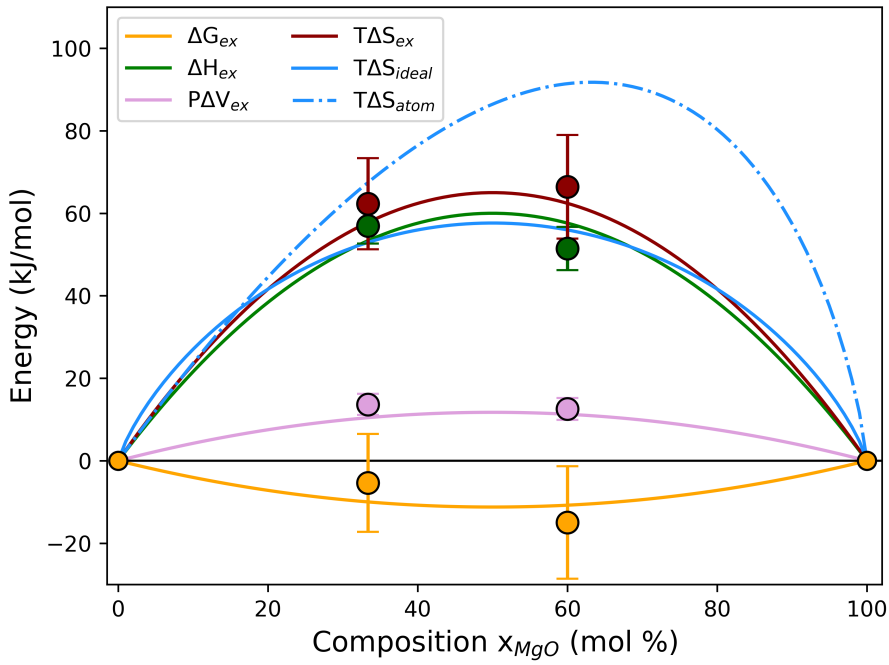


**Figure 4.3:** Energetics of mixing at 60 GPa and 10,000 K, showing the results of our simulations (symbols) and symmetric regular solution fits (lines) for the enthalpy (green), the entropy (red), and the volume (purple). We also compute the excess Gibbs free energy of mixing $\Delta G_{ex} = \Delta H_{ex} - T\Delta S_{ex} + PV_{ex}$ (orange). The symmetric regular solution fits yield $W_H = 240 \pm 12.01$ kJ/mol, $W_S = 26 \pm 0.10$ J/(K $\cdot$ mol), and $W_V = 1.3 \pm 0.07$ Å$^3$/mol. We compare with the ideal entropy of mixing assuming Fe and MgO as components (blue solid line) and assuming Fe, Mg, and O as components (blue dashed line).

The exsolution rate increases with increasing temperature and decreases with increasing pressure (Fig. 4.4). The exsolution rate is less than 2 x $10^{-5}$ K$^{-1}$ at all temperatures less than 5500 K. Our results at 60 GPa are similar in magnitude to previous experimental results (Du et al., 2017; Badro et al., 2018). The study of (Badro et al., 2018) also find that the exsolution rate increases with increasing temperature, albeit more gradually than what

we find, while the study of (Du et al., 2017) find that the exsolution rate decreases with increasing temperature.

The radial distribution function gives us additional insight into the microscopic interactions between components. The radial distribution function of the mixed homogeneous fluid ($x_{MgO}$=0.6) at 10,000 K and 60 GPa, shows distinct peaks for Mg-O, Fe-O, and Fe-Fe interactions. We compare these with the radial distribution functions computed for pure Fe, and pure MgO fluids at the same conditions. We find that $g_{Mg-O}$ and $g_{Fe-Fe}$ are very similar in the mixed and the pure fluids: in the mixed fluid, the first coordination shell is slightly less distinct: the height of the first maximum in $g(r)$ is slightly less and the first minimum occurs at larger distances. The Mg-O coordination number in the mixed fluid is much greater than that of the Fe-O coordination number (5.95 vs. 3.07). We find that bonds within the first coordination shell have very short lifetimes: for example, in the mixed fluid, the lifetime of Mg-O bonds is 155 fs, as compared with 60 fs for the vibrational period of the TO mode in periclase at a similar pressure.

Ionic charges are similar in oxide-rich and Fe-rich phases (Fig. 4.6). The ionic charge of Mg and Fe are the same within standard deviation in MgO-rich and Fe-rich phases, while in the case of oxygen, the charge is slightly less negative in the Fe-rich phase (by 0.3). Moreover, the ionic charges of the atoms are very similar to their values in the corresponding pure phases (pure MgO or pure Fe).

## 4.5 Discussion

Previous studies leave uncertain the nature of the interaction between MgO and Fe, as epitomized by the chemical reactions (Badro et al., 2018)

$$\text{Dissolution: } MgO^{oxide} \rightleftharpoons MgO^{metal} \tag{4.10}$$

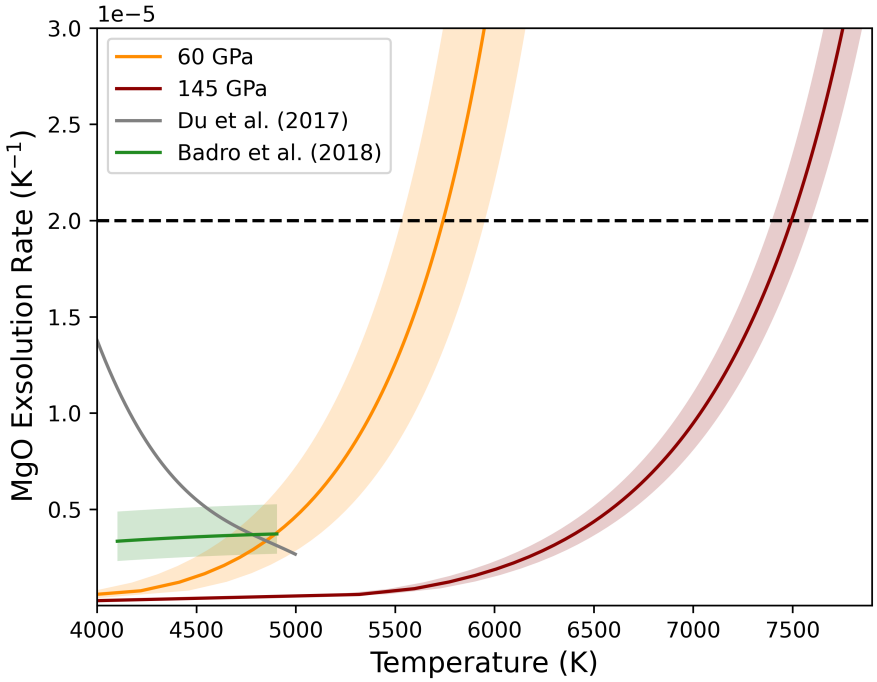


**Figure 4.4:** Exsolution rate of MgO from the Fe-rich fluid at 60 GPa (orange) and 145 GPa (red). Exsolution rates are compared with previous experimental studies from (Du et al., 2017) (gray) and (Badro et al., 2018) (green). The dashed line represents the exsolution rate that must be exceeded in order to produce a dynamo according to (O'Rourke et al., 2017).

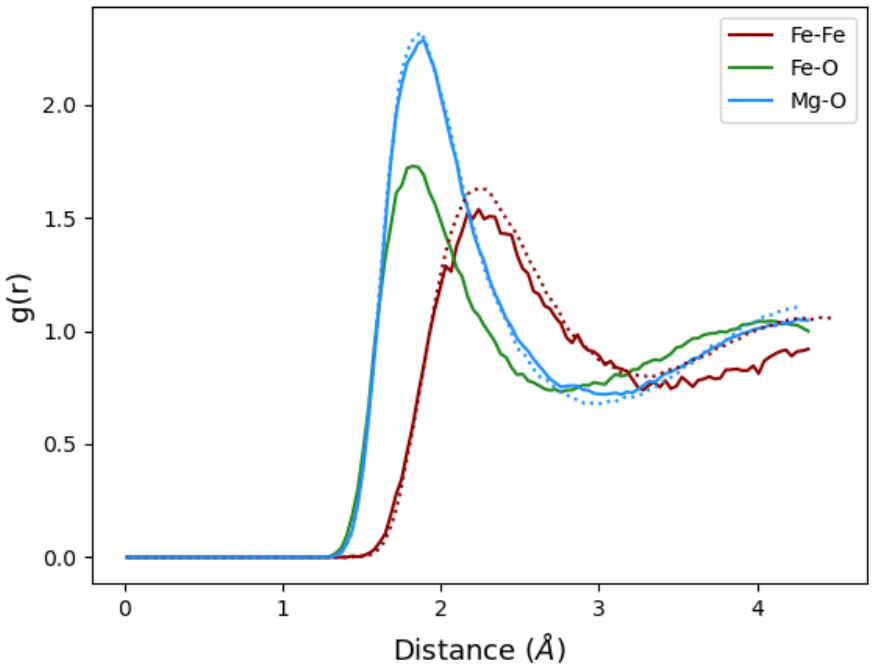


**Figure 4.5:** Radial distribution functions of the homogeneous fluid with $x_{MgO}$=0.6 at 10000 K and 60 GPa (solid lines) compared with the same pair distributions in the pure phases (dashed lines).

$$\text{Dissociation: } MgO^{oxide} \rightleftharpoons Mg^{metal} + O^{metal} \tag{4.11}$$

$$\text{Exchange: } MgO^{oxide} + Fe^{metal} \rightleftharpoons FeO^{oxide} + Mg^{metal} \tag{4.12}$$

The first views MgO as dissolving as a component in the metal phase. The second also involves dissolution, but views Mg and O as separate, dissociated components once dissolved in the metal. The third has also been widely used to understand the partitioning of moderately siderophile elements between oxide and metal ((Wood et al., 2008; Wood, 2008)). Previous experimental studies disagree on whether the exchange reaction, or the other two, can best represent experimental measurements (Du et al., 2017; Badro et al., 2018; Chidester et al.,

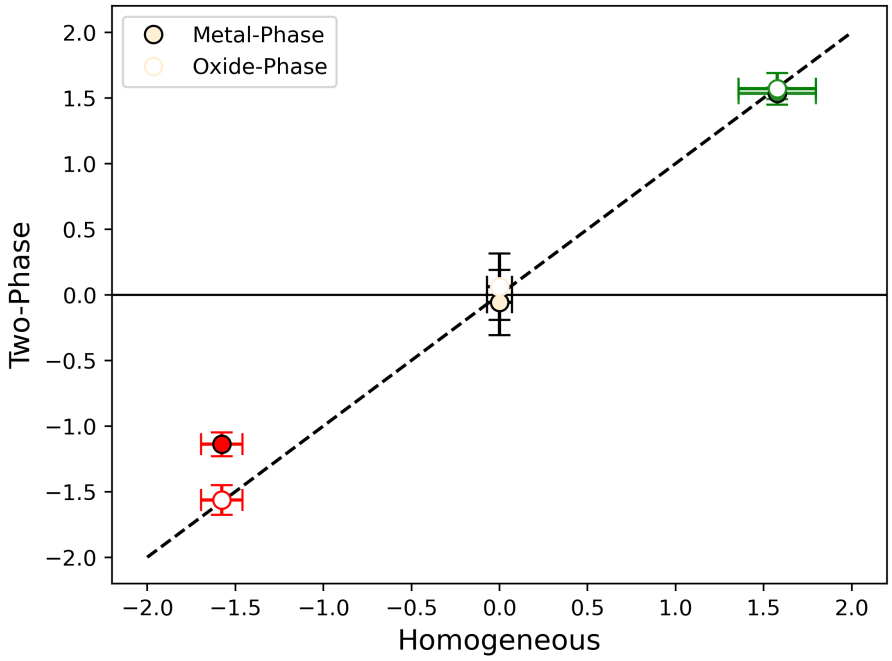


**Figure 4.6:** Mean values of the ionic charge for each atom type (Mg: green, O: red, Fe: tan) in each of the two phases (closed: Fe-rich phase, open: MgO-rich phase) from our two-phase simulation at 60 GPa, 6000 K, compared with their values in the corresponding pure phases (pure MgO or pure Fe liquid) at the same conditions. Error bars indicate the standard deviation in the value.

2022b). Previous theoretical studies have assumed that MgO is incorporated in Fe-rich liquid as a component (Wahl and Militzer, 2015; Wilson et al., 2022).

Our results point towards the dissolution mechanism as the best representation of MgO-Fe reaction. We find that MgO behaves as a component, with Mg and O concentrations equal to each other in both oxide-rich and Fe-rich phases over the entire range of pressure and temperature that we have considered, excluding the exchange mechanism. Our results favor the dissolution mechanism over the dissociation mechanism. In the dissociation mechanism, Mg and O are viewed as separate components, with implications for the ideal entropy of

mixing. Whereas we find that the phase diagram is symmetric, consistent with mixing between MgO and Fe components and the dissolution mechanism, ideal mixing among Mg, O, and Fe, introduces asymmetry to the ideal entropy of mixing on the MgO-Fe join that is inconsistent with our results (Fig. 4.3).

The dissolution mechanism does not imply covalent bonding between Mg and O, as argued by (Badro et al., 2018). Indeed, we find no such bonding, with ionic Mg-O bonds surviving for no more than two vibrational periods, and O atoms rapidly exchanging within the first coordination shell of the Mg cation. Moreover, the ionic charges of Mg and O are very similar in the metal and the oxide phases, indicating that Mg and O are still ionically, rather than covalently bonded in the metal phase.

We find that the rate of MgO exsolution from the metal phase is insufficient to drive a dynamo. Previous studies have argued that an exsolution rate of at least 2 x $10^{-5}$ $K^{-1}$ is required (O'Rourke et al., 2017). We find that the exsolution rate does not exceed this value for temperature less than 5500 K. It is possible that the core produced a magnetic field when the core temperature was as high as 5500 K, but cooling from this state would likely have been very rapid and such a magnetic field very short-lived. We have investigated a simplified chemical system and it is possible that the rate of exsolution of MgO in a multi-component system may differ from what we find. However, experiments show that the activity of Mg in the metal phase depends little on the presence of other elements. For example (Chidester et al., 2022b) find $\epsilon^i_{Mg} = 0$ for all elements $i$ except for $i = O$, for which they find a negative value, in accord with our finding of strong affinity Mg and O. On the other hand, the same study found that the activity of MgO in the oxide phase does depend on the silica concentration in the oxide phase, with a value of the interaction parameter $W_{MgO-SiO_2}$ that is in excellent agreement with previous theoretical studies (de Koker et al., 2013).

An important issue related to exsolution of light elements that has received relatively little attention is the pressure dependence of exsolution. The exsolution-driven dynamo scenario envisions exsolution first occurring at the top of the core, and this is in accord

with experimental findings that the pressure-dependence of exsolution is either weak or undetectable (O'Rourke and Stevenson, 2016; Badro et al., 2018; Chidester et al., 2022b). However, we find significant pressure dependence: $dT_C/dP = 24$ K/GPa, which is much greater than the expected adiabatic gradient in the core $\Gamma = 7$ K/GPa. If $dT_c/dP > \Gamma$ as we find, then exsolution begins at the bottom of the core, the exsolution of light elements leads to a stable stratification, and does not contribute to producing a dynamo (Landeau et al., 2022). The origin of the apparent discrepancy between our results and experiment is not clear. It is possible that experimental detection of pressure dependence is confounded by co-variance with other experimental parameters together with pressure, such as temperature, and bulk composition. It is also possible that the pressure dependence of exsolution is diminished in systems that are more chemically rich than the simplified system that we have focused on.

## 4.6 Conclusions

Lithophile element solubility in the core may have been much more extensive in the early Earth when temperatures were hotter, or in Super-Earths, where the larger planetary size may lead to much higher interior temperatures. The critical temperature that we find (7000 K at 60 GPa) means that complete miscibility of Fe and MgO cannot be excluded. By examining the entire MgO-Fe join in the liquid state, we find remarkably simple behavior: a symmetric regular solution between the two end-members. Our simulations favor the dissolution picture of lithophile-Fe interaction, in which MgO is viewed as a component that is not dissociated. Mg and O remain ions of near nominal charge in the metal liquid and Mg-O bonds last for only a short time.

Our results do not support the notion that the early magnetic field was generated by exsolution of MgO from the core. The rate of exsolution on cooling that we find is too small. Moreover, we find that exsolution likely initiated at the bottom of the core, rather than the

top, in which case exsolution would not have provided a driving force for fluid motions. Other mechanisms for producing the Earth's earliest field should be further explored, including the exsolution of lithophiles other than Mg from the core, or a silicate dynamo (Stixrude et al., 2020).

# CHAPTER 5

# Complete Solubility of Rock and Iron at High Pressure and Temperature

## 5.1 Introduction

The chemical interaction of the major planetary building blocks: rock and iron, set the first order separation of terrestrial bodies into mantle and core. This interaction may be much more extensive in the earlier, hotter portions of planetary evolution, and may impact our understanding of the early generation of the magnetic field through subsequent exsolution of lithophiles from the core, the origin of the light element in the core, and the partitioning of iron, oxygen, and other major elements between mantle and core.

The partitioning of major siderophile and lithophile elements between metal and silicate phases within the Earth is likely influenced by its accretionary and core formation history. Moderately siderophile elements are commonly used to better understand the accretionary stages of Earth's history (Wood, 2008). However, recent studies suggest that the partitioning of lithophile elements that typically occur in the silicate phases may be affected by core formation processes at very high temperature and pressure conditions, causing them to also partition in metal phases. High temperature and pressure partitioning in the early Earth may lead to geochemical behavior that is very different from what is observed in the current Earth. The amount of lithophile elements partitioned into the core may provide crucial insights into the process of core formation for both terrestrial planets and exoplanets.

The composition of the Earth's core can have a significant impact on important dynamic

processes, such as the generation of an early dynamo. One proposed explanation of this dynamo involves extensive chemical reactions between mantle and core materials, which occur at high temperatures after the process of accretion. As the initially homogeneous solution cools, an lithophile-rich phase exsolves providing a buoyancy force for the core dynamo (O'Rourke and Stevenson, 2016; O'Rourke et al., 2017).

The interaction between molten rock and metal at the conditions of the early Earth are still only incompletely known. While experiments have explored reactions between crystalline bridgmanite and liquid iron, and between molten iron and silicate liquids, these experiments have not explored the entire range of pressure and temperature conditions relevant (to 136 GPa, and $>$ 4000 K) (Takafuji et al., 2005; Fischer et al., 2015; Chidester et al., 2022a). Thus the solubility in the core of Si and O , which have been proposed as the predominant light elements, and Mg, which has been proposed as the crucial constituent of an exsolution-driven dynamo are poorly known. Crucially, the temperature at which rock and iron become completely miscible is unknown.

Here, we advance our understanding of the chemical interaction between rock and iron with ab initio molecular dynamics simulations of the $MgSiO_3$-Fe system. This system represents a first order chemical model of the core-mantle boundary, capturing more than 80 % of the constituents of planetary rock and iron, respectively. We examine the equilibrium compositions of the two phases as well as energetics of mixing and speciation. We explore the solubility of the components of $MgSiO_3$ in liquid iron at higher pressure up to the core-mantle boundary and up to temperatures of complete miscibility.

## 5.2 Theory

Our two-phase simulations are initiated as domains of pure Fe liquid and pure $MgSiO_3$ liquid joined at a planar interface. During the course of the two-phase simulations the system responds by establishing a dynamic equilibrium in which the compositions of the two

coexisting phases are stationary. We first quantify the compositions of the two co-existing phases through a 1D density profile which follows the expected hyperbolic tangent form (Widom, 1982):

$$\rho(z) = \rho_2 + \frac{\rho_1 - \rho_2}{2} \sum_{j=1}^{2} (-1)^j \tanh \frac{(z - z_1) - \text{nint}(z - z_1) + (-1)^j w_1}{\delta} \tag{5.1}$$

where $\rho_1$ is the number density of an atom type (Fe, Mg, Si, or O) in the phase whose center of mass is located at scaled coordinate $z_1$, $w_1$ is the half-width of the phase, $\rho_2$ is the number density of that atom type in the other phase, $\delta$ is the width of the interface, the nint function accounts for periodic boundary conditions, and the sum accounts for the presence of two interfaces. An example of a fit of this form to our results is shown in Figure 5.1.

In this definition of the interface, the functional form is fit to the 1D discrete density profile:

$$\rho(z, t) = \sum_i \delta(z - z_i(t)) \tag{5.2}$$

where $z_i(t)$ is the $i^{th}$ particle's position at time $t$ along the $z$ axis. However, a problem with the method from equation 5.2 requires binning to compute the Dirac delta function, which can result in poor statistical sampling along the 1D density profile. I have therefore explored a method by Coles et al. (2021) as an alternative way to calculate the 1D density profile, which involves force-based estimators with a reduced variance (Coles et al., 2021). First, a general expression for combining estimators is proposed as:

$$E_\lambda(x) = (1 - \lambda)E_0(x) + \lambda E_1(x) = E_0(x) + \lambda \Delta(x) \tag{5.3}$$

where $E_0(x)$ and $E_1(x)$ are estimators of the same property that depend on some parameter $x$ (i.e., distance or position), $\Delta(x) = E_1(x) - E_0(x)$, and $E_\lambda$ denotes another valid estimator of the same property, where the expectation value of $E_\lambda(x)$ is the same as that of $E_0(x)$

and $E_1(x)$. However,the variance of $E_\lambda$ is a quadratic function of $\lambda$, where $\mathrm{var}(E_\lambda(x)) = \langle[E_\lambda(x) - \langle E_\lambda(x)\rangle]^2\rangle$. Therefore, one can find for each $x$ a combination that minimizes the variance:

$$\lambda^*(x) = -\frac{\mathrm{cov}(E_0(x), \Delta(x))}{\mathrm{var}(\Delta(x))} = 1 - \frac{\mathrm{cov}(E_1(x), \Delta(x))}{\mathrm{var}(\Delta(x))} \tag{5.4}$$

which involves the covariances $\mathrm{cov}(A, B) = \langle(A - \langle A\rangle)(B - \langle B\rangle)\rangle$ and provides an optimal estimator $E^*_\lambda(x)$ for each $x$. In practice, the expectation values $\langle E_n(x)\rangle$ and covariances entering equation 5.4 are determined from two given estimators, which then leads to the corresponding optimal estimator $E^*_\lambda(x)$ from equation 5.3.

To compute the 1D density from the force field method, consider the force density:

$$\nabla\rho(\mathbf{r}) = \beta\left\langle \sum_i \delta(\mathbf{r} - \mathbf{r}_i)\mathbf{f}_i \right\rangle \tag{5.5}$$

where $\nabla$ is the gradient operator, $\mathbf{r}_i$ is the position of the particle $i$, $\delta$ is the Dirac delta function, $\beta = 1/k_BT$, and $\mathbf{f}_i$ is the force acting on atom $i$. The density can be obtained by integrating the force density from either side of the simulation cell, leading to the two estimators:

$$\Delta\rho_0(z) = \langle\Delta\hat{\rho}_{\lambda=0}(z)\rangle = \left\langle \frac{1}{S}\sum_i \mathrm{H}(z - z_i)\beta f_{z,i} \right\rangle \tag{5.6}$$

$$\Delta\rho_L(z) = \langle\Delta\hat{\rho}_{\lambda=1}(z)\rangle = \left\langle \frac{1}{S}\sum_i \mathrm{H}(z_i - z)\beta f_{z,i} \right\rangle \tag{5.7}$$

where H is the Heaviside function. The integration constant is determined from the average density

$$\rho_\alpha(z) = \Delta\rho_\alpha(z) - \frac{\int \Delta\rho_\alpha(z)dz}{L} + \frac{N_\alpha}{V} \tag{5.8}$$

where $L$ is the length along the $z$ axis, $N_\alpha$ is the total number atom type $\alpha$, and $V$ is the volume of the system. Following the general expression for combining estimators from equations 5.3 and 5.4, we can obtain the optimal expression for the 1D density profile without the need for any binning (Figure 5.1).

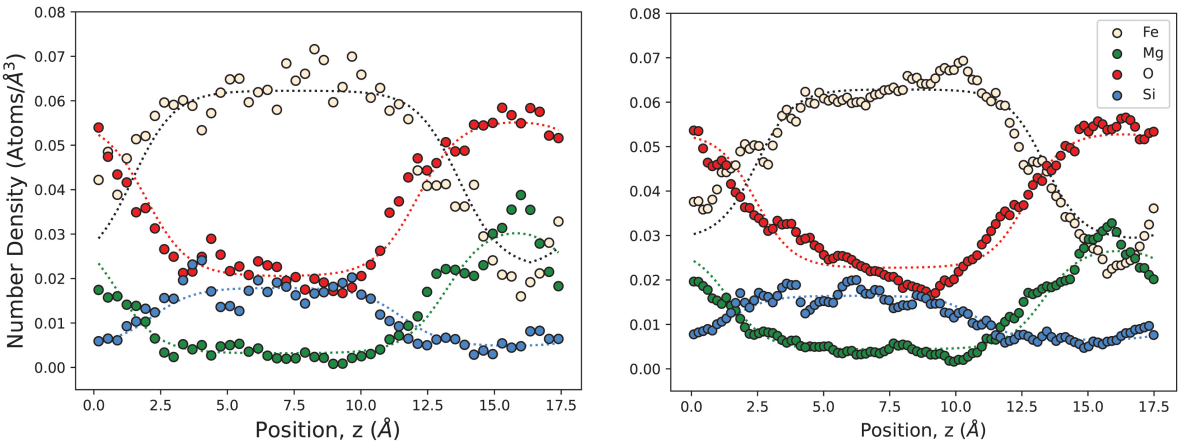


**Figure 5.1:** Comparison of number density calculation methods for discrete binning from equation 5.2 (*left*) versus the force field method from equation 5.3 (*right*) at 5000 K, 57 GPa, and 1356.79 Å$^3$. Tanh fits to both distributions shown in dotted lines.

In the second approach following Willard and Chandler (2010), we first define a coarse-grained density field by convolving atomic positions with a Gaussian:

$$\bar{\rho}(\mathbf{r}, t) = \sum_i (2\pi\xi^2)^{-3/2} \exp\left[-(\mathbf{r} - \mathbf{r}_i)^2 / 2\xi^2\right], \tag{5.9}$$

where $\mathbf{r}_i$ is the position of atom $i$, the sum is over the Fe atoms, and $\xi$ is the coarse-graining length, which we take to be 2.4 Å. The interface, $\mathbf{s}$, is located at every time step such that:

$$\bar{\rho}(\mathbf{s}, t) = c \tag{5.10}$$

where the density of the interface $c$ is set to approximately 1/2 the bulk density of the Fe

atoms. The interfaces determined in this way are shown in Figure 5.2. The time-averaged interface is planar and represents the Gibbs dividing surface.

With this definition of the interface, we can now assign each atom to one of the two phases. The proximity of each atom to the interface is:

$$a_i(t) = \{[\mathbf{s} - \mathbf{r}_i(t)] \cdot \mathbf{n}(t)\}|_{\mathbf{s}(t)=\mathbf{s}_i^*(t)} \tag{5.11}$$

where $\mathbf{s}_i^*(t)$ is the point on $\mathbf{s}(t)$ nearest to $\mathbf{r}_i(t)$ and $\mathbf{n}(t)$ is the unit vector normal to the interface in the direction of the local density gradient $\nabla\bar{\rho}(\mathbf{r},t)\ _{\mathbf{r}=\mathbf{s}^*(t)}$. For definiteness and without loss of generality, we take the value of $a_i$ to be positive if atom $i$ is on the Fe-poor side of the interface and negative if on the Fe-rich side. We can then count how many atoms of each type exist in each of the two phases at every time step of the simulation. In performing this count, we exclude those atoms in the interfacial region, for which $|a_i| < \delta$. Then, similarly to the density profile determined by the (Widom, 1982) method, we can determine the compositions of each phase.

## 5.3 Computation

All simulations are based on density functional theory, using the projector augmented wave (PAW) method (Kresse and Joubert, 1999) as implemented in the Vienna *ab initio* Simulation Package (VASP) (Kresse and Furthmüller, 1996). We use the PBEsol generalized gradient approximation (Perdew et al., 2008), which we have previously shown to yield excellent agreement with experiment in Fe-bearing oxides (Holmström and Stixrude, 2015; Insixiengmay and Stixrude, 2023). To account for strong correlation, we use the +U method (Anisimov et al., 1997) with $U - J = 2.5$ eV (Holmström and Stixrude, 2015). We use PAW potentials of 14, 8, 4, and 6 valence electrons of Fe, Mg, Si, and O with core radii of 1.16, 1.06, 1.312, and 0.82 Å, respectively. Our simulations are spin-polarized. We sample the Brillouin zone at the Gamma point and use a plane-wave cutoff of 500 eV, which we find

yields pressure and energy convergence to within 1 GPa and 5 meV/atom, respectively. We assume thermal equilibrium between ions and electrons via the Mermin functional (Mermin, 1965), and thermodynamic averages are computed after discarding 20 % of the time steps to allow for transients; uncertainties are computed via the blocking method (Flyvbjerg and Petersen, 1989).

We perform two-phase simulations in the canonical ensemble (constant $NVT$) using a Nóse-Hoover thermostat (Nosé, 1984b, 1991; Hoover, 1985; Frenkel and Smit, 2001) with a time step of 1 fs for a duration of 15-30 ps. We prepare the initial condition by first performing homogeneous simulations to ensure that the Fe liquid and the $MgSiO_3$ liquid initially have the same pressure, temperature, and volume. In the lower pressure regime, the volume of the cell is 1162.83 $Å^3$ and contains 16 $MgSiO_3$ units and 68 Fe atoms. In these isochoric simulations the pressure increases linearly on heating: the pressure of equilibrated systems range from 48 GPa (4000 K) to 77 GPa (7000 K).

To gain further insight into our results, we also perform a series of homogeneous simulations in the $NPT$ ensemble (Parrinello and Rahman, 1980, 1981), with a Langevin thermostat (Allen and Tildesley, 2017; Hoover et al., 1982; Evans, 1983), and a time step of 1 fs for 15 ps. We explore properties of homogeneous fluids on the joins Fe-MgO, Fe-$SiO_2$, MgO-$SiO_2$, and Fe-$MgSiO_3$. These simulations were run at 60 GPa and 5000-7000 K depending on the join. We derive the enthalpy and the volume from these $NPT$ simulations. For the entropy, we found that the $NPT$ simulations were not appropriate as the Langevin thermostat biases the velocity auto-correlation function. Therefore, once we determine the equilibrium volume at a given pressure, we continue at that volume in the canonical ensemble for an additional 15 ps, from which we derive the absolute entropy using the two-phase thermodynamic (2PT) method (Desjarlais, 2013; Wilson and Stixrude, 2021).

## 5.4 Results

We find two coexisting phases in dynamic equilibrium each with stationary compositions: one Fe-rich and one oxide-rich. Figure 5.2 shows the result of a typical simulation at 60 GPa and 5000 K, showing small, non-zero concentration of Si, O and Mg in the Fe-rich phase. At low temperatures, we find few Mg atoms in the Fe-rich region, whereas most of the Si and O atoms readily go into the Fe-rich phase with few remaining in the oxide-rich region.

The concentration of Si, O and Mg in the Fe-rich phase increase on heating (Figure 5.3). At the lowest temperatures, Si is much more soluble in the metal phase than either Mg or O. With increasing temperature, increasing amounts of O, and finally Mg enter the metal phase until the two phases become completely miscible at a temperature of 7000 K and 60 GPa. The critical temperature in the silicate-iron system is very similar to that in the MgO-Fe system.

We compute the energetics of mixing from our one-phase homogeneous simulations and show that immiscibility originates in a positive enthalpy of mixing (Figure 5.4). We find that the lowest enthalpy of mixing occurs for the Fe-$SiO_2$ join, the highest enthalpy of mixing occurs for the Fe-MgO join, and the Fe-$MgSiO_3$ join placing in between. The lower enthalpy of mixing for Fe-$SiO_2$ agrees with our finding that Si and O are more miscible in the metal phase than Mg.

## 5.5 Discussion

Our results show that Si and O are readily dissolved into the metal phase at all temperatures, and initially enter the metal-rich portion as a component of nearly SiO composition at low temperatures. At low temperatures, the composition of the oxides in the metal-rich region is comprised of approximately 10 mol % Mg. On heating, Mg begins to go into the metal phase with increasing amounts of Si and O. Comparison to our Fe-MgO simulations and

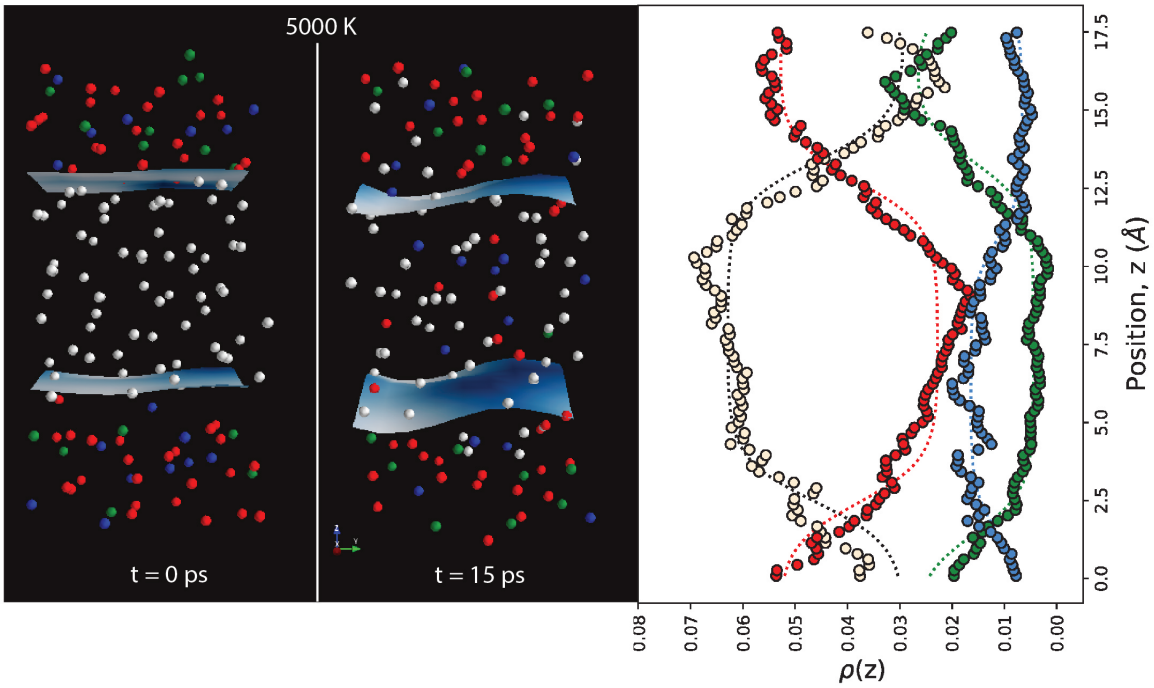


**Figure 5.2:** Simulation snapshots of the two-phase system at 5000 K and 60 GPa. Fe atoms are represented by tan spheres, Mg atoms by green spheres, O atoms by red spheres, and Si atoms by blue spheres. The interface is illustrated by the blue surface, separating Fe-rich and oxide-rich phases. The initial configuration is on the left and an equilibrated snapshot at 15 ps in the center. The rightmost figure shows the one-dimensional density determined from the equilibrated portion of the simulation (10 - 20 ps) and the lines are fits to equation 5.1.

experimental results at similar pressure and temperature conditions show that the amount of Mg in the metal-rich region consists of only a few mol % (Badro et al., 2016, 2018). Thus, the differing results point towards the possibility of increased Mg in the metal-rich regime due to the presence and interactions with SiO.

We compute the interaction parameters from one-phase homogeneous simulations to compare differing Fe-oxide joins. Comparing the enthalpy of mixing of Fe-$SiO_2$, Fe-MgO, and

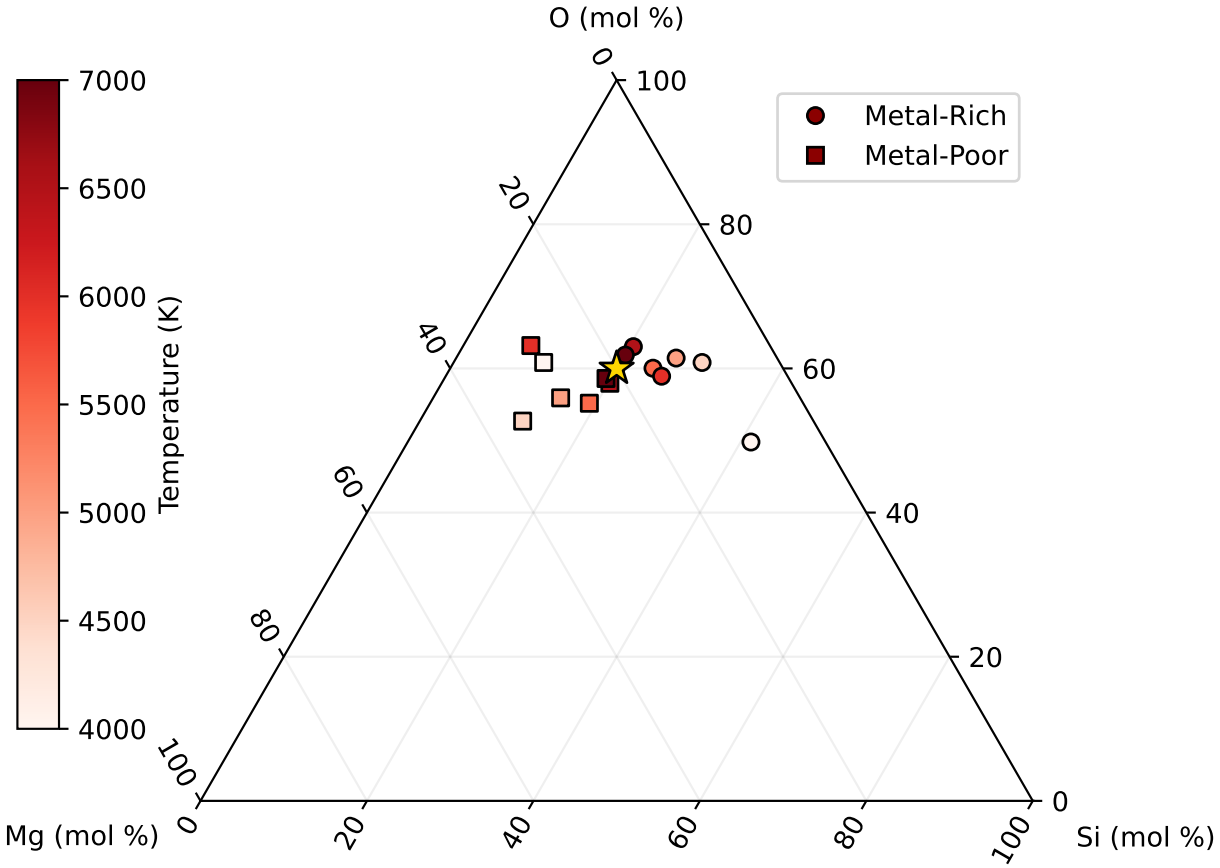


**Figure 5.3:** Mg-Si-O ternary phase diagram in mol % determined by the two-phase simulations. Circles represent the species in the Fe-rich region, squares represent species in the Fe-poor region, and the yellow star represents $MgSiO_3$ composition. The color bar indicates temperatures at which the two-phase simulations are performed at.

Fe-$MgSiO_3$ reveals that Fe-$SiO_2$ is more readily dissolved in the metal phase at high temperatures, followed by Fe-$MgSiO_3$ and Fe-MgO. Our homogeneous and two-phase simulations thus support the notion that Si and O are important light elements in the core. As in my study of the Fe-MgO system, we find that MgO is soluble in the metal phase, but only in small amounts at temperatures below 5000 K. The amount of MgO dissolved in the metal phase and the temperature deendence of the solubility are too small too allow for MgO to

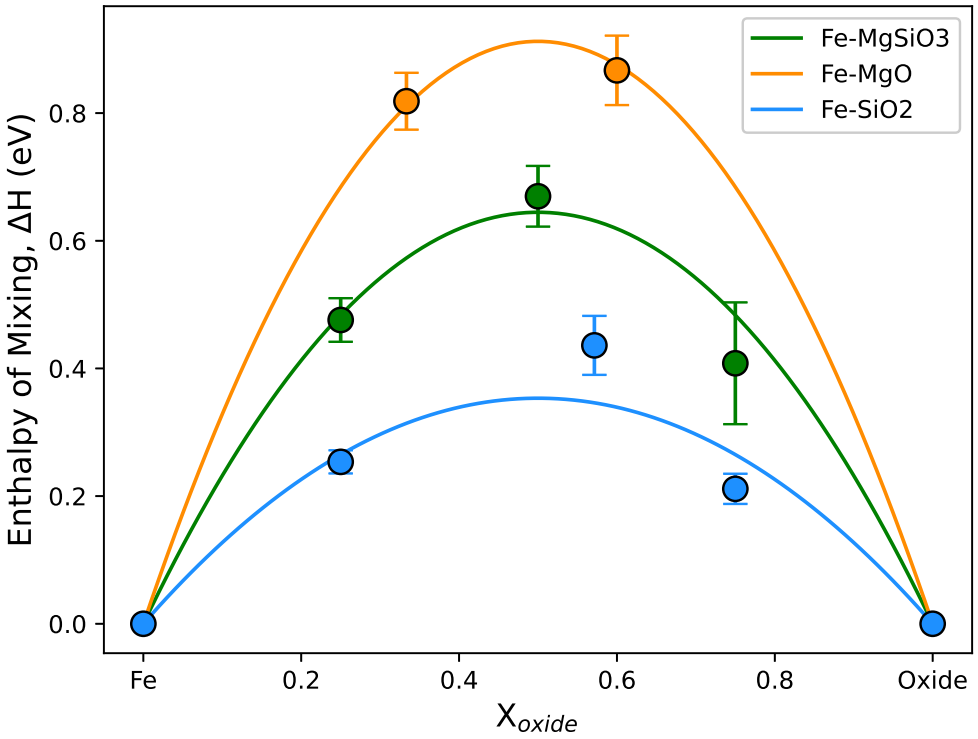


**Figure 5.4:** Excess enthalpy of mixing at 7000 K versus three Fe-Oxide joins: Fe-$SiO_2$ (blue), Fe-MgO (orange), and Fe-$MgSiO_3$ (green). The energetics of mixing is determined by our one phase homogeneous simulations.

be a primary driver of an exsolution dynamo.

From our 1D density profiles, we find small amounts of Fe, and a depletion of Si and O, in the oxide-rich phase, pointing towards a depletion of the mantle. In this context, we note that silica-depleted compositions have been suggested as the origin of the unusual properties of ULVZ (Wicks et al., 2010), and our results suggest that depletion may be a consequence of core-mantle reaction.

## 5.6 Conclusion

We find that complete miscibility of Fe-$MgSiO_3$ at 60 GPa occurs at 7000 K. Temperatures as high as this may have been present in the earliest Earth, for example immediately following the giant impact. The possibility of complete miscibility between rock and metal should be considered in models of the early thermal and chemical evolution of terrestrial planets.

# CHAPTER 6

# Hydrogen Bond Symmetrization and High-Spin to Low-Spin Transition of $\varepsilon$-FeOOH at the Pressure of Earth's Lower Mantle

## 6.1 Introduction

Water is an important component in the mantle, which even in small concentrations can have a large effect on properties such as the melting temperature and viscosity, and thus on thermal evolution. The amount of water stored in the largest part of the mantle, the lower mantle, is still uncertain. This is partly due to the relative inaccessibility of this region, for example few physical samples from the lower mantle are known, in contrast to the increasing number of diamond inclusions and other samples from the transition zone (Pearson et al., 2014; Tschauner et al., 2018). Our uncertainty about the water content in the lower mantle is also due to a comparative lack of understanding of hydrogen bonding at high pressure: in what phases is water crystallographically stored, and what is the effect of water on physical properties at high pressure?

Water storage may be fundamentally different in the lower mantle than in the transition zone. In the transition zone, copious amounts of water may be stored in nominally anhydrous minerals, including wadsleyite and ringwoodite, which have water storage capacities exceeding 1 wt.% (Hirschmann, 2006). In the lower mantle, however, the water storage capacity of the major phases (bridgmanite, ferropericalse, davemaoite), while still uncertain, appears

not to exceed 1200 ppm (Litasov and Ohtani, 2007; Fu et al., 2019; Chen et al., 2020; Liu et al., 2021). If the lower mantle has a water concentration much higher than this, the water must be stored in hydrous phases, i.e. phases in which water is a stoichiometric component.

Phase H is the hydrous phase that is found to be stable in mantle-like whole rock compositions with excess $H_2O$ (Walter et al., 2015) over most of the lower mantle pressure regime (55-125 GPa). These experiments were limited in not containing iron oxide as a component, but other studies have found stable solid solution of phase H encompassing essentially the entire ternary $(Mg,Fe,Al)(Si,Fe,Al)(OOH)_2$ (Nishi et al., 2019), complementing studies of binary joins in this compositional space (Ohira et al., 2019, 2021; Satta et al., 2021).

Our focus here is on the ferric end-member of phase H: $\varepsilon$-FeOOH. $\varepsilon$-FeOOH has an orthorhombic structure with $P2_1nm$ space group that is stable on its own composition from 7 GPa (where it transforms from the lower pressure, goethite phase) to 70 GPa, where it transforms to a pyrite-structured phase (Gleason et al., 2008; Nishi et al., 2017; Suzuki, 2017; Hu and Liu, 2021b). The structure is an orthorhombically distorted rutile derivative with edge- and corner-sharing $FeO_6$ octahedra linked by hydrogen bonds (O-H$\cdots$O) that are asymmetric at low pressure (Pernet et al., 1975; Bolotina et al., 2008). The anhydrous sublattice (arrangement of Fe and O atoms) is identical to the $CaCl_2$ high-pressure polymorph of stishovite.

Under pressure $\varepsilon$-FeOOH displays rich behavior undergoing two transitions: hydrogen bond symmetrization and a high-spin to low-spin transition. The $\varepsilon$-FeOOH phase thus serves as a model system for studying two transitions that are thought to be important in many mantle phases at high pressure. Hydrogen bond symmetrization occurs in a variety of materials at high pressure, including phase H (Tsuchiya and Mookherjee, 2015), phase D (Tsuchiya et al., 2005), and $H_2O$ (Holzapfel, 1972; Aoki et al., 1996; Meier et al., 2018). The high-spin to low-spin transition occurs in a wide variety of ferrous and ferric oxides and silicates (Lin et al., 2005; Tsuchiya et al., 2006; Gleason et al., 2008; Badro, 2014; Liu et al., 2014; Holmström and Stixrude, 2015). A unique feature of $\varepsilon$-FeOOH is that the

two transitions (hydrogen bond symmetrization and high-spin to low-spin transition) are thought to occur at similar pressures, and the nature of possible interaction between these two transitions, i.e. whether one drives the other, is still uncertain (Gleason et al., 2013; Xu et al., 2013; Thompson et al., 2020).

Hydrogen bond symmetrization occurs as the O-O distance of O-H···O decreases, while the O-H bond length increases, leading to a linear symmetric O-H-O configuration and promotion of the space group symmetry to Pnnm. The symmetrization transition has been widely studied in the Al-end member of phase H ($\delta$-AlOOH) (Tsuchiya et al., 2008b; Tsuchiya and Tsuchiya, 2009; Sano-Furukawa et al., 2018) and has been predicted to occur in the MgSi- end-member (Tsuchiya and Mookherjee, 2015; Solomatova et al., 2022). The pressure at which symmetrization occurs in $\varepsilon$-FeOOH is uncertain as neutron diffraction studies have not yet been performed on this phase at high pressure, and previous theoretical studies focused on the symmetrically bonded structure (Thompson et al., 2017).

The high-spin to low-spin transition occurs as increasing crystal field splitting on compression causes d-electrons in the $e_g$ manifold to pair up with those in the $t_{2g}$ manifold, yielding a change in the magnetic moment of the $Fe^{3+}$ cation from 5$\mu$B to 1 $\mu$B, and a collapse in volume. The high-spin to low-spin transition has been found to occur between 40 and 60 GPa in experimental studies (Gleason et al., 2013; Xu et al., 2013; Thompson et al., 2020). The high-spin to low-spin transition in $\varepsilon$-FeOOH has not yet been studied theoretically; part of the reason is that transition metal oxides present a challenge to conventional density functional theory, which tends to underestimate the strong correlation among the d electrons.

Here we explore the behavior of $\varepsilon$-FeOOH at high pressure with density functional theory augmented by local electron repulsion that captures the strong correlation (DFT+U). We study both transitions (hydrogen bond symmetrization and high-spin to low-spin) and explore the changes in properties that occur across them. We focus on physical properties that have been previously measured experimentally in this system, including the structure, equa-

tion of state, and vibrational frequencies, and on those that may be relevant to geophysical detection of phase H in the lower mantle, including elasticity, and electronic properties.

## 6.2 Methods

Our calculations are based on density functional theory (DFT), using the projector augmented wave (PAW) method (Kresse and Joubert, 1999) as implemented in the Vienna *ab initio* Simulation Package (VASP) (Kresse and Furthmüller, 1996). We use the PBEsol generalized gradient approximation (Perdew et al., 2008), which we have previously shown to yield excellent agreement with experiment in iron-bearing oxides (Holmström and Stixrude, 2015). To account for strong correlation, we use the +U method (Anisimov et al., 1997). On the basis of our calculations of the dependence of the spin transition pressure and optical properties on U-J, our previous results for the value of U-J for divalent iron (Holmström and Stixrude, 2015), and expected trends with respect to iron valence state (Mosey et al., 2008), we settled on a value of U-J = 3.2 eV. We use PAW potentials of 14, 1, and 6 valence electrons for Fe, H, and O with core radii of 1.16, 0.37, and 0.82, respectively. We perform spin-polarized simulations where the difference in the number of up-spin and down-spin electrons on each Fe atom is set to the high-spin (5) or low-spin (1) value for both anti-ferromagnetic and ferromagnetic arrangements (Fig. 1a and Fig. 1b). We also explored a mixed-spin arrangement in which half of the Fe are high-spin and the other half are low-spin (Fig. 1c). We found that sampling the Brillouin zone using a 4 x 4 x 4 k-point mesh and a basis-set energy cutoff of 1000 eV was sufficient to converge energy and pressure to within 3 meV/atom and 0.1 GPa, respectively. For calculation of the electronic density of states we use the tetrahedron method (Blochl et al., 1994) and a 20 x 20 x 20 k-point mesh. For phonon calculations, we use a 2 x 2 x 2 supercell and a 2 x 2 x 2 k-point mesh.

We calculate the elastic constants by applying finite strains $\varepsilon_{kl}$ to the lattice and computing the resultant stresses $\sigma_{ij}$, yielding the components of the elastic constant tensor as $\sigma_{ij} =$

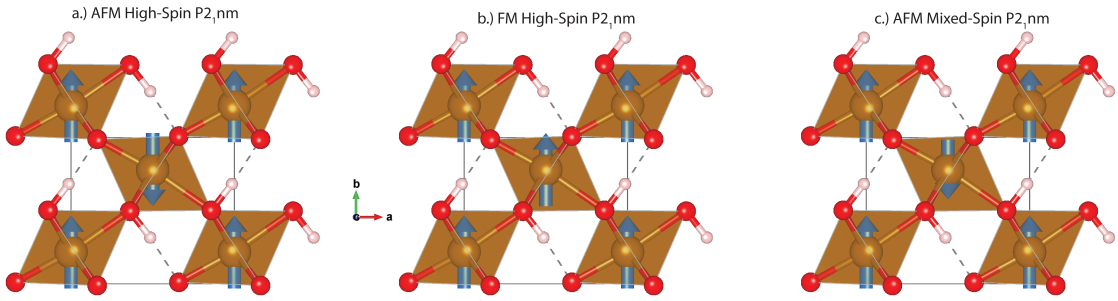


**Figure 6.1:** The structure of the $P2_1nm$ $\varepsilon$-FeOOH phase in an (a) AFM HS state, (b) FM HS state, and (c) an AFM mixed-spin state. The solid black lines indicate unit cells, oxygen atoms are red spheres, hydrogen atoms are pink spheres, and iron atoms are gold spheres. Blue arrows represent the magnetic moment $\mu$ of the iron atoms. The arrow magnitude is related to the spin state (longer = high-spin; shorter = low-spin) and the arrow direction is related to the up/down-spin of valence electrons (up = $+\mu$; down = $-\mu$). Image generated using the software VESTA (Momma and Izumi, 2008)

$c_{ijkl}\varepsilon_{kl}$. We choose a strain magnitude of 0.005 and strains (in Voigt notation): $\varepsilon_1$, $\varepsilon_2$, $\varepsilon_3$, and $\varepsilon_4 + \varepsilon_5 + \varepsilon_6$ appropriate for the orthorhombic case (Le Page and Saxe, 2002). The isotropic bulk and shear moduli are determined using the Voigt-Reuss-Hill (Hill, 1952) measure. We compute single crystal elastic wave velocities via the Christoffel equation $\|c_{ijkl}\, \boldsymbol{n_j n_l} - \rho v^2 \delta_{ik}\| = 0$ where $c_{ijkl}$ is the single-crystal elastic tensor, $\boldsymbol{n}$ is the propagation direction, $\rho$ is the density, $v$ is the velocity, and $\delta_{ik}$ is the Kronecker delta (Musgrave, 1970). The eigenvalues yield the elastic wave velocities, and eigenvectors the polarization directions. We fit our theoretical results to the Eulerian finite strain expansion (Stixrude and Lithgow-Bertelloni, 2005):

$$c_{ijkl} = (1+2f)^{5/2}\Big\{c_{ijkl0} + (3K_0 c'_{ijkl0} - 5c_{ijkl0})f + \left[6K_0 c'_{ijkl0} - 14c_{ijkl0} - \frac{3}{2}K_0\delta^{ij}_{kl} - 16\right]f^2\Big\} \tag{6.1}$$

where $f = 1/2\ [(V/V_0)^{-2/3}-1]$, $c_{ijkl}$ is the elastic tensor, the subscript 0 refers to the reference state (P = 0 GPa, $T_0$ = 300 K), and $\delta^{ij}_{kl} = -\delta_{ij}\delta_{kl} - \delta_{il}\delta_{jk} - \delta_{jl}\delta_{ik}$.

We calculate the phonon vibrational frequencies via density functional perturbation theory (DFPT) (Gajdoš et al., 2006). Phonon frequencies and eigenvectors are computed in the harmonic limit from the second-order force constant matrix $\Phi_{\alpha\beta}(jl,j'l')$, the elements of which are the change in the force in the $\alpha$ Cartesian direction acting on atom $j$ in unit cell $l$, in response to the displacement of atom $j'$ in unit cell $l'$ in the $\beta$ direction (Wilson et al., 1980). The phonon frequencies are the eigenvalues of the dynamical matrix at a given wavevector $\boldsymbol{q}$:

$$D^{jj'}_{\alpha\beta}(\mathbf{q}) = \frac{1}{\sqrt{m_j m_{j'}}} \sum_{l'} \Phi_{\alpha\beta}(jl, jl') \exp[i\mathbf{q} \cdot (\mathbf{r}(j', l') - \mathbf{r}(j, l))] \tag{6.2}$$

where $m_j$ are the atomic masses and $l$ and $l'$ are the unit cells of the two atoms.

The long-ranged Coulomb interactions lead to non-analytic corrections in the limit $\boldsymbol{q} \to 0$, that cause splitting of longitudinal optic (LO) and transverse optic (TO) modes (Pick et al., 1970; Gonze and Lee, 1997):

$$D^{jj'}_{\alpha\beta}(\mathbf{q} \to 0) = D^{jj'}_{\alpha\beta}(\mathbf{q} = \mathbf{0}) + \frac{1}{\sqrt{m_j m_{j'}}} \frac{4\pi}{\Omega_0} \frac{\left[\sum_\gamma q_\gamma Z^j_{\gamma\alpha}\right] \left[\sum_{\gamma'} q_{\gamma'} Z^{j'}_{\gamma'\beta}\right]}{\sum_{\alpha\beta} q_\alpha \varepsilon^\infty_{\alpha\beta} q_\beta} \tag{6.3}$$

where $Z_{\alpha\beta}{}^{j}$ is the Born effective tensor, $\varepsilon^\infty$ is the macroscopic dielectric tensor, and $\Omega_0$ is the volume of the cell.

We compute infrared (IR) intensities from the eigen-displacements around the gamma-point, where the atom's change in polarizability with respect to atomic displacement is captured by the Born effective-charge tensors (Giannozzi and Baroni, 1994):

$$I_{IR}(s) = \sum_\alpha \left| \sum_{j\beta} Z^j_{\alpha\beta} \frac{\mathbf{W}(s, j)}{\sqrt{m_j}} \right|^2 \tag{6.4}$$

where ***W**(s,j)* is the eigenvector of the dynamical matrix corresponding to mode s.

We compute Raman intensities from the change in the polarizability tensor $\alpha$ along the mode eigenvectors in terms of the macroscopic high-frequency dielectric constant (Skelton et al., 2017), via a central finite-difference scheme:

$$I_{Raman} \propto \frac{\partial \alpha}{\partial Q(s)} \equiv \frac{\partial \varepsilon^{\infty}}{\partial Q(s)} \approx \frac{\Delta \varepsilon^{\infty}}{\Delta Q(s)} \tag{6.5}$$

$$I_{Raman,\alpha\beta}(s) = \frac{\Omega}{4\pi}\left[-\frac{1}{2}\frac{\varepsilon^{\infty}_{\alpha\beta}(-s)}{\Delta Q(s)} + \frac{1}{2}\frac{\varepsilon^{\infty}_{\alpha\beta}(+s)}{\Delta Q(s)}\right] \tag{6.6}$$

where $Q$ is the normal-mode coordinate at the Γ-point and is defined by *u(s,j) = Q(s)* $\boldsymbol{W}$*(s,j)*$/\sqrt{m_j}$, where *u(s,j)* is the atomic displacement. The unpolarized Raman intensity takes the form:

$$\begin{aligned} I_{Raman} = 45 &\left[\frac{1}{3}(I_{xx} + I_{yy} + I_{zz}\right]^2 + \\ &\frac{7}{2}\left[(I_{xx} - I_{yy})^2 + (I_{xx} - I_{zz})^2 + (I_{yy} - I_{zz})^2 + 6(I_{xy}^2 + I_{xz}^2 + I_{yz}^2)\right]. \end{aligned} \tag{6.7}$$

To compute phonon frequencies and IR and Raman intensities, we use Phonopy and Phonopy-Spectroscopy (Togo and Tanaka, 2015; Skelton et al., 2017).

We find the pressure of the high-spin to low-spin transition as the point at which the Gibbs free energies of the two phases are equal:

$$G(P,T) = H(P, static) + F_{TH}(V,T) + P(V,T)V, \tag{6.8}$$

where $H$ is the enthalpy at static (athermal) conditions, $G$ is the Gibbs free energy as a function of pressure $P$ and temperature $T$, $V$ is the volume, and $F_{TH}$ is the Helmholtz free energy derived from the (quasi-)harmonic phonon energy. The pressure

$$P(V,T) = P(V,static) + P_{TH}(V,T) \tag{6.9}$$

where $P_{TH}$ = -$(\partial F_{TH}/\partial V)_T$ and

$$F_{TH} = \frac{1}{2}\sum_{\mathbf{q}j} \hbar\omega_{\mathbf{q}j} + k_B T \sum_{\mathbf{q}j} \ln\left[1 - \exp\left(-\frac{\hbar\omega_{\mathbf{q}j}}{k_B T}\right)\right] \tag{6.10}$$

where $\omega$ is the phonon frequency. We have found that the thermal free energy of the asymmetrically bonded phase is nearly independent of volume, yielding essentially zero thermal pressure. This result is inconsistent with experimental measurements of positive thermal expansivity (Suzuki, 2016), indicating that anharmonicity, which is not included at our level of theory, is important in the asymmetric phase. We hypothesize that the thermal free energy of the asymmetric phase can be approximated by that of the symmetric phase at the same volume. Our hypothesis could be tested by performing molecular dynamics simulations, which are beyond the scope of this study because of the much greater computational cost.

## 6.3 Results

At static conditions, we find that the ground state is high-spin anti-ferromagnetic (AFM), in agreement with a neutron diffraction study at ambient pressure (Pernet et al., 1975) (Fig. 6.2). The AFM state is more stable than the ferromagnetic (FM) state by 0.5 eV per unit cell (0.25 eV /formula unit) at zero pressure and 0.8 eV at 40 GPa. At 40 GPa, the lowest energy state becomes low-spin AFM. In the low-spin state, AFM is more stable than FM by 0.02 eV at 40 GPa, to 0.01 eV at 100 GPa. We also find that the mixed-spin state is less stable than the high-spin state at 40 GPa by 0.4 eV. Because AFM is the most stable, all subsequent results refer to the AFM arrangement.

We find hydrogen bond symmetrization to occur within the stability field of the high-spin state (Fig. 6.3). The transition occurs at a static pressure of 34 GPa. The symmetrization

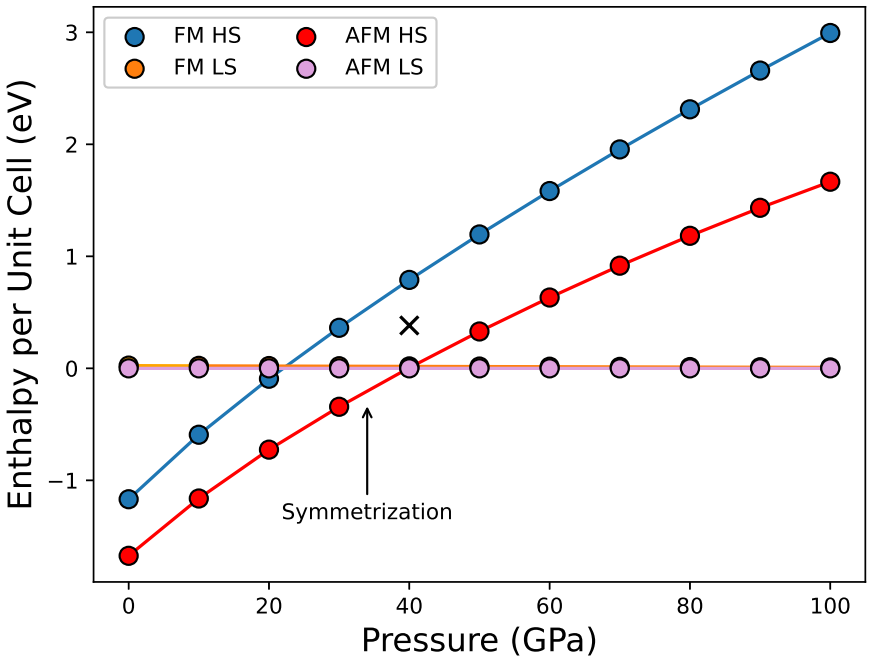


**Figure 6.2:** Enthalpy of FM and AFM states at static condition with respect to the AFM low-spin enthalpy. The arrow marks the pressure at which hydrogen bond symmetrization occurs, and x marks the AFM mixed spin enthalpy.

transition occurs without discontinuity in structure or volume and is therefore not first order. We also show results for the (metastable) symmetrization transition in the low spin state, which occurs at a static pressure of 5 GPa.

We find excellent agreement with experimental measurements of the equation of state of the high-spin and low-spin states and the pressure of the high-spin to low-spin transition (Suzuki, 2010, 2016; Gleason et al., 2013; Ikeda et al., 2019; Thompson et al., 2020) (Fig. 4). We find that the high-spin to low-spin transition occurs at 45 GPa at 300 K. We find disagreement with some previous experiments, including those of Gleason et al. (2013), at pressures greater than 50 GPa, which may be due to the lack of a pressure medium in this experiment, resulting in deviatoric stress and systematic overestimation of volumes (Meng

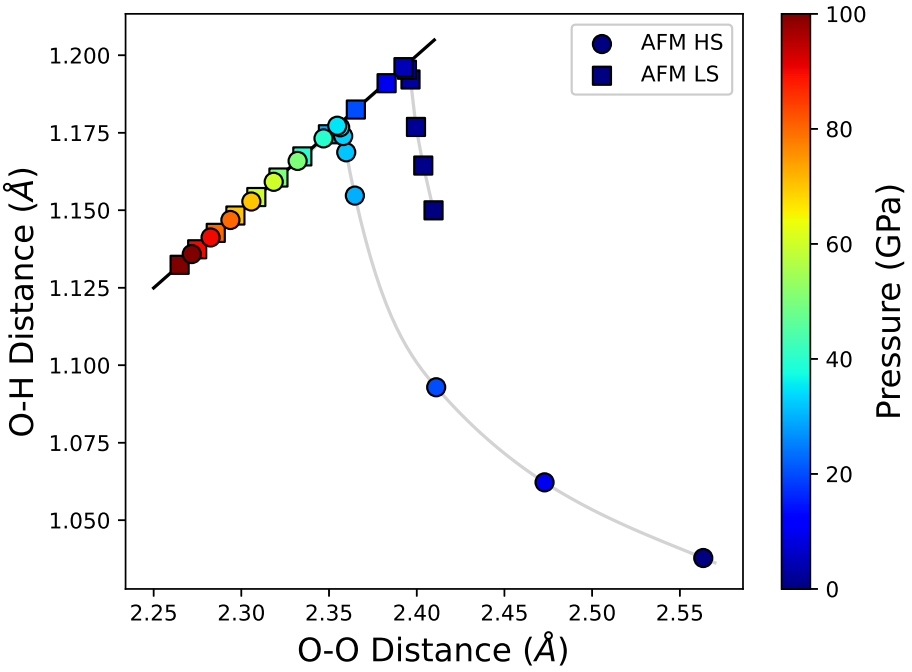


**Figure 6.3:** O-H vs O-O bond distance in high-spin (circles) and low-spin (squares) states with pressure indicated by the color bar. The 2:1 line is shown in black.

et al., 1993). The symmetrization transition has only a subtle effect on the equation of state: the symmetric and asymmetric equations of state are nearly coincident within the symmetric high spin stability field and there is no discontinuity in volume at the symmetrization transition. At 300 K, the symmetrization transition occurs at 37 GPa. All subsequent results are referred to the pressure at 300 K.

Our computed crystal structures agree well with ambient structure determinations and with high pressure measurements of the lattice parameters (Fig. 6.5, Table 1). We find a change in relative axial compressibilities with increasing pressure: $b$ is the most compressible direction near ambient pressure, but the stiffest at pressures exceeding 30 GPa. This change in relative compressibility is reflected in extrema in the variation of lattice parameter ratios versus pressure, which occur at 13 GPa ($b/c$) and 33 GPa ($a/b$). The largest deviation

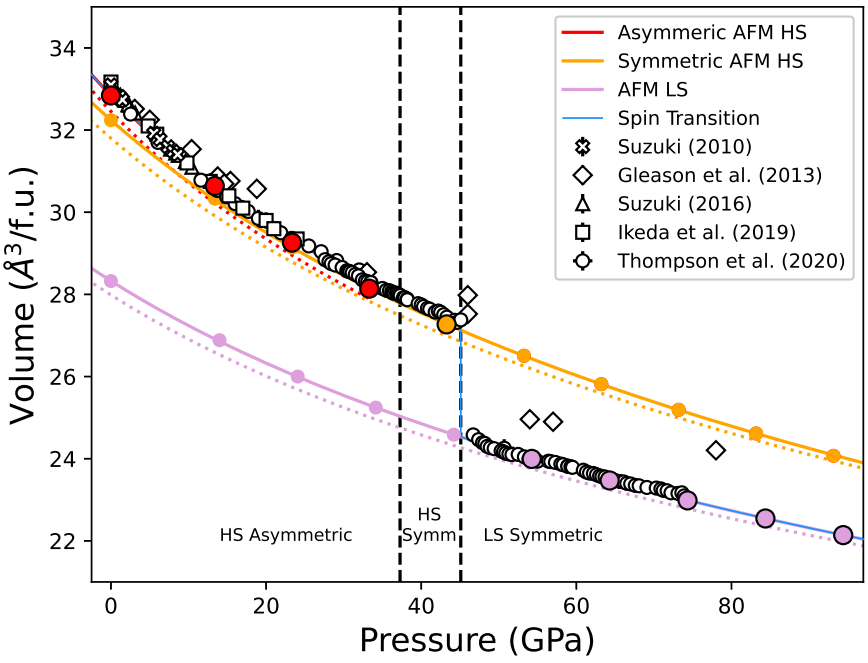


**Figure 6.4:** Pressure-volume equation of state for static and 300 K isotherms. Symbols in red, orange, and plum represent the asymmetric high-spin phase, the symmetric high-spin phase, and the symmetric low-spin phase at 300 K conditions. Dashed lines and solid lines represent the static and 300 K equations of state for each respective color. The blue line follows the stable phases. The vertical black dashed lines represent the hydrogen bond symmetrization and spin transition at 37 GPa and 45 GPa, respectively, at 300 K. Equation of state fit parameters $V_0$, $K_0$, and $K'_0$ are 65.68 Å$^3$, 168.55 ± 0.30 GPa, and 3.72 ± 0.01 for asymmetric high-spin, 64.48 Å$^3$, 193.42 ± 0.43 GPa, and 3.51 ± 0.02 for symmetric high-spin, and 56.65 Å$^3$, 236.56 ± 0.42 GPa, and 3.91 ± 0.01 for the symmetric low-spin at 300 K.

in atomic coordinates between our results and experiment occurs for the position of the H atom, corresponding to an OH bond length of 1.02 Åfor our results as compared with 0.85 Åfor experiment (Bolotina et al., 2008). Overestimation of OH bond length is expected at

our level of theory (Santra et al., 2009).

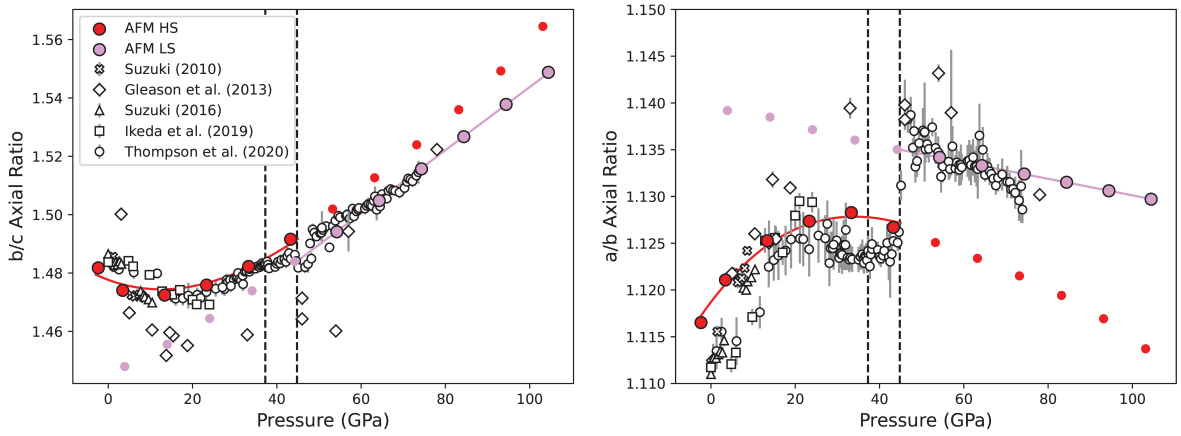


**Figure 6.5:** Lattice parameter ratios with respect to pressure. Red and plum represents the AFM high-spin and AFM low-spin states, respectively, and are compared to experimental results (white symbols). The vertical dashed lines represent the predicted 300 K pressure of the symmetrization transition (lower pressure) and the high-spin to low-spin transition (higher pressure).

The elastic moduli change discontinuously at the high-spin to low-spin transition and continuously at the symmetrization transition (Fig. 6.6). Because the hydrogen bonds lie within the $xy$-plane, the difference between asymmetric and symmetric structures is reflected more strongly in $c_{11}$ and $c_{22}$ than in $c_{33}$, and more strongly in $c_{66}$ than in $c_{44}$ or $c_{55}$. Values of $c_{ijkl0}$ and $c'_{ijkl0}$ show that the elastic moduli are softer and vary more rapidly with pressure in the asymmetric state as compared with the symmetric state: while the elastic moduli of the asymmetric and symmetric states become identical at the symmetrization transition, the pressure-dependence of the elastic moduli changes discontinuously at the transition. The elastic moduli are all stiffer in the low-spin state as compared with the high-spin state (Table 2). The $c_{44}$ and $c_{55}$ elastic moduli show a non-monotonic pressure dependence.

The bulk and shear moduli increase monotonically with increasing pressure from 0 to 90 GPa and both undergo an increase of 18% at the spin transition (Fig. 6.7). In the

[a](Bolotina et al., 2008). Fe(x) = Fe(z) = H(z) = O1(z) = O2(z) = 0

| Pressure (static) | Pressure (300 K) | $a$ (Å) | $b$ (Å) | $c$ (Å) | Fe (y) | H (x) | H (y) | O1 (x) | O1 (y) | O2 (x) | O2 (y) |
|---|---|---|---|---|---|---|---|---|---|---|---|
| | | | | | $\boldsymbol{P2_1nm}$ | | | | | | |
| | 0[a] | 4.958 | 4.461 | 3.005 | 0.219 | 0.46 | 0.35 | 0.352 | 0.497 | 0.658 | 0.005 |
| -5.88 | -2.36 | 5.005 | 4.483 | 3.025 | 0.223 | 0.485 | 0.317 | 0.359 | 0.497 | 0.660 | 0.011 |
| 0 | 3.44 | 4.936 | 4.403 | 2.987 | 0.227 | 0.486 | 0.303 | 0.357 | 0.490 | 0.656 | 0.014 |
| 10 | 13.38 | 4.852 | 4.312 | 2.929 | 0.234 | 0.488 | 0.288 | 0.356 | 0.484 | 0.653 | 0.018 |
| 20 | 23.34 | 4.788 | 4.247 | 2.878 | 0.240 | 0.492 | 0.275 | 0.355 | 0.480 | 0.651 | 0.021 |
| 30 | 33.30 | 4.736 | 4.197 | 2.832 | 0.248 | 0.498 | 0.258 | 0.353 | 0.478 | 0.649 | 0.024 |
| | | | | | $\boldsymbol{Pnnm}$ | | | | | | |
| 40 | 44.19 | 4.692 | 4.164 | 2.792 | 0.25 | 0.5 | 0.25 | 0.351 | 0.476 | 0.648 | 0.024 |
| 50 | 52.24 | 4.518 | 3.983 | 2.666 | 0.25 | 0.5 | 0.25 | 0.348 | 0.485 | 0.651 | 0.015 |
| 60 | 64.29 | 4.493 | 3.965 | 2.635 | 0.25 | 0.5 | 0.25 | 0.347 | 0.484 | 0.652 | 0.016 |
| 70 | 74.33 | 4.471 | 3.948 | 2.605 | 0.25 | 0.5 | 0.25 | 0.347 | 0.483 | 0.653 | 0.017 |
| 80 | 84.37 | 4.450 | 3.933 | 2.576 | 0.25 | 0.5 | 0.25 | 0.346 | 0.483 | 0.654 | 0.017 |
| 90 | 94.41 | 4.432 | 3.920 | 2.549 | 0.25 | 0.5 | 0.25 | 0.345 | 0.482 | 0.654 | 0.018 |
| 100 | 104.44 | 4.414 8 | 3.908 | 2.523 | 0.25 | 0.5 | 0.25 | 0.345 | 0.481 | 0.655 | 0.019 |

**Table 6.1:** Crystal structures of the $P2_1nm$ and $Pnnm$ phase with respect to pressure.

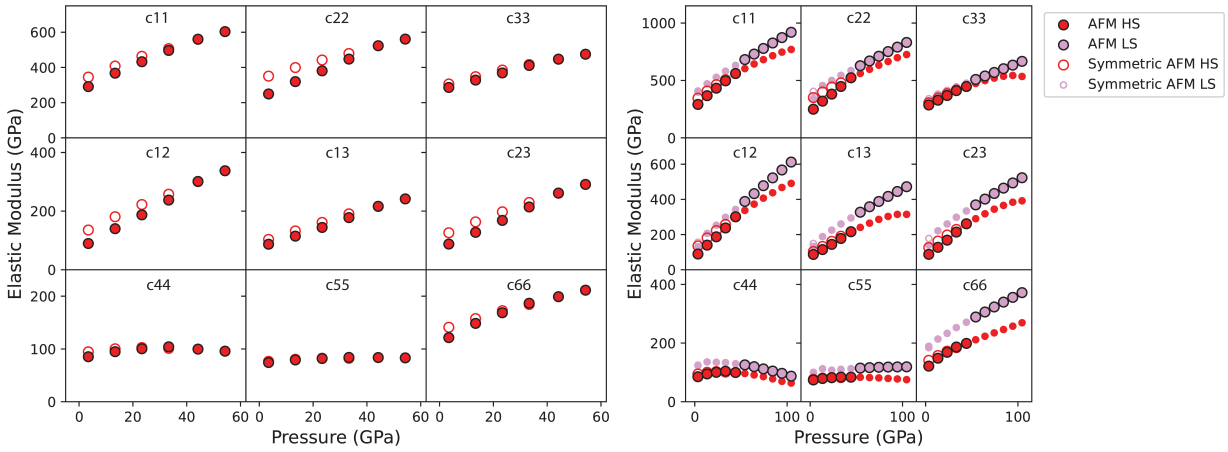


**Figure 6.6:** Elastic modulus with respect to pressure. Red and plum represent the AFM high-spin and AFM low-spin states, where closed and open symbols represent the asymmetric and symmetric states, respectively. Symbols representing stable phases are outlined in black.

low spin state, the shear modulus is nearly independent of pressure, reflecting, in part, the non-monotonic dependence of $c_{44}$ and $c_{55}$ on pressure, while $c_{66}$ increases with increasing pressure. Our elastic constants for the low spin state are in good agreement with previous calculations (Thompson et al., 2017) with differences (<7%) reflecting the difference in exchange-correlation functional used in the two studies (PBE vs. PBEsol in our study). We find that $\varepsilon$-FeOOH is highly anisotropic in both longitudinal- and shear-wave velocities at all pressures, with the shear wave velocity varying with propagation and polarization direction by as much as 24% at zero pressure and 43% at 46 GPa.

| | $c_{11}$ | $c_{12}$ | $c_{13}$ | $c_{22}$ | $c_{23}$ | $c_{33}$ | $c_{44}$ | $c_{55}$ | $c_{66}$ |
|---|---|---|---|---|---|---|---|---|---|
| Asymmetric HS | 280(4) | 78(5) | 76(4) | 234(6) | 77(4) | 272(3) | 88(3) | 73(1) | 121(2) |
| Symmetric HS | 333(3) | 128(2) | 97(1) | 335(2) | 120(2) | 295(1) | 95(1) | 74(1) | 135(1) |
| Symmetric LS | 392(7) | 147(1) | 148(3) | 384(2) | 177(3) | 319(3) | 134(2) | 99(2) | 183(1) |
| | $c'_{11}$ | $c'_{12}$ | $c'_{13}$ | $c'_{22}$ | $c'_{23}$ | $c'_{33}$ | $c'_{44}$ | $c'_{55}$ | $c'_{66}$ |
| Asymmetric HS | 6.65(8) | 4.5(1) | 3.01(8) | 6.6(1) | 3.83(8) | 4.64(6) | 0.67(6) | 0.59(1) | 2.06(5) |
| Symmetric HS | 5.75(6) | 3.85(5) | 2.74(2) | 4.99(5) | 3.23(4) | 4.19(2) | 0.48(2) | 0.51(1) | 1.74(2) |
| Symmetric LS | 5.92(1) | 4.34(1) | 3.27(3) | 5.22(2) | 3.53(4) | 4.20(4) | 0.24(3) | 0.62(2) | 2.24(2) |

**Table 6.2:** Elastic moduli $c_{ijkl0}$ and $c'_{ijkl0}$ with reference state of P = 0 GPa and T = 300 K.

The evolution of the hydrogen bond on compression is clearly reflected in the vibrational frequencies (Fig. 6.8). The frequencies of the $A_1$ and $B_2$ OH stretching modes decrease rapidly with pressure and the bending modes increase more gradually with pressure so that the frequencies of these two branches approach each other. In the symmetrically-bonded phase the OH stretching mode frequencies increase with increasing pressure while the bending mode frequencies initially continue to increase slightly with increasing pressure. These trends are also seen in $\delta$-AlOOH (Tsuchiya et al., 2008b). The OH stretching and bending mode frequencies change little at the high-spin to low-spin transition; in the low spin state some of the bending mode frequencies decrease with increasing pressure. Agreement is ex-

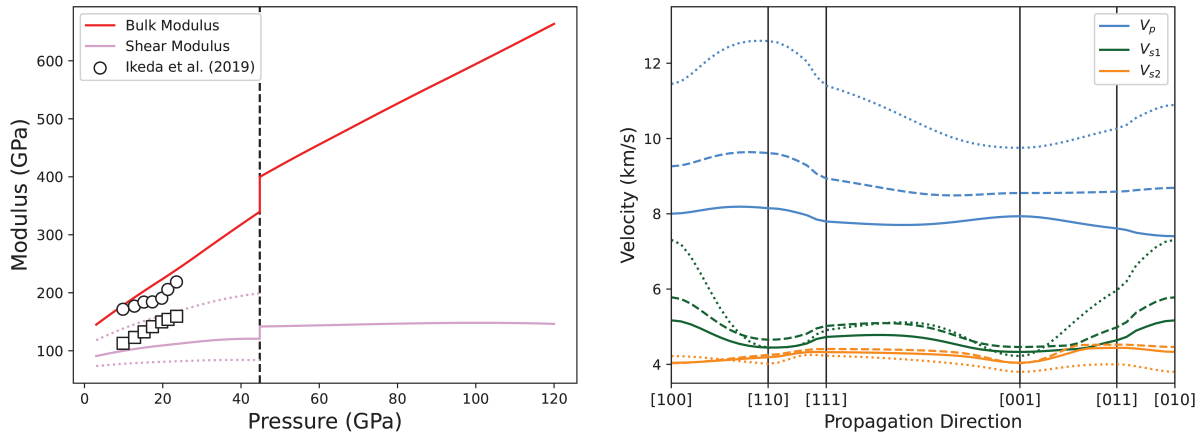


**Figure 6.7:** Left: Elastic properties of $\varepsilon$-FeOOH with respect to pressure compared with experimental measurements from Ikeda et al. (2019) (white circles and squares correspond to bulk and shear modulus, respectively). Dotted plum lines are maximum and minimum values of shear modulus from single crystal wave velocities from our results. Right: $v_p$ and $v_s$ dependence on propagation direction at 3.4 GPa (solid), 23.3 GPa (dashed), and 94.4 GPa (dotted).

cellent between our bending mode frequencies and experiment (Thompson et al., 2020) and our stretching mode frequencies are 1.4% smaller than the positions of peaks apparent in the experimentally reported spectrum in the OH stretching region at ambient conditions. Underestimation of OH stretching frequencies is expected at our level of theory (Santra et al., 2009).

The predicted absolute intensities of the IR- and Raman-active modes show large changes in the vibrational spectra with increasing pressure (Fig. 9). Factor group analysis for the $P2_1nm$ and Pnnm structure shows that the irreducible representation of the zone center optic vibrations are $\Gamma_{P2_1nm} = 7A_1(IR,R) + 4A_2(R) + 3B_1(IR,R) + 7\ B_2(IR,R)$ and $\Gamma_{Pnnm} = 2B_{1u}(IR) + 5B_{2u}(IR) + 5B_3u\ (IR) + 3A_u + 2A_g(R) + 2B_{1g}(R) + 1B_{2g}(R) + 1B_{3g}(R)$, where IR and R denote infrared and Raman active modes. In the IR spectrum, the highest frequency peak initially increases in intensity with increasing pressure, then splits as

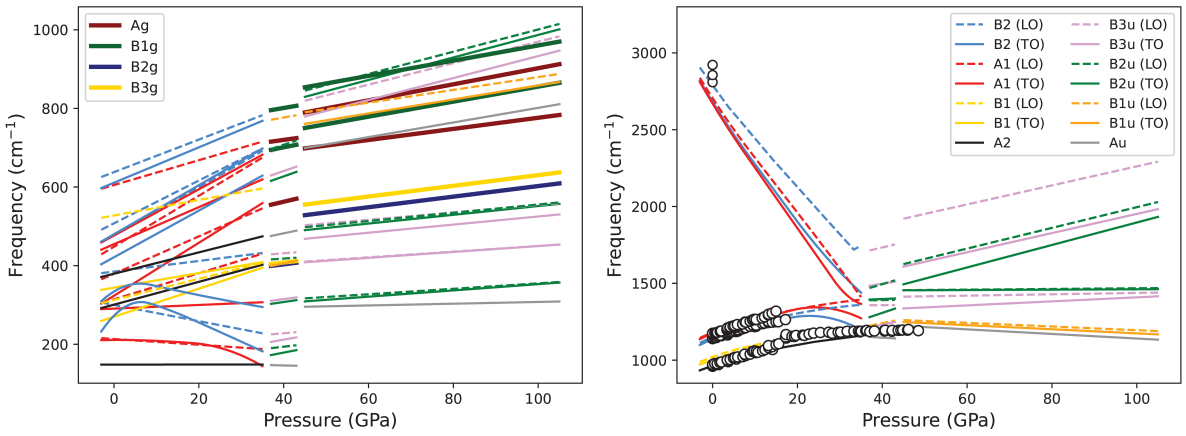


**Figure 6.8:** Pressure dependence of optical mode frequencies compared to experimental data in white circles (Thompson et al., 2020).

symmetrization is approached. At a pressure that nearly coincides with symmetrization (33 GPa), the most intense peaks are no longer the highest frequency peaks, reflecting mixing of stretching and bending modes. In the low-spin state, the peak at the highest frequency become the one with the highest intensity again. The Raman spectrum also shows splitting of the OH highest frequency as symmetrization is approached, as well as a vanishing intensity. This decrease in intensity is expected on symmetry grounds, and is also seen, for example, in $H_2O$ (Goncharov et al., 1999).

The electronic density of states shows a finite band gap at all pressures in high-spin and low-spin states (Fig. 6.10). The band gap decreases with increasing pressure in both phases and increases by 0.15 eV at the high-spin to low-spin transition. The band gap is narrow and comparable to that typically seen in semiconductors: 1.9 eV at ambient pressure and 1.3 eV at the highest pressure explored in this study. Consideration of +U in our study is crucial to obtaining agreement with experiment: if we assume that U-J=0 eV, we find that there is no band gap at any pressure.

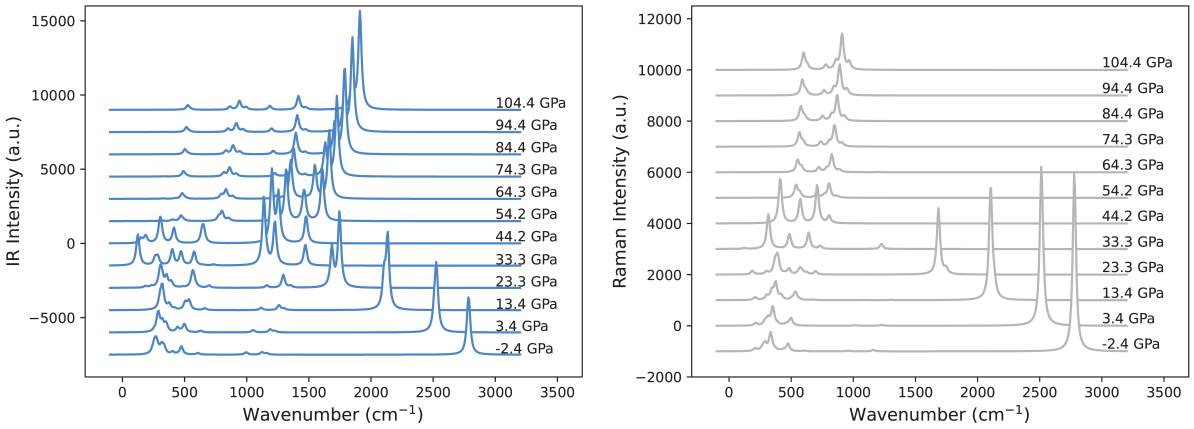


**Figure 6.9:** Computed IR intensities (left) and Raman intensities (right) with respect to pressure.

## 6.4 Discussion

We find two distinct phase transitions: the symmetrization transition and the high-spin to low-spin transition, which do not coincide, but are well separated in pressure, with the high spin symmetric phase stable over a finite pressure interval (8 GPa). Our results therefore do not support the arguments of some earlier studies that symmetrization drives the high-spin to low-spin transition (Gleason et al., 2013).

Our value for the pressure of the symmetrization transition (37 GPa), is much higher than the value of 18 GPa, argued for by Thompson et al. (2020). However, Thompson et al. (2020) were not able to measure hydrogen positions and relied on other lines of evidence to argue for the pressure of symmetrization. These included the location of inflection points in the variation of lattice parameter ratios with pressure. However, we do not see inflection points but instead find local extrema (a local minimum in $b/c$ at 13 GPa, and a local maximum in $a/b$ at 33 GPa) neither of which correspond precisely with the pressure of hydrogen bond symmetrization. We find that the lattice parameters begin to vary nearly linearly with pressure at the symmetrization transition, behavior also seen in a previous

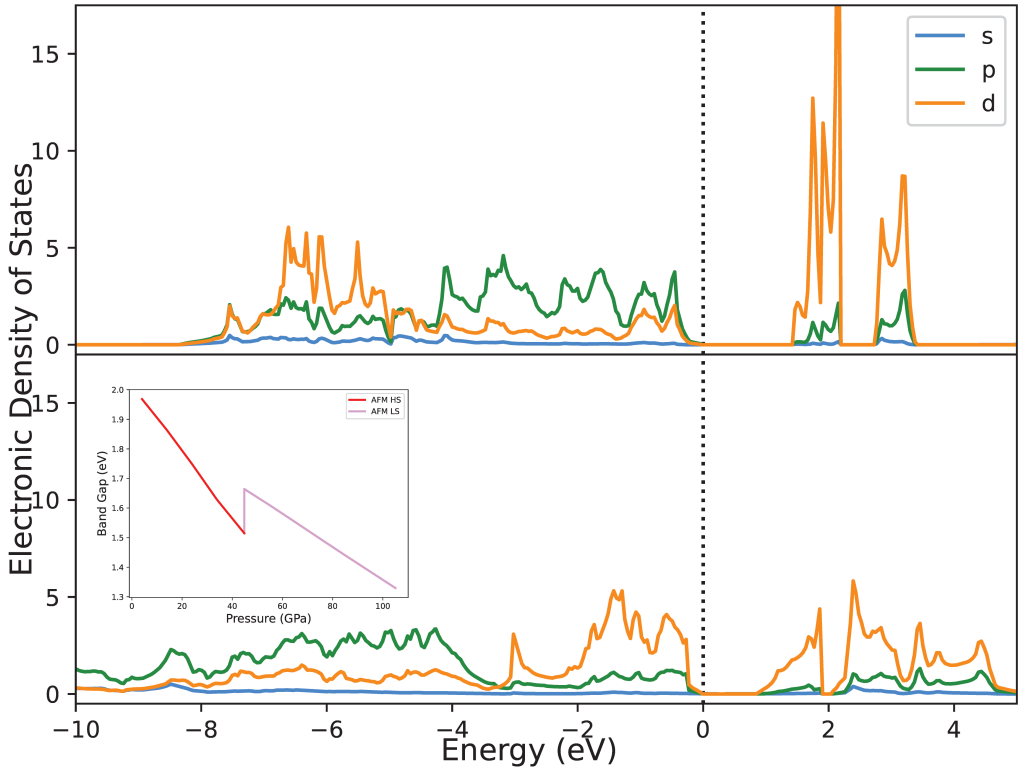


**Figure 6.10:** Electronic density of states at 3.4 GPa (top) and 94 GPa (bottom) with respect to s, p, and d orbitals. Inset shows the band gap dependence on pressure.

theoretical study of $\delta$-AlOOH (Tsuchiya and Tsuchiya, 2009).

The asymmetric to symmetric transition is continuous. The volume and bulk modulus (and all the elastic moduli) are continuous across the transition, so the transition is neither first order nor second order. Elastic wave velocities are also continuous across the symmetrization transition, so that no seismological signature of the symmetrization transition is expected. Our computed vibrational spectra indicate that symmetrization might be detected via IR or Raman spectroscopy: according to our results, the symmetrization transition is characterized by changes in the pressure dependence of several modes, as well as splitting, and changes in intensity. Neutron diffraction of deuterated samples, as recently done for AlOOH (Sano-Furukawa et al., 2018), could also lend further insight into symmetrization in

$\varepsilon$-FeOOH.

Our predictions of the shear and bulk modulus of $\varepsilon$-FeOOH do not agree with the experimental measurements of Ikeda et al. (2019). The contrast in the pressure dependence of the shear modulus (G'=dG/dP) is particularly notable (G'=1.2 from our results vs. G'=4.6 from experiment). The reason for this discrepancy is unclear. It is possible that approximations to the exchange-correlation functional in our study are the cause of the discrepancy, but this seems unlikely, because previous studies have found good agreement between density functional theory and experiment for the elastic moduli of $\delta$-AlOOH (Tsuchiya and Tsuchiya, 2009). The value of G' found for $\delta$-AlOOH (1.33) is very similar to what we find for $\varepsilon$-FeOOH. Another possibility is that the experimental sample is textured or that the degree of texture of the sample varied with increasing pressure. Texturing of the sample could change the shear modulus substantially because $\varepsilon$-FeOOH is very anisotropic, with the shear modulus varying by 24% to 43% with propagation and polarization direction at 0 and 43 GPa, respectively. $\varepsilon$-FeOOH is much more anisotropic than $\delta$-AlOOH (Tsuchiya and Tsuchiya, 2009).

The high spin state is likely to be remain magnetically ordered at room temperature throughout its stability field. This conclusion is based on the large enthalpy difference that we find between AFM and FM ordering. The enthalpy difference grows with increasing pressure and is similar in magnitude to the difference between the AFM and FM ordering states of hematite (0.25 eV/Fe; (Rollmann et al., 2004)), which has a Neel temperature of 950 K. We would therefore expect $\varepsilon$-FeOOH to have a Neel temperature of similar magnitude based on our results, in agreement with neutron diffraction experiments that show that AFM ordering exists in $\varepsilon$-FeOOH to at least 423 K (Pernet et al., 1975) and an estimated Neel temperature of 570 K (Pernet et al., 1973). The low spin state is likely to be magnetically disordered at room temperature, as the difference in energy between AFM and FM ordering is much smaller than in the high spin state (by a factor of  25).

Our results suggest possible explanations for the sharpness of the high-spin to low-spin

transition as seen experimentally. The experiments of Thompson et al. (2020), show that the transition interval is irresolvably sharp and no greater than 2 GPa. This is much less than the width of the high-spin to low-spin transition at room temperature seen in other systems: for example, 10 GPa in $MgSiO_3$-$Fe_2O_3$ (Liu et al., 2018), or 18 GPa in $Mg_{0.5}Fe_{0.5O}$ (Solomatova et al., 2016). We hypothesize that the width of the high spin to low spin transition in $\varepsilon$-FeOOH is limited by two factors. First is the presence of non-ideal interactions between high-spin and low-spin Fe cations. We find that the mixed-spin state is much higher in energy than the high-spin or low-spin states. This unfavorable energy of interaction is not included in the widely used ideal model of the spin transition (Tsuchiya et al., 2006) and has the effect of limiting the pressure interval of coexistence of high-spin and low-spin cations. Second is the presence of magnetic order. The ideal solution model, as typically applied, assumes the high temperature limit of magnetic entropy. But this limit may not be valid in the case of $\varepsilon$-FeOOH because the Neel temperature of the high-spin state is likely to exceed room temperature at all pressures.

Our calculations are quasiharmonic and we are therefore not able explore the possibility of H disorder in $\varepsilon$-FeOOH. Consideration of H disorder is motivated by neutron diffraction experiments on $\delta$-AlOOH, which have been interpreted to show disorder of H between two symmetrically equivalent positions along the O···O line (Sano-Furukawa et al., 2018). On the other hand, another recent study based on static structural relaxations in density functional theory and nuclear magnetic resonance experiments argues against H disorder in $\delta$-AlOOH (Trybel et al., 2021). We suggest that molecular dynamics simulations could be used to explore the possibility of H disorder in $\varepsilon$-FeOOH.

## 6.5 Implications

The presence of $\varepsilon$-FeOOH in Earth's mantle could have significant effects on material properties due to the iron spin-transition and hydrogen bond symmetrization. The shear modulus

shows a large increase at the high-spin to low-spin transition in $\varepsilon$-FeOOH (an 18% increase in shear modulus, or 3% increase in shear wave velocity); behavior that contrasts with other systems. For example, in ferropericlase, the shear modulus is continuous across the high-spin to low-spin transition (Yang et al., 2015; Marquardt et al., 2018). Possible seismic detection of the high-spin to low-spin transition in the mantle has therefore focused on the effect of the transition on the bulk modulus, and therefore the P-wave velocity (or bulk sound velocity) (Shephard et al., 2021). Our results show that the S-wave velocity may also be significantly affected by the spin transition in lower mantle phases other than ferropericlase. The bulk modulus anomaly associated with the high-spin to low-spin transition is caused by the volume collapse across the pressure interval of the transition. We have assumed in the case of $\varepsilon$-FeOOH, that the high-spin to low-spin transition is sharp, consistent with experiment, and therefore does not show any bulk modulus anomaly at room temperature, although it is possible that a narrow transition interval exists over which the bulk modulus anomaly would also exist.

Based on our results, the seismic signature of the spin transition in phase H may be more distinct than that in other systems undergoing spin transitions, including ferropericlase. In ferropericlase, the width of the transition is broader than the ideal case at all temperatures because of favorable interaction between high-spin and low-spin Fe (Holmström and Stixrude, 2015), tending to mute the elastic signature of the transition. The width of the spin transition in $\varepsilon$-FeOOH is likely to increase with temperature. However, the unfavorable interaction between unlike spins in $\varepsilon$-FeOOH is likely to limit the width of the transition as seen in phase H as compared with expectations based on ideal mixing of spin states.

Our prediction of a narrow band gap in $\varepsilon$-FeOOH raises the possibility that phase H may contribute to the electrical conductivity of the lower mantle as seen in electromagnetic sounding (Püthe et al., 2015). The narrow gap that we find is consistent with experimental observations of non-zero infrared transmission at all pressures measured from 23-72 GPa (Thompson et al., 2020). Moreover, the experiments show increasing absorption with in-

creasing pressure, in agreement with the decreasing band gap with increasing pressure that we find. Our results are also consistent with experimental measurements showing that the electrical conductivity increases with increasing pressure and is small in value, typical of semi-conductors (Wang and Yoshino, 2021; Zhuang et al., 2022). On the other hand, the experiments show a rapid drop in transmission and a rapid increase in electrical conductivity at the high-spin to low-spin transition, whereas we find a slight increase in the band gap at the transition. Further study of the relationship between the band structure, optical absorption, and electrical conductivity is therefore warranted.

# CHAPTER 7

# Physical Properties of Pyrite-FeOOH in the Earth's Lower Mantle

## 7.1 Introduction

The amount of hydrogen present and its incorporation in the Earth's deep interior remains unknown despite hydrogen being the most abundant element in the solar system. Hydrogen may be transported to the lower mantle by subduction of cold oceanic plates, in which hydrogen takes the form of hydrous minerals at low pressure. As oceanic slabs descend into the Earth's interior, hydrogen exchange with the surrounding mantle may significantly affect its transport properties, melting temperature, and other physical properties.

An alternative hypothesis for the origin of hydrogen in the Earth's deep mantle is a hydrogen-rich primordial atmosphere (Young et al., 2023). In this view, water in the mantle is a remnant of Earth's formation. Hydrogen derived from the primordial atmosphere could also have a significant influence on the density of the core and the oxidation state of lower mantle materials, thus shaping our understanding of Earth's planetary evolution

A number of experimental and theoretical studies have explored the stability of oxy-hydroxides MOOH to conditions of the lowermost mantle with M=Al, Fe, (Mg,Si). These studies find a phase transition to a pyrite-structured phase at lower mantle coditions, which has been proposed to be a possible carrier and reservoir of water (Tsuchiya et al., 2008b; Thompson et al., 2021; Tsuchiya et al., 2020). The pyrite-structure is known to be stable in $SiO_2$ and $GeO_2$ above 250 GPa and 90 GPa (Kuwayama et al., 2005; Ono et al., 2003),

respectively, and was found to be experimentally stable in GaOOH and InOOH compositions (Tsuchiya et al., 2008a; Sano et al., 2008).

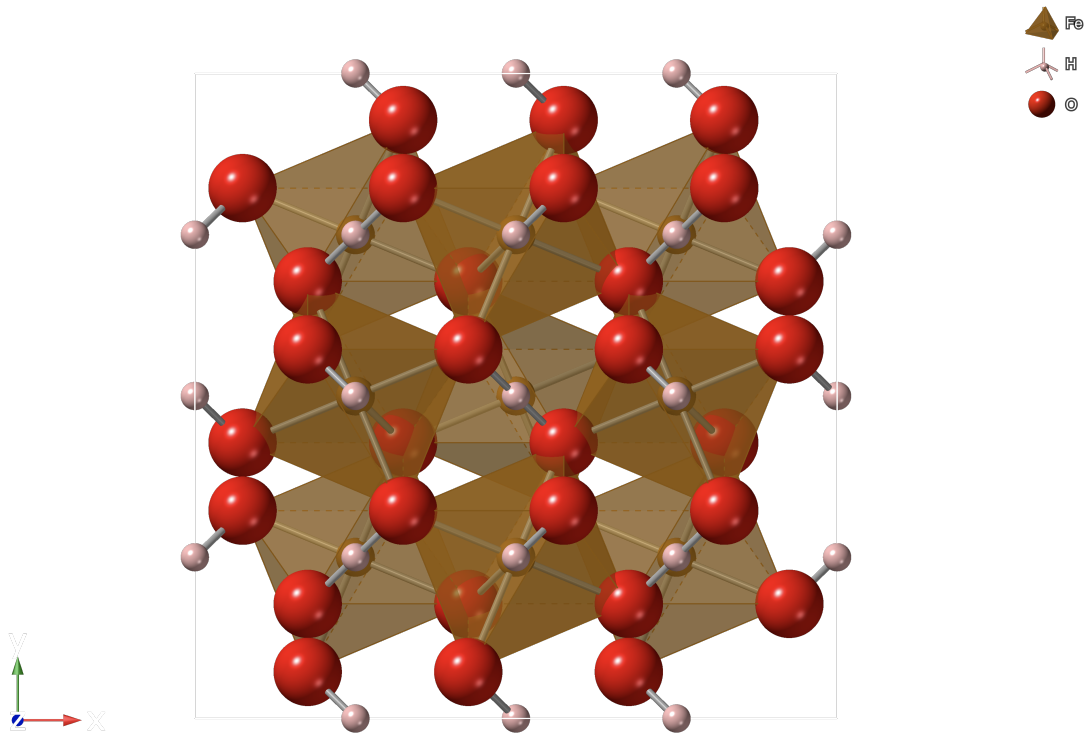


**Figure 7.1:** $Pa\bar{3}$ pyrite-structured FeOOH. Iron atoms are represented by gold spheres, oxygen atoms by red spheres, and hydrogen atoms by pink spheres. The $FeO_6$ octahedra are depicted in transparent gold and bonding by gray bars.

Recent experimental studies (Hu et al., 2017; Hu and Liu, 2021a; Nishi et al., 2017; Mao et al., 2017) report evidence for the stability of pyrite-structured FeOOH in the Earth's lowermost mantle. The stability of this material at high pressures suggests the existence of another possible water carrier, either as a separate phase or in solid solution with other MOOH end-members, and may provide a pathway for investigating the interaction of core material with hydrogen-bearing mantle material at the core-mantle boundary.

Our focus here is the ferric end-member of the pyrite-structured dense-oxyhydroxide:

pyrite-phased FeOOH (p-FeOOH) (Fig. 7.1). P-FeOOH has the pyrite structure with a $Pa\bar{3}$ space group that is stable in the lowermost mantle (Gleason et al., 2013; Nishi et al., 2017; Suzuki, 2010; Hu et al., 2017; Hu and Liu, 2021a), although its stability field is uncertain. The structure is cubic with $FeO_6$ octahedra linked by symmetric hydrogen bonds. The anhydrous sub-lattice (arrangement of Fe and O atoms) is identical to the $FeS_2$ pyrite structure.

P-FeOOH has been proposed to undergo partial dehydrogenation upon its formation from lower pressure polymorphs during subduction (Hu et al., 2016, 2017; Mao et al., 2017) and decompose to form $FeOOH_x+(1-x)/2\ H_2$, with $0 < x < 1$. Hydrogen loss from p-$FeOOH_x$ raises an interesting possibility of the first phase with partial hydrogen occupation in a solid phase, where the hydrogen exchange may alter the valence and spin states of iron atoms with important implications for our understanding of oxygen fugacity and water circulation in the Earth's interior. However, the value of $x$ is poorly constrained experimentally, in part because the H are not visible in typical x-ray diffraction experiments.

Here, we explore the behavior of p-FeOOH at high pressure with density functional theory augmented by local electron-electron repulsion that captures the strong correlation within the 3d manifold (DFT+U). We study the stability of p-FeOOH and its high-spin to low-spin transition. We explore the possible values of $x$ in this phase by comparison with experimental measurements of the unit cell volume. We also explore other properties that may hold clues to the nature of this phase at high pressure, including the internal structural parameters, vibrational frequencies, and band structure.

## 7.2 Methods

Our calculations are based on density functional theory (DFT), using the projector augmented wave (PAW) method (Kresse and Furthmüller, 1996; Kresse and Joubert, 1999). We use the PBEsol generalized gradient approximation Perdew et al. (2008), which we have previously shown to yield excellent agreement with iron-bearing oxides. To account for the

strong correlation, we use the +U method. On the basis of our previous results for the value of U-J for trivalent iron Insixiengmay and Stixrude (2023), we settled on a value of U-J = 3.2 eV. We use PAW potentials of 14, 1, and 6 valence electrons for Fe, H, and O with core radii of 1.16, 0.37, and 0.82 Å, respectively. We perform spin-polarized simulations where the difference in the number of up-spin and down-spin electrons on each Fe atom is set to the high-spin (5) or low-spin (1) value for both anti-ferromagnetic and ferromagnetic arrangements. We also explored a mixed-spin arrangement in which half of the Fe are high-spin and the other half are low-spin. We found that sampling the Brilliouin zone using a $4 \times 4 \times 4$ k-point mesh and a basis-set energy cutoff of 1000 eV was sufficient to converge energy and pressure to within 3 meV/atom and 0.5 GPa, respectively. For phonon calculations, we use a $2 \times 2 \times 2$ supercell and a $2 \times 2 \times 2$ k-point mesh.

We calculate the vibrational frequencies via density functional perturbation theory (DFPT) (Gajdoš et al., 2006). We follow similar methods in Insixiengmay and Stixrude (2023) to compute infrared (IR) intensities with Phonopy and Phonopy-Spectroscopy (Togo et al., 2023; Togo, 2023; Skelton et al., 2017). We find the pressure of the high-spin to low-spin transition as the point at which the Gibbs free energies of the two phases are equal:

$$G(P,T) = H(P,\text{static}) + F_{TH}(V,T)_P(V,T)V \tag{7.1}$$

where $H$ is the enthalpy at static (athermal) conditions, $G$ is the Gibbs free energy as a function of pressure $P$ and temperature $T$, $V$ is the volume, and $F_{TH}$ is the Helmholtz free energy derived from the (quasi-)harmonic phonon energy. The pressure

$$P(V,T) = P(V,\text{static}) + P_{TH}(V,T) \tag{7.2}$$

where the thermal pressure $P_{TH} = -(\partial F_{TH}/\partial V)_T$ (Figure 7.2) and

$$F_{TH} = \frac{1}{2}\sum_{qj}\hbar\omega_{qj} + k_B T \sum_{qj} \ln\left[1 - \exp\left(\frac{\hbar\omega_{qj}}{k_B T}\right)\right] \tag{7.3}$$

where $\omega_{qj}$ is the phonon frequency of mode $j$ at Brillouin zone point $q$.

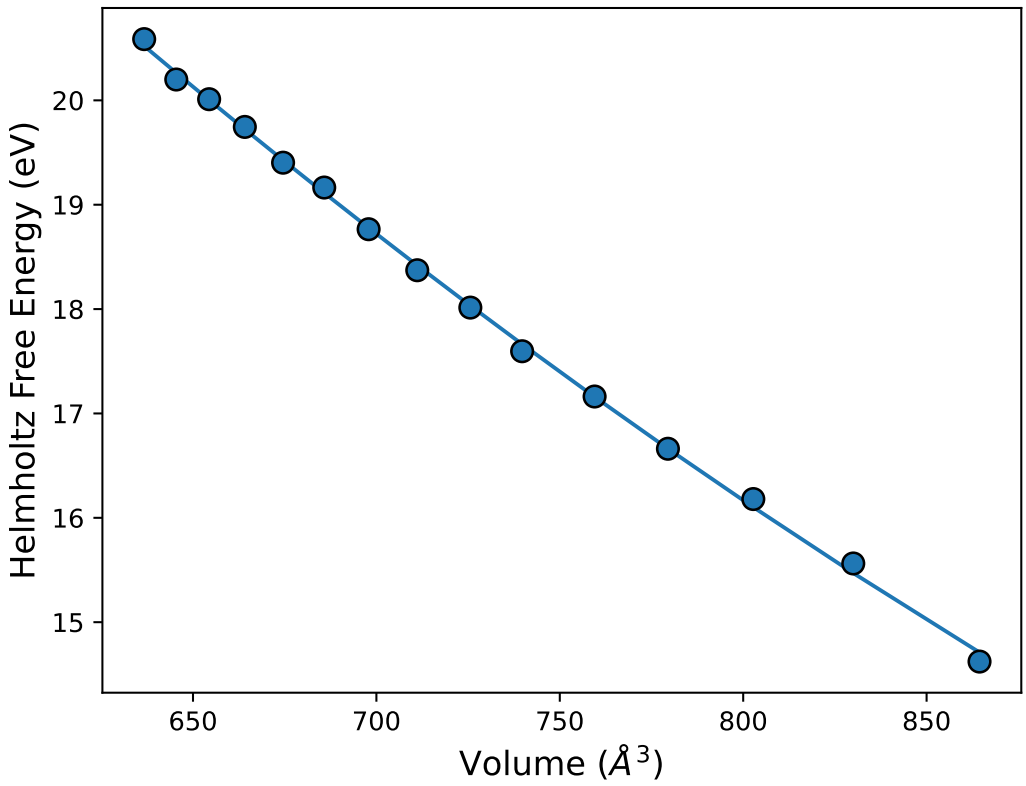


**Figure 7.2:** Thermal Helmholtz free energy at 300 K versus volume of LS AFM p-FeOOH. The derivative of the curve yields the thermal pressure of p-FeOOH.

## 7.3 Results

At static conditions, we find that the lowest energy spin arrangement is anti-ferromagnetic (AFM) at all pressures (Figure 7.3). The AFM state is more stable than the ferromagnetic (FM) state by 0.5 eV per unit cell at 90 GPa. At 45 GPa, we find a transition from high-

spin to low-spin AFM, in agreement with experimental studies (Liu et al., 2019). We also explored a mixed high-spin, low-spin state, and found that it is less stable than the high-spin state at 40 GPa by 0.25 eV. Because AFM is the most stable, all subsequent results refer to the AFM arrangement. We find the transition from the $\varepsilon$-FeOOH to the p-FeOOH phase at 90 GPa.

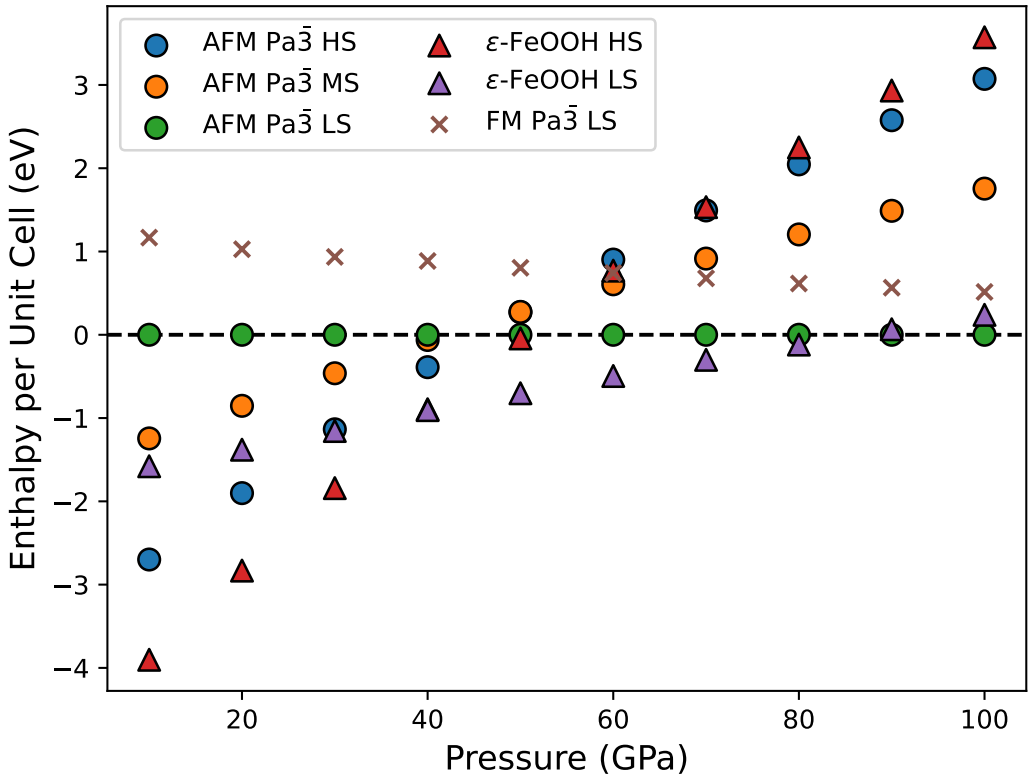


**Figure 7.3:** Enthalpy of FM and AFM states at static condition with respect to p-FeOOH AFM low-spin enthlapy. Circles represent AFM pyrite-structured FeOOH with space group $Pa\bar{3}$, triangles represent $\varepsilon$-FeOOH, and X marks the FM $Pa\bar{3}$ LS state.

Our equation of state is in reasonable agreement with the experimental study of Nishi et al. (2017) (Fig. 7.4). These authors argued that $x = 1$ in their experiments and that dehydrogenation did not occur. Their measured values of the volume are systematically larger

than our predictions, which may be the result of non-hydrostatic stress in their diamond anvil cell experiments, which is known to cause systematic over-estimation of the volume. The results of Yuan et al. (2018) are more scattered, and show even larger values of the volume as compared with those of Nishi et al. (2017). The larger volume in the experiments of Yuan et al. (2018) may also be attributable to deviatoric stress, and also suggest that $x = 1$ in their experiments. The results of other experiments (Hu et al., 2017; Mao et al., 2017) are more difficult to interpret. Both studies find volumes that are both larger and smaller than our predicted values. Whereas the larger volumes could also be attributed to deviatoric stress, the smaller volumes suggest $x < 1$, as also suggested by the authors.

We find that the IR active OH stretching mode has a frequency near 2000 cm$-1$ at 90 GPa, increasing with increasing pressure, behavior typical of symmetric hydrogen bonds (Fig. 7.5).

## 7.4 Discussion

While previous studies assumed that p-FeOOH had a low-spin configuration, based on behavior of the $\varepsilon$-FeOOH phase, we confirm that this is the case and locate the (metastable) high-spin to low-spin transition at 40 GPa, well within the stability field of the $\varepsilon$ phase (Thompson et al., 2021). We find that the most stable magnetic configuration is AFM, in contrast to an earlier study which considered only the ferromagnetic spin arrangement (Thompson et al., 2021).

Our predicted phase transition pressure from $\varepsilon$-FeOOH to p-FeOOH at 90 GPa is consistent with previous experimental findings that the transition takes place at pressures greater than 75 GPa (Thompson et al., 2021; Gleason et al., 2013; Hu et al., 2017; Hu and Liu, 2021a; Nishi et al., 2017; Zhuang et al., 2022). The transition pressure that we calculate is somewhat larger than that found in previous theoretical studies (by 10-20 GPa) (Nishi et al., 2017; Thompson et al., 2021; Hu et al., 2017). The difference may be due to the

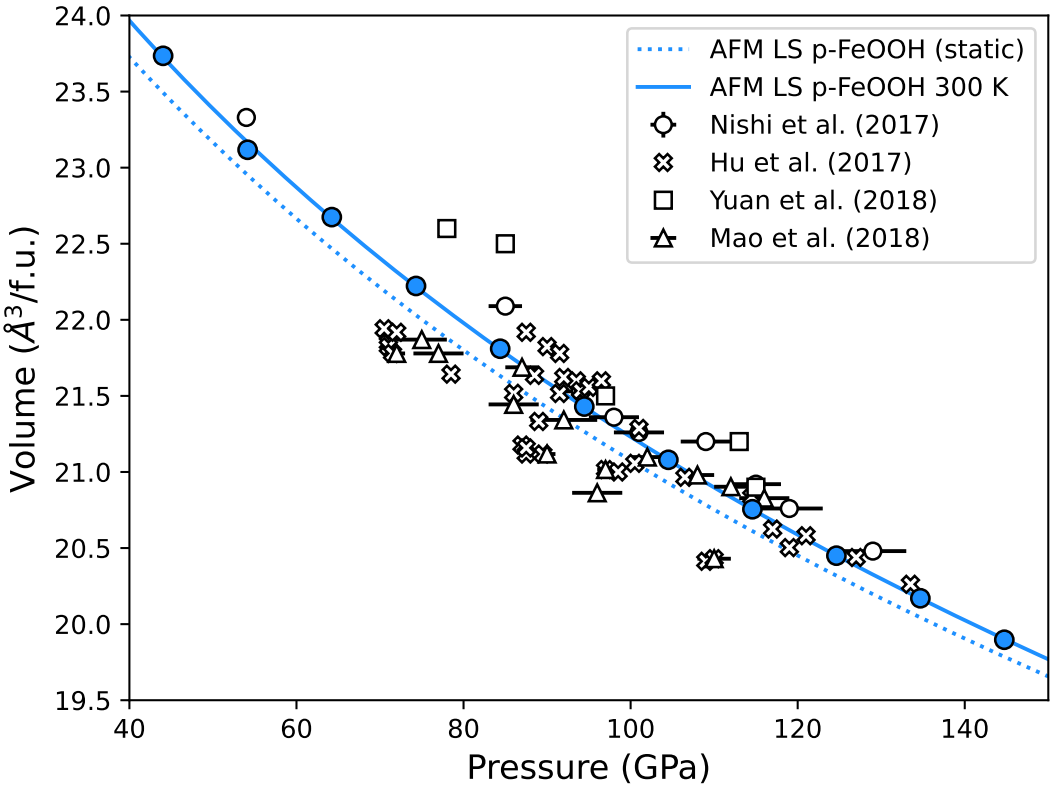


**Figure 7.4:** Pressure-volume equation of state for fully hydrated low-spin AFM p-FeOOH at static (dotted blue line) and 300 K (solid blue line) conditions. Symbols in blue represent the low-spin phase at 300 K. White symbols represent reported experimental values for p-FeOOH. Equation of state fit parameters $V_0$, $K_0$, and $K_0'$ are 109.43 Å, 226.33 ± 0.04 GPa, and 4.34 ± 0.001 for AFM $Pa\bar{3}$ low-spin at 300 K.

assumed exchange-correlation potential: whereas we assume PBEsol, previous studies have used PBE. In this context we note that PBEsol has been shown to yield excellent agreement with experiment (Insixiengmay and Stixrude, 2023; Holmström and Stixrude, 2015; Cortona, 2017).

The comparison of our equation of state with that experimentally measured highlights important sources of experimental uncertainty. We expect our results to be an accurate

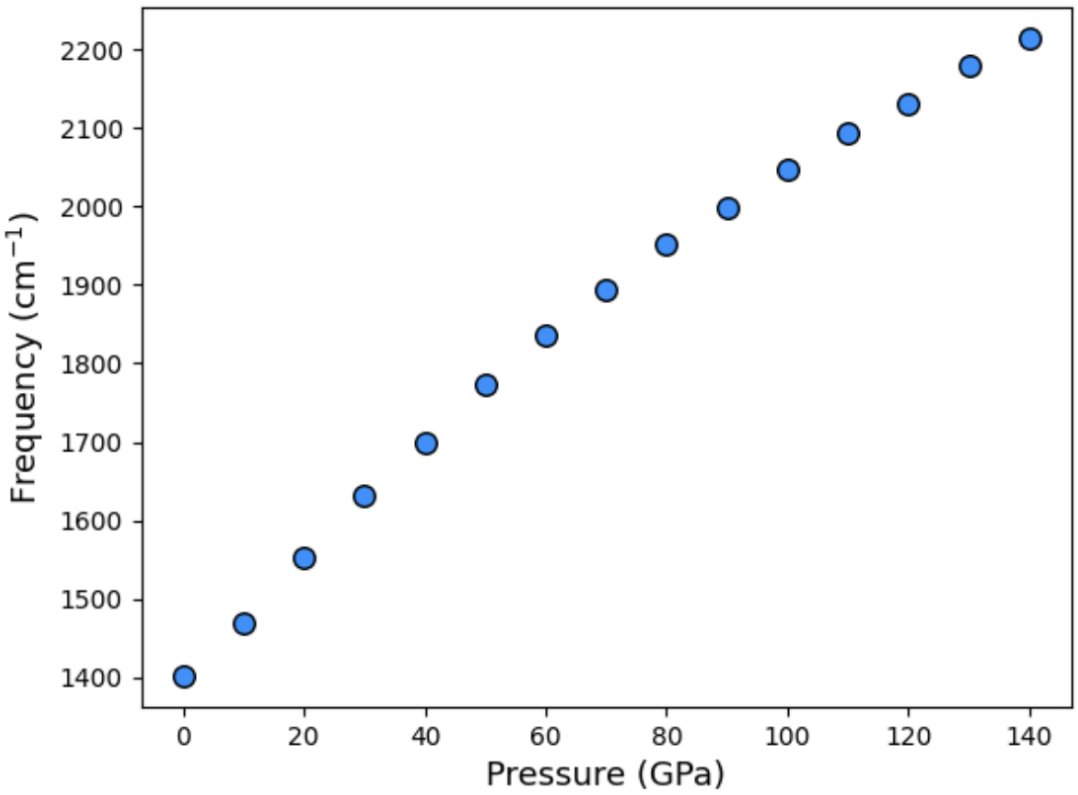


**Figure 7.5:** Pressure dependence of the IR O-H stretching vibrational mode frequencies with respect to pressure.

prediction of the equation of state of the $x = 1$ structure because of the excellent agreement that we find with the experimentally measured equation of state and structure of the $\varepsilon$ phase, for which the composition is known to be FeOOH. Agreement with the study of Nishi et al. (2017) is reasonably good. This study was unique in reverting the p-phase to the $\varepsilon$ phase upon reduction of pressure, providing strong evidence that $x = 1$ in these experiments. Using our results as a baseline, we find that it may be possible to explain some other experimental results, those with volumes less than ours, by dehydrogenation, and values of $x$ less than 1 (Hu et al., 2017; Mao et al., 2017). It is more difficult to explain experimentally measured volumes that are larger than ours, except possibly by the influence of deviatoric stress.

The IR spectrum of p-FeOOH has not yet been measured, and our prediction of the

frequency of the IR active OH stretching mode (Fig. 7.5) could be used to further test our preictions. A Raman spectroscopic study found a mode near 3500 $cm^{-1}$ (Hou et al., 2021), which decreases slightly in frequency with increasing pressure. The origin of the discrepancy with experiment is not clear. The experimental results are puzzling because both the measured frequency and its pressure dependence are typical of assymmetric hydrogen bonds, rather than the symmetric hydrogen bonds of the p-FeOOH phase. Moreover, the hydrogen-stretch in a symmetrically bonded configuration is Raman inactive. It is possible that the observed Raman mode originates in another, otherwise undetected phase, within the sample chamber, or could conceivably originate in adsorbed water at some point on the laser path.

## 7.5 Conclusions

Pyrite-structure FeOOH may be an important host of water in the deep lower mantle. We find that this phase is stable at pressures greater than 90 GPa, corresponding to 2000 km depth in the mantle. The phase is low-spin anti-ferromagnetic and is denser than the $\varepsilon$ phase. We find good agreement with some experimental measurements of this phase, particularly in those experiments where the composition can be confidently ascertained to be FeOOH (i.e. $x$=1). Comparison with experiment also reveals many remaining uncertainties, including the possibility of dehydrogenation, which is difficult to detect experimentally. We make predictions that may lead to better characterization of p-$FeOOH_x$, including the IR active vibrational mode frequencies, and the atomic coorinates, that could be tested against the results of future experimental studies.

# CHAPTER 8

# Conclusions

The projects in this thesis set out to push the forefront of understanding the interactions of major planet-forming materials at extreme pressure-temperature conditions such as those that prevail at the Earth's core-mantle boundary. Using first principles molecular dynamics simulations, I have determined the partitioning of nominally lithophile elements (Mg, Si, and O) in the Earth's core (Fe), finding substantial inter-solubility, and complete miscibility at temperatures exceeding 7000 K. I have also placed fundamental energetic constraints on the interaction of metal and ice components by exploring the physics of the FeOOH system, and making predictions its behavior, including solid-solid phase transitions, high-spin to low-spin transitions, insulator-metal transitions, and hydrogen-bond symmetrization.

Bibliography

Adamo, C., Barone, V., 1999. Toward reliable density functional methods without adjustable parameters: The pbe0 model. The Journal of chemical physics 110, 6158–6170.

Alfe, D., 2005. Melting curve of mgo from first-principles simulations. Physical review letters 94, 235701.

Allen, M.P., Tildesley, D.J., 2017. Computer simulation of liquids. Oxford university press.

Andersen, H.C., 1980. Molecular dynamics simulations at constant pressure and/or temperature. The Journal of chemical physics 72, 2384–2393.

Anisimov, V.I., Aryasetiawan, F., Lichtenstein, A.I., 1997. First-principles calculations of the electronic structure and spectra of strongly correlated systems: The LDA + U method. Journal of Physics Condensed Matter 9, 767–808. doi:10.1088/0953-8984/9/4/002.

Aoki, K., Yamawaki, H., Sakashita, M., Fujihisa, H., 1996. Infrared absorption study of the hydrogen-bond symmetrization in ice to 110 GPa. Physical Review B - Condensed Matter and Materials Physics 54, 15673–15677. doi:10.1103/PhysRevB.54.15673.

Badro, J., 2014. Spin Transitions in Mantle Minerals. Annual Review of Earth and Planetary Sciences 42, 231–248. URL: http://www.annualreviews.org/doi/10.1146/annurev-earth-042711-105304, doi:10.1146/annurev-earth-042711-105304.

Badro, J., Aubert, J., Hirose, K., Nomura, R., Blanchard, I., Borensztajn, S., Siebert, J., 2018. Magnesium Partitioning Between Earth's Mantle and Core and its Potential to Drive an Early Exsolution Geodynamo. Geophysical Research Letters 45, 13,240–13,248. doi:10.1029/2018GL080405.

Badro, J., Brodholt, J.P., Piet, H., Siebert, J., Ryerson, F.J., 2015. Core formation and core composition from coupled geochemical and geophysical constraints. Proceedings of the National Academy of Sciences 112, 12310–12314.

Badro, J., Siebert, J., Nimmo, F., 2016. An early geodynamo driven by exsolution of mantle components from Earth's core. Nature 536, 326–328. URL: http://dx.doi.org/10.1038/nature18594, doi:10.1038/nature18594.

Ballmer, M.D., Lourenço, D.L., Hirose, K., Caracas, R., Nomura, R., 2017. Reconciling magma-ocean crystallization models with the present-day structure of the earth's mantle. Geochemistry, Geophysics, Geosystems 18, 2785–2806.

Becke, A.D., 1988. Density-functional exchange-energy approximation with correct asymptotic behavior. Physical review A 38, 3098.

Bevington, P.R., Robinson, D.K., 2003. Data reduction and error analysis. McGrawâ€"Hill, New York .

Biggin, A.J., Strik, G.H., Langereis, C.G., 2009. The intensity of the geomagnetic field in the late-archaean: new measurements and an analysis of the updated iaga palaeointensity database. Earth, Planets and Space 61, 9–22.

Blaha, P., Schwarz, K., Herzig, P., 1985. First-principles calculation of the electric field gradient of li 3 n. Physical review letters 54, 1192.

Blöchl, P.E., 1994. Projector augmented-wave method. Phys. Rev. B 50, 17953–17979. URL: https://link.aps.org/doi/10.1103/PhysRevB.50.17953, doi:10.1103/PhysRevB.50.17953.

Blochl, P.E., Jepsen, O., Andersen, O.K., 1994. Improved tetrahedron method for Brillouin-zone integrations. Physical Review B 49, 223–233.

Bohr, N., 1913. Lxxiii. on the constitution of atoms and molecules. The London, Edinburgh, and Dublin Philosophical Magazine and Journal of Science 26, 857–875.

Bolotina, N.B., Molchanov, V.N., Dyuzheva, T.I., Lityagina, L.M., Bendeliani, N.A., 2008. Single-crystal structures of high-pressure phases FeOOH, FeOOD, and GaOOH. Crystallography Reports 53, 960–965. doi:10.1134/S1063774508060084.

Boltzmann, L., 1872. Weitere studien über das warmegleichgewicht unter gasmolekülen (further studies on the thermal equilibrium of gas molecules, the kinetic theory of gases). Sitzungsberichte Akademie der Wissenschaften 66, 275–370.

Boltzmann, L., 1877. Über die Beziehung zwischen dem zweiten Hauptsatze des mechanischen Wärmetheorie und der Wahrscheinlichkeitsrechnung, respective den Sätzen über das Wärmegleichgewicht. Kk Hof-und Staatsdruckerei.

Bono, R.K., Paterson, G.A., van der Boon, A., Engbers, Y.A., Michael Grappone, J., Handford, B., Hawkins, L.M., Lloyd, S.J., Sprain, C.J., Thallner, D., et al., 2022. The pint database: A definitive compilation of absolute palaeomagnetic intensity determinations since 4 billion years ago. Geophysical Journal International 229, 522–545.

Born, M., Huang, K., 1996. Dynamical theory of crystal lattices. Oxford university press.

Born, M., Oppenheimer, R., 1927. Zur Quantentheorie der Molekeln. Annalen der Physik 389, 457–484. doi:10.1002/andp.19273892002.

Boyet, M., Carlson, R.W., 2005. 142nd evidence for early (¿ 4.53 ga) global differentiation of the silicate earth. Science 309, 576–581.

Braginsky, S., 1963. Structure of f layer and reason for convection in the earth's core, in: Soviet. Phys. Dokl., pp. 8–11.

Buff, F., Lovett, R., Stillinger Jr, F., 1965. Interfacial density profile for fluids in the critical region. Physical Review Letters 15, 621.

Bukowinski, M., 1977. A theoretical equation of state for the inner core. Physics of the Earth and Planetary Interiors 14, 333–344.

Burns, R.G., 1993. Mineralogical applications of crystal field theory. 5, Cambridge university press.

Canup, R.M., Asphaug, E., 2001. Origin of the Moon in a giant impact near the end of the Earth's formation. Nature 412, 708–712.

Ceperley, D.M., Alder, B.J., 1980. Ground state of the electron gas by a stochastic method. Physical review letters 45, 566.

Chen, H., Leinenweber, K., Prakapenka, V., Prescher, C., Meng, Y., Bechtel, H., Kunz, M., Shim, S.H., 2020. Possible H2O storage in the crystal structure of CaSiO3 perovskite. Physics of the Earth and Planetary Interiors 299, 106412. URL: https://doi.org/10.1016/j.pepi.2019.106412, doi:10.1016/j.pepi.2019.106412.

Chidester, B.A., Lock, S., Swadba, K.E., Rahman, Z., Righter, K., Campbell, A.J., 2022a. The lithophile element budget of earth's core. Geochemistry, Geophysics, Geosystems 23, e2021GC009986.

Chidester, B.A., Lock, S.J., Swadba, K.E., Rahman, Z., Righter, K., Campbell, A.J., 2022b. The Lithophile Element Budget of Earth's Core. Geochemistry, Geophysics, Geosystems 23. doi:10.1029/2021GC009986.

Christensen, U.R., Aubert, J., 2006. Scaling properties of convection-driven dynamos in rotating spherical shells and application to planetary magnetic fields. Geophysical Journal International 166, 97–114.

Cococcioni, M., De Gironcoli, S., 2005. Linear response approach to the calculation of the effective interaction parameters in the lda+ u method. Physical Review B 71, 035105.

Coles, S.W., Mangaud, E., Frenkel, D., Rotenberg, B., 2021. Reduced variance analysis of molecular dynamics simulations by linear combination of estimators. The Journal of Chemical Physics 154.

Cortona, P., 2017. Hydrogen bond symmetrization and elastic constants under pressure of $\delta$-alooh. Journal of Physics: Condensed Matter 29, 325505.

Davisson, C., Germer, L.H., 1927. The scattering of electrons by a single crystal of nickel. Nature 119, 558–560.

De Broglie, L., 1923. Waves and quanta. Nature 112, 540–540.

Deng, J., Stixrude, L., 2021. Deep fractionation of hf in a solidifying magma ocean and its implications for tungsten isotopic heterogeneities in the mantle. Earth and Planetary Science Letters 562, 116873.

Desjarlais, M.P., 2013. First-principles calculation of entropy for liquid metals. Physical Review E 88, 062145.

Dirac, P.A., 1930. Note on exchange phenomena in the thomas atom, in: Mathematical proceedings of the Cambridge philosophical society, Cambridge University Press. pp. 376–385.

Dovesi, R., Saunders, V., Roetti, C., Orlando, R., Zicovich-Wilson, C., Pascale, F., Civalleri, B., Doll, K., Harrison, N., Bush, I., et al., 2017. Crystal17 .

Du, Z., Jackson, C., Bennett, N., Driscoll, P., Deng, J., Lee, K.K., Greenberg, E., Prakapenka, V.B., Fei, Y., 2017. Insufficient Energy From MgO Exsolution to Power Early Geodynamo. Geophysical Research Letters 44, 11,376–11,381. doi:10.1002/2017GL075283.

Dudarev, S.L., Botton, G.A., Savrasov, S.Y., Humphreys, C., Sutton, A.P., 1998. Electron-energy-loss spectra and the structural stability of nickel oxide: An lsda+ u study. Physical Review B 57, 1505.

Eckart, C., 1935. Some studies concerning rotating axes and polyatomic molecules. Physical Review 47, 552.

Einstein, A., 1905. Generation and conversion of light with regard to a heuristic point of view. Annalen Der Physik 17, 132–148.

Evans, D.J., 1983. Computer "experiment"for nonlinear thermodynamics of couette flow. The Journal of Chemical Physics 78, 3297–3302.

Fermi, E., 1927. Un metodo statistico per la determinazione di alcune priorieta dell'atome. Rend. Accad. Naz. Lincei 6, 32.

Feynman, R.P., 1939. Forces in molecules. Physical review 56, 340.

Filatov, M., Thiel, W., 1997. A new gradient-corrected exchange-correlation density functional. Molecular Physics 91, 847–860.

Fischer, R.A., Nakajima, Y., Campbell, A.J., Frost, D.J., Harries, D., Langenhorst, F., Miyajima, N., Pollok, K., Rubie, D.C., 2015. High pressure metal-silicate partitioning of Ni, Co, V, Cr, Si, and O. Geochimica et Cosmochimica Acta 167, 177–194. doi:10.1016/j.gca.2015.06.026.

Flasar, F.M., Birch, F., 1973. Energetics of core formation-a correction. Journal of Geophysical Research 78.

Flyvbjerg, H., Petersen, H.G., 1989. Error estimates on averages of correlated data. The Journal of Chemical Physics 91, 461–466.

Fock, V., 1930. Näherungsmethode zur lösung des quantenmechanischen mehrkörperproblems. Zeitschrift für Physik 61, 126–148.

Frenkel, D., Smit, B., 2001. Understanding molecular simulation: from algorithms to applications. volume 1. Elsevier.

Fu, S., Yang, J., ichiro Karato, S., Vasiliev, A., Presniakov, M.Y., Gavrilliuk, A.G., Ivanova, A.G., Hauri, E.H., Okuchi, T., Purevjav, N., Lin, J.F., 2019. Water Concentration in

Single-Crystal (Al,Fe)-Bearing Bridgmanite Grown From the Hydrous Melt: Implications for Dehydration Melting at the Topmost Lower Mantle. Geophysical Research Letters 46, 10346–10357. doi:10.1029/2019GL084630.

Gajdoš, M., Hummer, K., Kresse, G., Furthmüller, J., Bechstedt, F., 2006. Linear optical properties in the projector-augmented wave methodology. Physical Review B - Condensed Matter and Materials Physics 73, 1–9. doi:10.1103/PhysRevB.73.045112.

Garnero, E.J., McNamara, A.K., 2008. Structure and dynamics of earth's lower mantle. science 320, 626–628.

Gell-Mann, M., Brueckner, K.A., 1957. Correlation energy of an electron gas at high density. Physical Review 106, 364.

Giannozzi, P., Baroni, S., 1994. Vibrational and dielectric properties of C60 from density-functional perturbation theory. The Journal of Chemical Physics 100, 8537–8539. doi:10.1063/1.466753.

Gillan, M., Alfe, D., Brodholt, J., Vočadlo, L., Price, G., 2006. First-principles modelling of earth and planetary materials at high pressures and temperatures. Reports on progress in physics 69, 2365.

Gleason, A.E., Jeanloz, R., Kunz, M., 2008. Pressure-temperature stability studies of feooh using x-ray diffraction. American Mineralogist 93, 1882–1885.

Gleason, A.E., Quiroga, C.E., Suzuki, A., Pentcheva, R., Mao, W.L., 2013. Symmetrization driven spin transition in $\epsilon$-FeOOH at high pressure. Earth and Planetary Science Letters 379, 49–55. URL: http://dx.doi.org/10.1016/j.epsl.2013.08.012, doi:10.1016/j.epsl.2013.08.012.

Goncharov, A.F., Struzhkin, V.V., Mao, H.K., Hemley, R.J., 1999. Raman spectroscopy of

dense h2o and the transition to symmetric hydrogen bonds. Physical Review Letters 83, 1998–2001. doi:10.1103/PhysRevLett.83.1998.

Gonze, X., Lee, C., 1997. Dynamical matrices, Born effective charges, dielectric permittivity tensors, and interatomic force constants from density-functional perturbation theory. Physical Review B - Condensed Matter and Materials Physics 55, 10355–10368. doi:10.1103/PhysRevB.55.10355.

Gubbins, D., et al., 1977. Energetics of the earth's core. Journal of Geophysics 43, 453–464.

Harrison, W.A., 2012. Electronic structure and the properties of solids: the physics of the chemical bond. Courier Corporation.

Hartree, D.R., 1928a. The wave mechanics of an atom with a non-coulomb central field. part i. theory and methods, in: Mathematical Proceedings of the Cambridge Philosophical Society, Cambridge university press. pp. 89–110.

Hartree, D.R., 1928b. The wave mechanics of an atom with a non-coulomb central field. part ii. some results and discussion, in: Mathematical Proceedings of the Cambridge Philosophical Society, Cambridge University Press. pp. 111–132.

Hartree, D.R., 1928c. The wave mechanics of an atom with a non-coulomb central field. part iii. term values and intensities in series in optical spectra, in: Mathematical Proceedings of the Cambridge Philosophical Society, Cambridge University Press. pp. 426–437.

Hellmann, H., 1937. Einfuhrung in die quantenchemie .

Henkelman, G., Arnaldsson, A., Jónsson, H., 2006. A fast and robust algorithm for bader decomposition of charge density. Computational Materials Science 36, 354–360.

Heyd, J., Scuseria, G.E., Ernzerhof, M., 2003. Hybrid functionals based on a screened coulomb potential. The Journal of chemical physics 118, 8207–8215.

Hill, R., 1952. The elastic behaviour of a crystalline aggregate. Proceedings of the Physical Society. Section A 65, 349–354. doi:10.1088/0370-1298/65/5/307.

Himmetoglu, B., Floris, A., De Gironcoli, S., Cococcioni, M., 2014. Hubbard-corrected dft energy functionals: The lda+ u description of correlated systems. International Journal of Quantum Chemistry 114, 14–49.

Hirose, K., Morard, G., Sinmyo, R., Umemoto, K., Hernlund, J., Helffrich, G., Labrosse, S., 2017. Crystallization of silicon dioxide and compositional evolution of the Earth's core. Nature 543, 99–102. URL: http://dx.doi.org/10.1038/nature21367, doi:10.1038/nature21367.

Hirose, K., Wood, B., Vočadlo, L., 2021. Light elements in the earth's core. Nature Reviews Earth & Environment 2, 645–658.

Hirschmann, M.M., 2006. Water, melting, and the deep Earth H2O cycle. Annual Review of Earth and Planetary Sciences 34, 629–653. doi:10.1146/annurev.earth.34.031405.125211.

Hohenberg, P., Kohn, W., 1964. Inhomogeneous electron gas. Physical review 136, B864.

Holmström, E., Stixrude, L., 2015. Spin crossover in ferropericlase from first-principles molecular dynamics. Physical review letters 114, 117202.

Holmström, E., Stixrude, L., 2015. Spin crossover in ferropericlase from first-principles molecular dynamics. Physical Review Letters 114. doi:10.1103/PhysRevLett.114.117202.

Holzapfel, W.B., 1972. On the symmetry of the hydrogen bonds in ice VII. The Journal of Chemical Physics 56, 838–844. doi:10.1063/1.1677221.

Hoover, W.G., 1985. Canonical dynamics: Equilibrium phase-space distributions. Physical review A 31, 1695.

Hoover, W.G., Ladd, A.J., Moran, B., 1982. High-strain-rate plastic flow studied via nonequilibrium molecular dynamics. Physical Review Letters 48, 1818.

Hou, M., He, Y., Jang, B.G., Sun, S., Zhuang, Y., Deng, L., Tang, R., Chen, J., Ke, F., Meng, Y., et al., 2021. Superionic iron oxide–hydroxide in earth's deep mantle. Nature Geoscience 14, 174–178.

Hu, Q., Kim, D.Y., Liu, J., Meng, Y., Yang, L., Zhang, D., Mao, W.L., Mao, H.k., 2017. Dehydrogenation of goethite in earth's deep lower mantle. Proceedings of the National Academy of Sciences 114, 1498–1501.

Hu, Q., Kim, D.Y., Yang, W., Yang, L., Meng, Y., Zhang, L., Mao, H.K., 2016. Feo2 and feooh under deep lower-mantle conditions and earth's oxygen–hydrogen cycles. Nature 534, 241–244.

Hu, Q., Liu, J., 2021a. Deep mantle hydrogen in the pyrite-type feo2–feo2h system. Geoscience Frontiers 12, 975–981.

Hu, Q., Liu, J., 2021b. Deep mantle hydrogen in the pyrite-type FeO2–FeO2H system. Geoscience Frontiers 12, 975–981. doi:10.1016/j.gsf.2020.04.006.

Hubbard, J., 1964a. Electron correlations in narrow energy bands. ii. the degenerate band case. Proceedings of the Royal Society of London. Series A. Mathematical and Physical Sciences 277, 237–259.

Hubbard, J., 1964b. Electron correlations in narrow energy bands iii. an improved solution. Proceedings of the Royal Society of London. Series A. Mathematical and Physical Sciences 281, 401–419.

Hubbard, J., 1965. Electron correlations in narrow energy bands-iv. the atomic representation. Proceedings of the Royal Society of London. Series A. Mathematical and Physical Sciences 285, 542–560.

Hubbard, J., 1967a. Electron correlations in narrow energy bands v. a perturbation expansion about the atomic limit. Proceedings of the Royal Society of London. Series A. Mathematical and Physical Sciences 296, 82–99.

Hubbard, J., 1967b. Electron correlations in narrow energy bands vi. the connexion with many-body perturbation theory. Proceedings of the Royal Society of London. Series A. Mathematical and Physical Sciences 296, 100–112.

Ikeda, O., Sakamaki, T., Ohashi, T., Goto, M., Higo, Y., Suzuki, A., 2019. Sound velocity measurements of $\epsilon$-FeOOH up to 24 GPa. Journal of Mineralogical and Petrological Sciences 114, 155–160. doi:10.2465/jmps.181115b.

Insixiengmay, L., Stixrude, L., 2023. Hydrogen bond symmetrization and high-spin to low-spin transition of $\varepsilon$-feooh at the pressure of earth's lower mantle. American Mineralogist 108, 2209–2218.

Isbister, D., McQuarrie, D., 1972. On the calculation of the coefficient of self-diffusion. The Journal of Chemical Physics 56, 736–738.

Jeanloz, R., Richter, F.M., 1979. Convection, composition, and the thermal state of the lower mantle. Journal of Geophysical Research: Solid Earth 84, 5497–5504.

Jones, G.M., 1977. Thermal interaction of the core and the mantle and long-term behavior of the geomagnetic field. Journal of Geophysical Research 82, 1703–1709.

Kohn, W., Sham, L.J., 1965. Self-consistent equations including exchange and correlation effects. Physical review 140, A1133.

de Koker, N., Karki, B.B., Stixrude, L., 2013. Thermodynamics of the mgo–sio2 liquid system in earth's lowermost mantle from first principles. Earth and planetary science letters 361, 58–63.

Kresse, G., Furthmüller, J., 1996. Efficient iterative schemes for ab initio total-energy calculations using a plane-wave basis set. Physical Review B - Condensed Matter and Materials Physics 54, 11169–11186. doi:10.1103/PhysRevB.54.11169.

Kresse, G., Joubert, D., 1999. From ultrasoft pseudopotentials to the projector augmented-wave method. Physical Review B - Condensed Matter and Materials Physics 59, 1758–1775. doi:10.1103/PhysRevB.59.1758.

Kuwayama, Y., Hirose, K., Sata, N., Ohishi, Y., 2005. The pyrite-type high-pressure form of silica. Science 309, 923–925.

Labrosse, S., 2003. Thermal and magnetic evolution of the earth's core. Physics of the Earth and Planetary Interiors 140, 127–143.

Labrosse, S., Hernlund, J., Coltice, N., 2007. A crystallizing dense magma ocean at the base of the earth's mantle. Nature 450, 866–869.

Labrosse, S., Poirier, J.P., Le Mouël, J.L., 2001. The age of the inner core. Earth and Planetary Science Letters 190, 111–123.

Landeau, M., Fournier, A., Nataf, H.C., Cébron, D., Schaeffer, N., 2022. Sustaining earth's magnetic dynamo. Nature Reviews Earth & Environment 3, 255–269.

Lay, T., Hernlund, J., Buffett, B.A., 2008. Core – mantle boundary heat flow. Nature Geoscience 1, 25–32.

Le Page, Y., Saxe, P., 2002. Symmetry-general least-squares extraction of elastic data for strained materials from ab initio calculations of stress. Physical Review B 65, 1–14. doi:10.1103/PhysRevB.65.104104.

Lee, C., Yang, W., Parr, R.G., 1988. Development of the colle-salvetti correlation-energy formula into a functional of the electron density. Physical review B 37, 785.

Léorat, J., Nore, C., 2008. Interplay between experimental and numerical approaches in the fluid dynamo problem. Comptes Rendus. Physique 9, 741–748.

Li, J., Agee, C.B., 1996. Geochemistry of mantle–core differentiation at high pressure. Nature 381, 686–689.

Lin, J.f., Struzhkin, V.V., Jacobsen, S.D., Hu, M.Y., Chow, P., Kung, J., Liu, H., Mao, H.k., Hemley, R.J., 2005. Spin transition of iron in magnesiowu Earth's lower mantle. Nature 436, 377–380. doi:10.1038/nature03825.

Litasov, K.D., Ohtani, E., 2007. Effect of water on the phase relations in Earth's mantle and deep water cycle. volume 421. doi:10.1130/2007.2421(08).

Liu, J., Dorfman, S.M., Zhu, F., Li, J., Wang, Y., Zhang, D., Xiao, Y., Bi, W., Ercan Alp, E., 2018. Valence and spin states of iron are invisible in Earth's lower mantle. Nature Communications 9, 1–9. URL: http://dx.doi.org/10.1038/s41467-018-03671-5, doi:10.1038/s41467-018-03671-5.

Liu, J., Hu, Q., Bi, W., Yang, L., Xiao, Y., Chow, P., Meng, Y., Prakapenka, V.B., Mao, H.K., Mao, W.L., 2019. Altered chemistry of oxygen and iron under deep earth conditions. Nature Communications 10, 153.

Liu, J., Lin, J.F., Mao, Z., Prakapenka, V.B., 2014. Thermal equation of state and spin transition of magnesiosiderite at high pressure and temperature. American Mineralogist 99, 84–93.

Liu, Z., Fei, H., Chen, L., McCammon, C., Wang, L., Liu, R., Wang, F., Liu, B., Katsura, T., 2021. Bridgmanite is nearly dry at the top of the lower mantle. Earth and Planetary Science Letters 570, 117088. URL: https://doi.org/10.1016/j.epsl.2021.117088, doi:10.1016/j.epsl.2021.117088.

Loper, D.E., 1978. The gravitationally powered dynamo. Geophysical Journal International 54, 389–404.

Maller, A., Landeau, M., Allibert, L., Charnoz, S., 2024. Condition for metal fragmentation during earth-forming collisions. Physics of the Earth and Planetary Interiors , 107199.

Mao, H.K., Hu, Q., Yang, L., Liu, J., Kim, D.Y., Meng, Y., Zhang, L., Prakapenka, V.B., Yang, W., Mao, W.L., 2017. When water meets iron at earth's core–mantle boundary. National Science Review 4, 870–878.

Marquardt, H., Buchen, J., Mendez, A.S., Kurnosov, A., Wendt, M., Rothkirch, A., Pennicard, D., Liermann, H.P., 2018. Elastic Softening of (Mg0.8Fe0.2)O Ferropericlase Across the Iron Spin Crossover Measured at Seismic Frequencies. Geophysical Research Letters 45, 6862–6868. doi:10.1029/2018GL077982.

Mattheiss, L., Hamann, D., 1986. Linear augmented-plane-wave calculation of the structural properties of bulk cr, mo, and w. Physical Review B 33, 823.

Maxwell, J.C., 1860a. Ii. illustrations of the dynamical theory of gases. The London, Edinburgh, and Dublin Philosophical Magazine and Journal of Science 20, 21–37.

Maxwell, J.C., 1860b. V. illustrations of the dynamical theory of gases.—part i. on the motions and collisions of perfectly elastic spheres. The London, Edinburgh, and Dublin Philosophical Magazine and Journal of Science 19, 19–32.

McQuarrie, D., 1975. Statistical Mechanics. Chemistry Series, Harper & Row. URL: https://books.google.com/books?id=PANRAAAAMAAJ.

McQuarrie, D.A., 2008. Quantum chemistry. University Science Books.

Meier, T., Petitgirard, S., Khandarkhaeva, S., Dubrovinsky, L., 2018. Observation of nuclear quantum effects and hydrogen bond symmetrisation in high pressure ice. Na-

ture Communications 9, 1–7. URL: http://dx.doi.org/10.1038/s41467-018-05164-x, doi:10.1038/s41467-018-05164-x, arXiv:1803.07019.

Meng, Y., Weidner, D.J., Fei, Y., 1993. Deviatoric Stress in a Quasi-hydrostatic diamond anvil cell: effect on the volume-based pressure calibration. Geophysical Research Letters 20, 1147–1150.

Mermin, N.D., 1965. Thermal properties of the inhomogeneous electron gas. Physical Review 137, A1441.

Momma, K., Izumi, F., 2008. VESTA: A three-dimensional visualization system for electronic and structural analysis. Journal of Applied Crystallography 41, 653–658. doi:10.1107/S0021889808012016.

Mosey, N.J., Liao, P., Carter, E.A., 2008. Rotationally invariant ab initio evaluation of Coloumb and exchange parameters for DFT+U calculations. Journal of Chemical Physics 129, 1–13. doi:10.1063/1.2943142.

Mound, J., Davies, C., Rost, S., Aurnou, J., 2019. Regional stratification at the top of earth's core due to core–mantle boundary heat flux variations. Nature Geoscience 12, 575–580.

Musgrave, M.J.P., 1970. Crystal Acoustics. Holden-Day, San Francisco.

Nakajima, M., Stevenson, D.J., 2015. Melting and mixing states of the earth's mantle after the moon-forming impact. Earth and Planetary Science Letters 427, 286–295.

Nishi, M., Kuwayama, Y., Tsuchiya, J., Tsuchiya, T., 2017. The pyrite-type high-pressure form of feooh. Nature 547, 205–208.

Nishi, M., Tsuchiya, J., Kuwayama, Y., Arimoto, T., Tange, Y., 2019. Solid Solution and Compression Behavior of Hydroxides in the Lower Mantle Journal of Geophysical Research : Solid Earth. Journal of Geophysical Research: Solid Earth 124, 10231–10239. doi:10.1029/2019JB018146.

Nosé, S., 1984a. A molecular dynamics method for simulations in the canonical ensemble. Molecular physics 52, 255–268.

Nosé, S., 1984b. A unified formulation of the constant temperature molecular dynamics methods. The Journal of chemical physics 81, 511–519.

Nosé, S., 1991. Constant temperature molecular dynamics methods. Progress of Theoretical Physics Supplement 103, 1–46.

Ohira, I., Jackson, J.M., Solomatova, N.V., Sturhahn, W., Finkelstein, G.J., Kamada, S., Kawazoe, T., Maeda, F., Hirao, N., Nakano, S., Toellner, T.S., Suzuki, A., Ohtani, E., 2019. Compressional behavior and spin state of $\delta$-(Al,Fe)OOH at high pressures. American Mineralogist 104, 1273–1284.

Ohira, I., Jackson, J.M., Sturhahn, W., Finkelstein, G.J., Kawazoe, T., Toellner, T.S., Suzuki, A., Ohtani, E., 2021. The influence of $\delta$-(Al,Fe)OOH on seismic heterogeneities in Earth's lower mantle. Scientific Reports 11, 1–9. URL: https://doi.org/10.1038/s41598-021-91180-9, doi:10.1038/s41598-021-91180-9.

Olson, P., Schubert, G., Anderson, C., 1987. Plume formation in the d -layer and the roughness of the core–mantle boundary. Nature 327, 409–413.

Ono, S., Tsuchiya, T., Hirose, K., Ohishi, Y., 2003. High-pressure form of pyrite-type germanium dioxide. Physical review B 68, 014103.

O'Rourke, J.G., Korenaga, J., Stevenson, D.J., 2017. Thermal evolution of earth with magnesium precipitation in the core. Earth and Planetary Science Letters 458, 263–272.

O'Rourke, J.G., Stevenson, D.J., 2016. Powering earth's dynamo with magnesium precipitation from the core. Nature 529, 387–389.

Parrinello, M., Rahman, A., 1980. Crystal structure and pair potentials: A molecular-dynamics study. Physical review letters 45, 1196.

Parrinello, M., Rahman, A., 1981. Polymorphic transitions in single crystals: A new molecular dynamics method. Journal of Applied physics 52, 7182–7190.

Pauli, W., 1925a. On the connexion between the completion of electron groups in an atom with the complex structure of spectra. Zeitschrift für Physik 31, 765.

Pauli, W., 1925b. Über den zusammenhang des abschlusses der elektronengruppen im atom mit der komplexstruktur der spektren. Einführ. Orig 229, 765–783.

Pauli, W., 1940. The connection between spin and statistics. Physical Review 58, 716.

Payne, M.C., Teter, M.P., Allan, D.C., Arias, T., Joannopoulos, a.J., 1992. Iterative minimization techniques for ab initio total-energy calculations: molecular dynamics and conjugate gradients. Reviews of modern physics 64, 1045.

Pearson, D.G., Brenker, F.E., Nestola, F., McNeill, J., Nasdala, L., Hutchison, M.T., Matveev, S., Mather, K., Silversmit, G., Schmitz, S., Vekemans, B., Vincze, L., 2014. Hydrous mantle transition zone indicated by ringwoodite included within diamond. Nature 507, 221–224. URL: http://dx.doi.org/10.1038/nature13080, doi:10.1038/nature13080.

Perdew, J.P., Burke, K., Ernzerhof, M., 1996. Generalized gradient approximation made simple. Physical Review Letters 77, 3865–3868. doi:10.1103/PhysRevLett.77.3865.

Perdew, J.P., Burke, K., Ernzerhof, M., 1998. Perdew, burke, and ernzerhof reply. Physical Review Letters 80, 891.

Perdew, J.P., Chevary, J.A., Vosko, S.H., Jackson, K.A., Pederson, M.R., Singh, D.J., Fiolhais, C., 1992. Atoms, molecules, solids, and surfaces: Applications of the generalized gradient approximation for exchange and correlation. Physical review B 46, 6671.

Perdew, J.P., Ruzsinszky, A., Csonka, G.I., Vydrov, O.A., Scuseria, G.E., Constantin, L.A., Zhou, X., Burke, K., 2008. Restoring the density-gradient expansion for exchange in solids

and surfaces. Physical Review Letters 100, 1–4. doi:10.1103/PhysRevLett.100.136406, arXiv:0711.0156.

Perdew, J.P., Wang, Y., 1992. Accurate and simple analytic representation of the electron-gas correlation energy. Physical review B 45, 13244.

Perdew, J.P., Zunger, A., 1981. Self-interaction correction to density-functional approximations for many-electron systems. Physical Review B 23, 5048.

Pernet, M., Chenavas, J., Joubert, J.L., Meyer, C., Gros, Y., 1973. Caracterisation et etude pareffet mossbauer d'une nouvelle variete hautepression de FeOOH. Solid State Communications 13, 1147–1154.

Pernet, M., Joubert, J.C., Berthet-Colominas, C., 1975. Etude par diffraction neutroniquede la forme haute pression de FeOOH. Solid State Communications 17, 1505–1510.

Pick, R.M., Cohen, M.H., Martin, R.M., 1970. Microscopic Theory of Force Constants in the Adiabatic Approximation. Physical Review B 1, 910–920.

Planck, M., 1901. On the law of the energy distribution in the normal spectrum. Ann. Phys 4, 1–11.

Püthe, C., Kuvshinov, A., Khan, A., Olsen, N., 2015. A new model of Earth's radial conductivity structure derived from over 10 yr of satellite and observatory magnetic data. Geophysical Journal International 203, 1864–1872. doi:10.1093/gji/ggv407.

Righter, K., Drake, M., Yaxley, G., 1997. Prediction of siderophile element metal-silicate partition coefficients to 20 gpa and 2800 c: the effects of pressure, temperature, oxygen fugacity, and silicate and metallic melt compositions. Physics of the Earth and Planetary Interiors 100, 115–134.

Rollmann, G., Rohrbach, A., Entel, P., Hafner, J., 2004. First-principles calculation of the structure and magnetic phases of hematite. Physical Review B - Condensed Matter and Materials Physics 69, 1–12. doi:10.1103/PhysRevB.69.165107.

Rotenberg, B., 2020. Use the force! reduced variance estimators for densities, radial distribution functions, and local mobilities in molecular simulations. The Journal of Chemical Physics 153.

Sano, A., Yagi, T., Okada, T., Gotou, H., Ohtani, E., Tsuchiya, J., Kikegawa, T., 2008. X-ray diffraction study of high pressure transition in inooh. Journal of Mineralogical and Petrological Sciences 103, 152–155.

Sano-Furukawa, A., Hattori, T., Komatsu, K., Kagi, H., Nagai, T., Molaison, J.J., dos Santos, A.M., Tulk, C.A., 2018. Direct observation of symmetrization of hydrogen bond in $\delta$-AlOOH under mantle conditions using neutron diffraction. Scientific Reports 8, 1–9. doi:10.1038/s41598-018-33598-2.

Santra, B., Michaelides, A., Scheffler, M., 2009. Coupled cluster benchmarks of water monomers and dimers extracted from density-functional theory liquid water: The importance of monomer deformations. Journal of Chemical Physics 131. doi:10.1063/1.3236840.

Sanville, E., Kenny, S.D., Smith, R., Henkelman, G., 2007. Improved grid-based algorithm for bader charge allocation. Journal of computational chemistry 28, 899–908.

Satta, N., Criniti, G., Kurnosov, A., Boffa Ballaran, T., Ishii, T., Marquardt, H., 2021. High-Pressure Elasticity of $\delta$-(Al,Fe)OOH Single Crystals and Seismic Detectability of Hydrous MORB in the Shallow Lower Mantle. Geophysical Research Letters 48, 1–10. doi:10.1029/2021GL094185.

Sayvetz, A., 1939. The kinetic energy of polyatomic molecules. The Journal of chemical physics 7, 383–389.

Schrödinger, E., 1926. An undulatory theory of the mechanics of atoms and molecules. Physical review 28, 1049.

Schwerdtfeger, P., 2011. The pseudopotential approximation in electronic structure theory. ChemPhysChem 12, 3143–3155.

Shephard, G.E., Houser, C., Hernlund, J.W., Valencia-Cardona, J.J., Trønnes, R.G., Wentzcovitch, R.M., 2021. Seismological expression of the iron spin crossover in ferropericlase in the Earth's lower mantle. Nature Communications 12, 1–11. URL: http://dx.doi.org/10.1038/s41467-021-26115-z, doi:10.1038/s41467-021-26115-z.

Skelton, J.M., Burton, L.A., Jackson, A.J., Oba, F., Parker, S.C., Walsh, A., Jackson, A.J., Oba, F., 2017. Lattice dynamics of the tin sulphides SnS2, SnS and Sn2S3: Vibrational spectra and thermal transport. Physical Chemistry Chemical Physics 19, 12452–12465. doi:10.1039/c7cp01680h.

Slater, J.C., 1928. The self consistent field and the structure of atoms. Physical Review 32, 339.

Slater, J.C., 1930. Note on hartree's method. Physical Review 35, 210.

Solomatova, N.V., Caracas, R., Bindi, L., Asimow, P.D., 2022. Ab initio study of the structure and relative stability of MgSiO4H2polymorphs at high pressures and temperatures. American Mineralogist 107, 781–789. doi:10.2138/am-2021-7937.

Solomatova, N.V., Jackson, J.M., Sturhahn, W., Wicks, J.K., Zhao, J., Toellner, T.S., Kalkan, B., Steinhardt, W.M., 2016. Equation of state and spin crossover of (Mg,Fe)O at high pressure, with implications for explaining topographic relief at the core-mantle boundary. American Mineralogist 101, 1084–1093.

Solomon, S.C., 1979. Formation, history and energetics of cores in the terrestrial planets. Physics of the Earth and Planetary Interiors 19, 168–182.

Stacey, F.D., Loper, D.E., 1983. The thermal boundary-layer interpretation of d and its role as a plume source. Physics of the Earth and Planetary Interiors 33, 45–55.

Stephens, P.J., Devlin, F.J., Chabalowski, C.F., Frisch, M.J., 1994. Ab initio calculation of vibrational absorption and circular dichroism spectra using density functional force fields. The Journal of physical chemistry 98, 11623–11627.

Stevenson, D.J., 1981. Models of the Earth's Core. Science 214, 611–619.

Stixrude, L., 2014. Melting in super-earths. Philosophical Transactions of the Royal Society A: Mathematical, Physical and Engineering Sciences 372, 20130076.

Stixrude, L., Cohen, R., Singh, D., 1994. Iron at high pressure: Linearized-augmented-plane-wave computations in the generalized-gradient approximation. Physical Review B 50, 6442.

Stixrude, L., Karki, B., 2005. Structure and freezing of mgsio3 liquid in earth's lower mantle. Science 310, 297–299.

Stixrude, L., de Koker, N., Sun, N., Mookherjee, M., Karki, B.B., 2009. Thermodynamics of silicate liquids in the deep earth. Earth and Planetary Science Letters 278, 226–232.

Stixrude, L., Lithgow-Bertelloni, C., 2005. Mineralogy and elasticity of the oceanic upper mantle: Origin of the low-velocity zone. Journal of Geophysical Research: Solid Earth 110, 1–16. doi:10.1029/2004JB002965.

Stixrude, L., Scipioni, R., Desjarlais, M.P., 2020. A silicate dynamo in the early Earth. Nature Communications 11, 6–10. URL: http://dx.doi.org/10.1038/s41467-020-14773-4, doi:10.1038/s41467-020-14773-4.

Sun, J., Ruzsinszky, A., Perdew, J.P., 2015. Strongly constrained and appropriately normed semilocal density functional. Physical review letters 115, 036402.

Suzuki, A., 2010. High-pressure X-ray di V raction study of -FeOOH. Physics and Chemistry of Minerals 37, 153–157. doi:10.1007/s00269-009-0319-x.

Suzuki, A., 2016. Pressure–volume–temperature equation of state of $\epsilon$–FeOOH to 11 GPa and 700 K. Journal of Mineralogical and Petrological Sciences 111, 420–424. doi:10.2465/jmps.160719c.

Suzuki, A., 2017. Thermal equation of state of goethite ($\alpha$-FeOOH). High Pressure Research 37, 193–199. doi:10.1080/08957959.2017.1301938.

Takafuji, N., Hirose, K., Mitome, M., Bando, Y., 2005. Solubilities of O and Si in liquid iron in equilibrium with (Mg,Fe)SiO3 perovskite and the light elements in the core. Geophysical Research Letters 32, 1–4. doi:10.1029/2005GL022773.

Tang, W., Sanville, E., Henkelman, G., 2009. A grid-based bader analysis algorithm without lattice bias. Journal of Physics: Condensed Matter 21, 084204.

Tao, J., Perdew, J.P., Staroverov, V.N., Scuseria, G.E., 2003. Climbing the density functional ladder: Nonempirical meta–generalized gradient approximation designed for molecules and solids. Physical review letters 91, 146401.

Tarduno, J.A., Cottrell, R.D., Bono, R.K., Oda, H., Davis, W.J., Fayek, M., Erve, O.v., Nimmo, F., Huang, W., Thern, E.R., et al., 2020. Paleomagnetism indicates that primary magnetite in zircon records a strong hadean geodynamo. Proceedings of the National Academy of Sciences 117, 2309–2318.

Tarduno, J.A., Cottrell, R.D., Davis, W.J., Nimmo, F., Bono, R.K., 2015. A Hadean to Paleoarchean geodynamo recorded by single zircon crystals. Science 349, 521–524.

Tarduno, J.A., Cottrell, R.D., Watkeys, M.K., Hofmann, A., Doubrovine, P.V., Mamajek, E.E., Liu, D., Sibeck, D.G., Neukirch, L.P., Usui, Y., 2010. Geodynamo, solar wind,

and magnetopause 3.4 to 3.45 billion years ago. Science 327, 1238–1240. doi:10.1126/science.1183445.

Thomas, L.H., 1927. The calculation of atomic fields, in: Mathematical proceedings of the Cambridge philosophical society, Cambridge University Press. pp. 542–548.

Thompson, E.C., Campbell, A.J., Tsuchiya, J., 2017. Elasticity of $\epsilon$-FeOOH: Seismic implications for Earth's lower mantle. Journal of geophysical research 122, 1–10. doi:10.1002/2017JB014168.

Thompson, E.C., Campbell, A.J., Tsuchiya, J., 2021. Elastic properties of the pyrite-type feooh-alooh system from first-principles calculations. Geochemistry, Geophysics, Geosystems 22, e2021GC009703.

Thompson, E.C., Davis, A.H., Brauser, N.M., Liu, Z., Prakapenka, V.B., Campbell, A.J., 2020. Phase transitions in -FeOOH at high pressure and ambient temperature. American Mineralogist 105, 1769–1777. doi:10.2138/am-2020-7468.

Togo, A., 2023. First-principles phonon calculations with phonopy and phono3py. J. Phys. Soc. Jpn. 92, 012001. doi:10.7566/JPSJ.92.012001.

Togo, A., Chaput, L., Tadano, T., Tanaka, I., 2023. Implementation strategies in phonopy and phono3py. J. Phys. Condens. Matter 35, 353001. doi:10.1088/1361-648X/acd831.

Togo, A., Tanaka, I., 2015. First principles phonon calculations in materials science. Scripta Materialia 108, 1–5. URL: http://dx.doi.org/10.1016/j.scriptamat.2015.07.021, doi:10.1016/j.scriptamat.2015.07.021.

Touboul, M., Kleine, T., Bourdon, B., Palme, H., Wieler, R., 2007. Late formation and prolonged differentiation of the moon inferred from w isotopes in lunar metals. Nature 450, 1206–1209.

Trybel, F., Meier, T., Wang, B., Steinle-Neumann, G., 2021. Absence of proton tunneling during the hydrogen-bond symmetrization in $\delta$-AlOOH. Physical Review B 104, 1–6. doi:10.1103/PhysRevB.104.104311.

Tschauner, O., Huang, S., Greenberg, E., Prakapenka, V.B., Ma, C., Rossman, G.R., Shen, A.H., Zhang, D., Newville, M., Lanzirotti, A., Tait, K., 2018. Ice-VII inclusions in diamonds: Evidence for aqueous fluid in Earth's deep mantle. Science 359, 1136–1139. doi:10.1126/science.aao3030.

Tsuchiya, J., Mookherjee, M., 2015. Crystal structure, equation of state, and elasticity of phase H(MgSiO4H2) at Earth's lower mantle pressures. Scientific Reports 5, 1–8. doi:10.1038/srep15534.

Tsuchiya, J., Tsuchiya, T., 2009. Elastic properties of $\delta$-AlOOH under pressure: First principles investigation. Physics of the Earth and Planetary Interiors 174, 122–127. doi:10.1016/j.pepi.2009.01.008.

Tsuchiya, J., Tsuchiya, T., Sano, A., Ohtani, E., 2008a. First principles prediction of new high-pressure phase of inooh. Journal of Mineralogical and Petrological Sciences 103, 116–120.

Tsuchiya, J., Tsuchiya, T., Tsuneyuki, S., Tsune, 2005. First-principles study of hydrogen bond symmetrization of phase D under high pressure. American Mineralogist 90, 44–49. doi:10.2138/am.2005.1628.

Tsuchiya, J., Tsuchiya, T., Wentzcovitch, R.M., 2008b. Vibrational properties of $\delta$-alooh under pressure. American Mineralogist 93, 477–482.

Tsuchiya, T., Tsuchiya, J., Dekura, H., Ritterbex, S., 2020. Ab initio study on the lower mantle minerals. Annual Review of Earth and Planetary Sciences 48, 99–119.

Tsuchiya, T., Wentzcovitch, R.M., Da Silva, C.R., De Gironcoli, S., Silva, C.R.S., Gironcoli, S.D., 2006. Spin Transition in Magnesiowustite in Earth's Lower Mantle. Physical Review Letters 96, 1–4. doi:10.1103/PhysRevLett.96.198501.

Verhoogen, J., 1961. Heat balance of the earth's core. Geophysical Journal International 4, 276–281.

Verlet, L., 1967. Computer" experiments" on classical fluids. i. thermodynamical properties of lennard-jones molecules. Physical review 159, 98.

Wahl, S.M., Militzer, B., 2015. High-temperature miscibility of iron and rock during terrestrial planet formation. Earth and Planetary Science Letters 410, 25–33. URL: www.elsevier.com/locate/epsl, doi:10.1016/j.epsl.2014.11.014.

Walker, D., Norby, L., Jones, J., 1993. Superheating effects on metal-silicate partitioning of siderophile elements. Science 262, 1858–1861.

Walter, M.J., Thomson, A.R., Wang, W., Lord, O.T., Ross, J., McMahon, S.C., Baron, M.A., Melekhova, E., Kleppe, A.K., Kohn, S.C., 2015. The stability of hydrous silicates in Earth's lower mantle: Experimental constraints from the systems MgO-SiO2-H2O and MgO-Al2O3-SiO2-H2O. Chemical Geology 418, 16–29. URL: http://dx.doi.org/10.1016/j.chemgeo.2015.05.001, doi:10.1016/j.chemgeo.2015.05.001.

Wang, R., Yoshino, T., 2021. Electrical conductivity of diaspore, $\delta$-AlOOH and -FeOOH. American Mineralogist 106, 774–781. doi:10.2138/am-2021-7605.

Whaler, K., 1986. Geomagnetic evidence for fluid upwelling at the core-mantle boundary. Geophysical Journal International 86, 563–588.

Wicks, J., Jackson, J., Sturhahn, W., 2010. Very low sound velocities in iron-rich (mg, fe) o: Implications for the core-mantle boundary region. Geophysical Research Letters 37.

Widom, B., 1982. Potential-distribution theory and the statistical mechanics of fluids. The Journal of Physical Chemistry 86, 869–872.

Wigner, E., Huntington, H.á., 1935. On the possibility of a metallic modification of hydrogen. The Journal of Chemical Physics 3, 764–770.

Willard, A.P., Chandler, D., 2010. Instantaneous liquid interfaces. The Journal of Physical Chemistry B 114, 1954–1958.

Wilson, A., Stixrude, L., 2021. Entropy, dynamics, and freezing of casio3 liquid. Geochimica et Cosmochimica Acta 302, 1–17.

Wilson, A.J., Pozzo, M., Alfè, D., Walker, A.M., Greenwood, S., Pommier, A., Davies, C.J., 2022. Powering earth's ancient dynamo with silicon precipitation. Geophysical Research Letters 49, e2022GL100692.

Wilson, A.J., Walker, A.M., Alfè, D., Davies, C.J., 2021. Probing the nucleation of iron in Earth's core using molecular dynamics simulations of supercooled liquids. Physical Review B 103, 1–6. doi:10.1103/PhysRevB.103.214113.

Wilson, E.B., Decius, J.C., Cross, P.C., 1980. Molecular vibrations: the theory of infrared and Raman vibrational spectra. Courier Corporation.

Wood, B.J., 2008. Accretion and core formation: constraints from metal–silicate partitioning. Philosophical Transactions of the Royal Society A: Mathematical, Physical and Engineering Sciences 366, 4339–4355.

Wood, B.J., Wade, J., Kilburn, M.R., 2008. Core formation and the oxidation state of the earth: Additional constraints from nb, v and cr partitioning. Geochimica et Cosmochimica Acta 72, 1415–1426.

Xiao, B., Stixrude, L., 2018. Critical vaporization of mgsio3. Proceedings of the National Academy of Sciences 115, 5371–5376.

Xu, W., Greenberg, E., Rozenberg, G.K., Pasternak, M.P., Bykova, E., Boffa-Ballaran, T., Dubrovinsky, L., Prakapenka, V., Hanfland, M., Vekilova, O.Y., Simak, S.I., Abrikosov, I.A., 2013. Pressure-induced hydrogen bond symmetrization in iron oxyhydroxide. Physical Review Letters 111, 1–5. doi:10.1103/PhysRevLett.111.175501.

Yang, J., Tong, X., Lin, J.F., Okuchi, T., Tomioka, N., 2015. Elasticity of Ferropericlase across the Spin Crossover in the Earth's Lower Mantle. Scientific Reports 5, 1–9. doi:10.1038/srep17188.

Yin, Q., Jacobsen, S., Yamashita, K., Blichert-Toft, J., Télouk, P., Albarede, F., 2002. A short timescale for terrestrial planet formation from hf–w chronometry of meteorites. Nature 418, 949–952.

Young, C.J., Lay, T., 1987. The core-mantle boundary. Annual Review of Earth and Planetary Sciences 15, 25–46.

Young, E.D., Shahar, A., Schlichting, H.E., 2023. Earth shaped by primordial h2 atmospheres. Nature 616, 306–311.

Yu, M., Trinkle, D.R., 2011. Accurate and efficient algorithm for bader charge integration. The Journal of chemical physics 134.

Yuan, L., Ohtani, E., Ikuta, D., Kamada, S., Tsuchiya, J., Naohisa, H., Ohishi, Y., Suzuki, A., 2018. Chemical reactions between fe and h2o up to megabar pressures and implications for water storage in the earth's mantle and core. Geophysical Research Letters 45, 1330–1338.

Yuen, D., Peltier, W., 1980. Mantle plumes and the thermal stability of the d layer. Geophysical Research Letters 7, 625–628.

Zhang, Z., Stixrude, L., Brodholt, J., 2013. Elastic properties of mgsio3-perovskite under

lower mantle conditions and the composition of the deep earth. Earth and Planetary Science Letters 379, 1–12.

Zhao, Y., Truhlar, D.G., 2006. Density functional for spectroscopy: no long-range self-interaction error, good performance for rydberg and charge-transfer states, and better performance on average than b3lyp for ground states. The Journal of Physical Chemistry A 110, 13126–13130.

Zhuang, Y., Gan, B., Cui, Z., Tang, R., Tao, R., Hou, M., Jiang, G., Popescu, C., Garbarino, G., Zhang, Y., Hu, Q., 2022. Mid-mantle water transportation implied by the electrical and seismic properties of $\epsilon$-FeOOH. Science Bulletin 67, 748–754. URL: https://doi.org/10.1016/j.scib.2021.12.002, doi:10.1016/j.scib.2021.12.002.